

A203333
REPORT SD-TR-88-98

Adhesion in Chemically Hostile Environments: The Use of Filled Polymers as Diffusion Barriers

R. S. BRETZLAFF and R. Y. SUGIHARA
Materials Sciences Laboratory
Laboratory Operations
The Aerospace Corporation
El Segundo, CA 90245

1 November 1988

Prepared for
SPACE DIVISION
AIR FORCE SYSTEMS COMMAND
Los Angeles Air Force Base
P.O. Box 92960
Los Angeles, CA 90009-2960

DTIC
ELECTE
DEC 29 1988
S D

APPROVED FOR PUBLIC RELEASE;
DISTRIBUTION UNLIMITED

88 12 28 137

REPORT DOCUMENTATION PAGE

1a. REPORT SECURITY CLASSIFICATION Unclassified			1b. RESTRICTIVE MARKINGS		
2a. SECURITY CLASSIFICATION AUTHORITY			3. DISTRIBUTION/AVAILABILITY OF REPORT Approved for public release; distribution unlimited.		
2b. DECLASSIFICATION/DOWNGRADING SCHEDULE					
4. PERFORMING ORGANIZATION REPORT NUMBER(S) TR-0088(3935-03)-1			5. MONITORING ORGANIZATION REPORT NUMBER(S) SD-TR-88-98		
6a. NAME OF PERFORMING ORGANIZATION The Aerospace Corporation Laboratory Operations		6b. OFFICE SYMBOL (If applicable)	7a. NAME OF MONITORING ORGANIZATION Space Division		
6c. ADDRESS (City, State, and ZIP Code) El Segundo, CA 90245			7b. ADDRESS (City, State, and ZIP Code) Los Angeles Air Force Base Los Angeles, CA 90009-2960		
8a. NAME OF FUNDING/SPONSORING ORGANIZATION		8b. OFFICE SYMBOL (If applicable)	9. PROCUREMENT INSTRUMENT IDENTIFICATION NUMBER F04701-85-C-0086-P00019		
8c. ADDRESS (City, State, and ZIP Code)			10. SOURCE OF FUNDING NUMBERS		
			PROGRAM ELEMENT NO.	PROJECT NO.	TASK NO.
11. TITLE (Include Security Classification) Adhesion in Chemically Hostile Environments: The Use of Filled Polymers as Diffusion Barriers					
12. PERSONAL AUTHOR(S) Bretzlaff, Robert S., and Sugihara, Richard Y.					
13a. TYPE OF REPORT		13b. TIME COVERED FROM TO		14. DATE OF REPORT (Year, Month, Day) 1988 November 1	
15. PAGE COUNT 98					
16. SUPPLEMENTARY NOTATION					
17. COSATI CODES			18. SUBJECT TERMS (Continue on reverse if necessary and identify by block number)		
FIELD	GROUP	SUB-GROUP	Adhesion Diffusion Metal substrates		
			Barrier liners Fillers Polymers		
			Corrosion Hydrogen fluoride Reactive gases		
19. ABSTRACT (Continue on reverse if necessary and identify by block number)					
<p>Polymer/metal bonding is accomplished, in general, through a combination of chemical bonding and mechanical interlocking. In either case, the metal surface must remain uncorroded in order to preserve adhesion. If material layers that are close to the bonded interface evolve corrosive species, then the metal can be corroded and the adhesive strength reduced. One way to ameliorate this adhesive degradation is to coat the metal substrate with a barrier liner that is relatively impervious to the corrosive species. If subsequently bonded material layers evolve corrosive species, then relatively fewer of these molecules would be able to penetrate the barrier liner and corrode the substrate.</p> <p>The experiments reported here were performed on a polyurethane (Uralane 5753) with or without filler particles (alumina, strontium chromate, magnesium silicate, or carbon black) and subjected to gaseous hydrogen fluoride at ambient temperature. A method of analysis is developed that allows the calculation of two basic diffusion parameters (the diffusion</p>					
20. DISTRIBUTION/AVAILABILITY OF ABSTRACT <input type="checkbox"/> UNCLASSIFIED/UNLIMITED <input checked="" type="checkbox"/> SAME AS RPT. <input type="checkbox"/> DTIC USERS			21. ABSTRACT SECURITY CLASSIFICATION Unclassified		
22a. NAME OF RESPONSIBLE INDIVIDUAL			22b. TELEPHONE (Include Area Code)		22c. OFFICE SYMBOL

UNCLASSIFIED

SECURITY CLASSIFICATION OF THIS PAGE

19. ABSTRACT (Continued)

coefficient and the gas/polymer reactivity), as well as a quantitative measure of the barrier effectiveness for plane-slab geometries. For the slab thicknesses of interest, it was found that about 50% of the available corrosive molecules could be kept away from the metal substrate when the barrier liner diffusion coefficient is one-tenth of the diffusion coefficient in the adjacent matrix. About 90% of the corrosive molecules could be kept away when the corresponding ratio is one to one hundred. It was found that SrCrO_4 or carbon black can effect a tenfold or greater reduction of the Uralane diffusion coefficient. Thus, for the geometry studied, it seems possible with these filled polymer systems to prevent about 50% of the available corrosive species from impinging upon the metal substrate.

UNCLASSIFIED

SECURITY CLASSIFICATION OF THIS PAGE

PREFACE

The authors thank the following personnel of The Aerospace Corporation for their important contributions to this research: S. Schreiber for many helpful discussions on liner chemistry, R. Kobayashi for help in setting up the HF aging chamber, G. Cagle for preparing the initial Uralane samples, N. Marquez for ion mass microprobe analysis, J. Uht for work in scanning electron microscopy and particle-size analysis, and C. Su for polishing coupon sections. The availability of the Aerospace Space Sciences Laboratory's "DIRAC" VAX for the mathematical modeling is gratefully acknowledged. In addition, Dr. S. Hornung of American Hospital Supply is acknowledged for having provided expeditious scheduling of the X-ray photoelectron spectroscopy testing.

CONTENTS

PREFACE.....	1
I. INTRODUCTION.....	11
II. INITIAL RESULTS FOR GASEOUS HF DIFFUSION.....	17
A. Background.....	17
B. Initial Observations.....	18
C. Physical Model for Reactive Gas Diffusion in Filled Polymers.....	25
D. Computer Calculations and Their Physical Interpretation.....	30
E. Experimental Results.....	45
F. Summary.....	50
III. CALCULATION OF HF FLUX AT THE METAL SUBSTRATE.....	53
A. Background.....	53
B. Physical Model for the Diffusion of Reactive Gases out of a Matrix, Through a Liner, and onto a Metal Substrate.....	53
C. Computer Calculation for the Barrier Effectiveness, τ , of Filled Polymeric Liners.....	60
D. Computer Calculations of the Barrier Effectiveness, τ , for a Realistic Case of a Filled Polymer Containing Defects.....	74
E. Summary.....	80
IV. EFFECT OF FILLER TYPE ON HF DIFFUSION.....	85
A. Background.....	85
B. Diffusion-Front Trajectories.....	86
C. Experimental Method.....	91
D. Experimental Results.....	92
E. Summary.....	95

CONTENTS (Continued)

REFERENCES.....	99
APPENDIX A: RELATION OF COMPLEX ANALYSIS TO STURM- LIOUVILLE THEORY.....	101
APPENDIX B: USE OF COMPLEX ANALYSIS FOR CASE OF UNEQUAL D_1 AND D_2	103
APPENDIX C: PARTICLE-SIZE ANALYSIS.....	105

FIGURES

I-1.	SEM Micrographs of Ti-6Al-4V Coupon Treated with a Sodium Dichromate ($\text{Na}_2\text{Cr}_2\text{O}_7$)/Sulphuric Acid Etchant Before Rinsing and Vacuum Drying.....	12
I-2.	Severe Pock-Marking of Surface in SEM Micrographs After 1 Day's Exposure of an Uncoated Ti-6Al-4V Coupon to HF Vapor.....	13
I-3.	Definition of Geometry and Material Parameters.....	14
II-1.	Titanium-Alloy Coupon as Originally Spray Coated with PVB.....	19
II-2.	(Top) Enlarged View of One Corner of the Coated Coupon in Fig. II-1 after 1 Day of Exposure to "Pure" HF Vapor; (Bottom) Alumina-Filled and Unfilled Uralane 5753 Samples Cut from Larger Slabs of Material and Subjected to One-Dimensional Diffusion of HF Vapor.....	20-21
II-3.	Calculated Diffusion Profiles for $H = 0 \text{ Msec}^{-1}$	31
II-4.	Calculated Diffusion Profiles for $H = 1 \text{ Msec}^{-1}$	31
II-5.	Calculated Diffusion Profiles for $H = 10 \text{ Msec}^{-1}$	32
II-6.	Calculated Diffusion Profiles for $H = 100 \text{ Msec}^{-1}$	32
II-7.	Calculated Diffusion Profiles for $H = 1000 \text{ Msec}^{-1}$	33
II-8.	"Effective" Diffusion Front ($H = 0$) Advances According to $\langle x \rangle = 2\sqrt{Dt}$ into an Unbounded Medium (for $t < \tau$, i.e., when the back wall plays no role).....	37
II-9.	"Effective" Diffusion Front ($H = 10$) Advances According to $\langle x \rangle = 2\sqrt{Dt}$ Until Saturation (due to the nonzero H) Sets In.....	39
II-10.	"Effective" Diffusion Front of a Strongly Interacting System ($H = 1000$) Does Not Exhibit Classical $\langle x \rangle = 2\sqrt{Dt}$ Behavior in This Region.....	39
II-11.	"Effective" Diffusion Front ($H = 10$) Showing Longer-Time Behavior than Fig. II-9.....	43

FIGURES (Continued)

II-12.	(a) Experimental (ion microprobe) Diffusion Profile for Unfilled Uralane After 21 h of Exposure; (b) Experimental (ion microprobe) Diffusion Profile for Alumina-Filled Uralane After 21 h of Exposure.....	47
II-13.	(a) Experimental (XPS) Diffusion Profile for Unfilled Uralane After 12 Days of HF Exposure; (b) Experimental (XPS) Diffusion Profile for Alumina-Filled Uralane After 12 Days of HF Exposure.....	49
III-1.	Pole Structure of the Response Function $\bar{c}_i(s)$	58
III-2.	Roots of $C_d(s) = 0$ (excluding $s = 0$ and $s = -H$) Are Simple Poles of the Response Function $c_i(s)$	58
III-3.	HF Concentration vs Position at Several Times.....	63
III-4.	Time-Evolution of Total HF, HF at Sink, and HF at Metal, Corresponding to Fig. III-3.....	63
III-5.	HF Concentration vs Position at Several Times.....	64
III-6.	Time-Evolution of Total HF, HF at Sink, and HF at Metal, Corresponding to Fig. III-5.....	64
III-7.	HF Concentration vs Position at Several Times.....	65
III-8.	Time-Evolution of Total HF, HF to Sink, and HF to Metal, Corresponding to Fig. III-7.....	65
III-9.	HF Concentration vs Position at Several Times.....	66
III-10.	Time-Evolution of Total HF, HF at Sink, and HF at Metal, Corresponding to Fig. III-9.....	66
III-11.	HF Concentration vs Position at Several Times.....	67
III-12.	Time-Evolution of Total HF, HF to Sink, and HF to Metal, Corresponding to Fig. III-11.....	67
III-13.	HF Concentration vs Position at Several Times.....	68

FIGURES (Continued)

III-14.	Time-Evolution of Total HF, HF to Sink, and HF to Metal, Corresponding to Fig. III-13.....	68
III-15.	Barrier Effectiveness, τ , vs the Liner Diffusion Coefficient, D_2 , for Two Values of Liner Thickness.....	75
III-16.	Barrier Effectiveness, τ , vs the Liner Thickness, l_2 , for Two Values of the Liner Diffusion Coefficient, D_2	75
III-17.	HF Concentration vs Position at Several Times, Corresponding to an Unfilled Model-Polymer Liner as Measured in Section II.....	77
III-18.	Time-Evolution of Total HF, HF to Sink, and HF to Metal, Corresponding to Fig. III-17.....	77
III-19.	HF Concentration vs Position at Several Times, Corresponding to an Al_2O_3 -Filled Model-Polymer Liner as Measured in Section II.....	78
III-20.	Time-Evolution of Total HF, HF to Sink, and HF to Metal, Corresponding to Fig. III-19.....	78
III-21.	Single-Slab Profiles of HF Concentration Which Represent the Al_2O_3 -Filled Uralane Data in Fig. II-13b.....	79
III-22.	Single-Slab Results for the Parameters Given Above Figure.....	79
III-23.	Parallel-Pathways Model Result (single slab) for a Filled Polymer ($D = 0.1$, $H = 13$) with Defects ($D = 1$, $H = 0$).....	81
III-24.	Parallel-Pathways Result (double slab) for a Filled Polymer Liner ($D = 0.1$, $H = 13$) with Defects ($D = 1$, $H = 0$) in the Region $x > 0$	81
III-25.	Time-Evolution of Total HF, HF at Sink, and HF at Metal, Corresponding to Fig. III-24 (defective liner).....	82

FIGURES (Continued)

IV-1.	Calculated Concentration Profiles for the Diffusion of Gas into a Solid, Including the Reactivity Between the Gas and Solid.....	88
IV-2.	Same Concentration Profiles as in Fig. IV-1 Replotted on a Smaller Scale.....	88
IV-3.	Diffusion Trajectory, $\langle x \rangle$, Plotted vs Square Root of the Diffusion Time for Calculated Profiles in Fig. IV-2.....	90
IV-4.	Experimental Fluorine Concentration Profile for Unfilled Uralane After 9 Days of HF Exposure.....	93
IV-5.	Experimental Fluorine Concentration Profile for $\text{MgO} \cdot \text{SiO}_2$ -Filled Uralane After 9 Days of HF Exposure.....	94
IV-6.	Experimental Fluorine Concentration Profile for SrCrO_4 -Filled Uralane After 9 Days of HF Exposure.....	94
IV-7.	Experimental Fluorine Concentration Profile for Carbon-Black-Filled Uralane After 9 Days of HF Exposure.....	96

TABLES

II-1.	Diffusion Coefficients for Gas Molecules in Solid Polymers at 25°C.....	24
II-2.	Initial Slopes (σ_0) and Final Plateau Levels (P_0) for the Normalized Profiles for Several Values of the Interaction Parameter H.....	35
II-3.	Propagation into an Unbounded Medium.....	36
II-4.	Propagation into an Unbounded Medium.....	38
II-5.	Propagation into an Unbounded Medium.....	40
II-6.	Correlation of Profile Saturation with the Value of the Interaction Parameter, H.....	41
III-1.	Parameters Used in the Calculation of the Barrier Effectiveness, ζ , of Several One-Dimensional Matrix/Liner Systems.....	61-62
III-2.	Barrier Effectiveness, $\zeta(\%)$, for Matrix/Liner = 0.277/0.025 cm.....	69
III-3.	Barrier Effectiveness, $\zeta(\%)$, for Matrix/Liner = 0.277/0.005 cm.....	69
III-4.	Barrier Effectiveness, $\zeta(\%)$, for Matrix/Liner = 0.500/0.025 cm.....	70
III-5.	Barrier Effectiveness, $\zeta(\%)$, for Matrix/Liner = 0.500/0.005 cm.....	70
IV-1.	Effect of 9-Day Exposure on Freshly Cast Uralane 5753 with or Without Filler Particles.....	97

I. INTRODUCTION

The bonding of polymers to metals is accomplished through a combination of chemical bonding and physical interlocking of the polymer around surface asperities on the metal. Many detailed studies of this process have been conducted (see Refs. 1-3 and the citations therein). It is well known that the metal interface must remain in an uncorroded state in order to preserve adhesion during component aging. Much less is known about how to preserve that metal/polymer interface in the presence of neighboring material layers that evolve liquid or gaseous by-products during aging. Examples are (1) thermal insulators that must be held on spacecraft outer bond lines by siloxanes that evolve acetic acid during cure; (2) the various layers of coatings, liners, insulators, and propellants that must adhere to solid-rocket motor cases despite the high reactivity of some of the constituent materials; and (3) the adhesive "flypaper" used in some electronics packages in order to catch stray solder particles and hold them for long periods of time.

It is desired to investigate the effect of filled polymer liners in retarding diffusion of corrosive species to the metal/polymer interface. Consider the etched and bondable metal surface shown in Fig. I-1. After corrosive attack [this report concerns gaseous hydrogen fluoride (HF) as an example of a corrosive species], the same metal surface has the appearance shown in Fig. I-2. Clearly, a barrier liner on this metal that could prevent interaction with the HF would be desirable. The general situation considered in this report is shown in Fig. I-3.

The transport coefficients of proposed liner materials must be determined before calculations can reveal the extent to which the barrier reduces the flux (J_2 in Fig. I-3) of corrosive species (here, HF gas) at the metal substrate. Therefore, in Section II it will be shown how these transport coefficients are determined from one-dimensional diffusion experiments. Concentration profiles are measured in order to determine the basic diffusion coefficient, D_2 , and a second parameter, H , which specified the degree of reactivity between the gas and the liner material. In

Surface Preparation

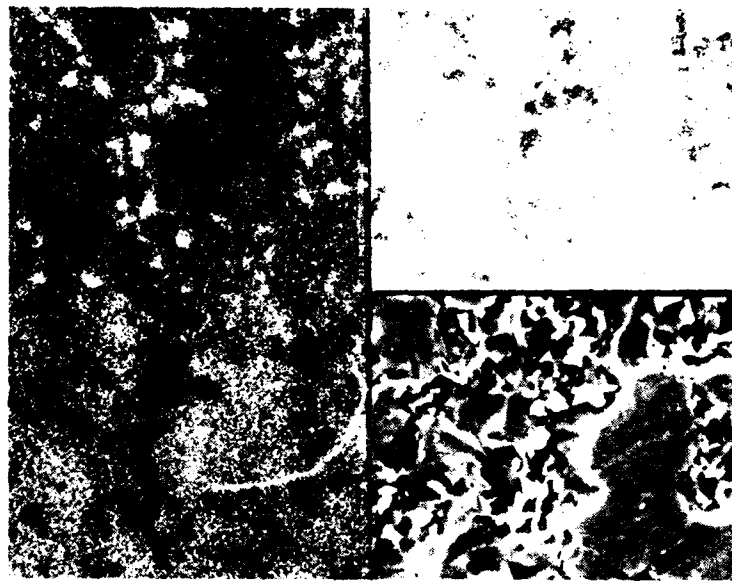
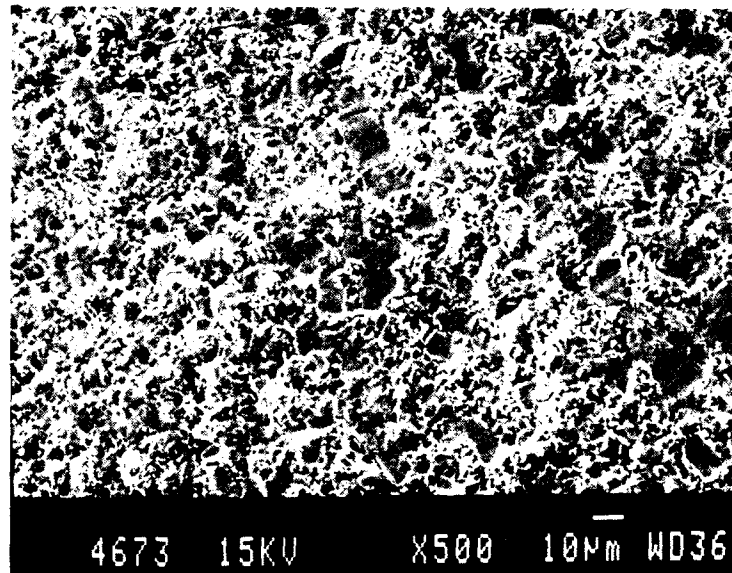


IMAGE	Al
Ti	V

Fig. I-1. SEM Micrographs of Ti-6Al-4V Coupon Treated with a Sodium Dichromate ($\text{Na}_2\text{Cr}_2\text{O}_7$)/Sulphuric Acid Etchant Before Rinsing and Vacuum Drying

Effect of HF on Titanium Alloy



← 5 mils →

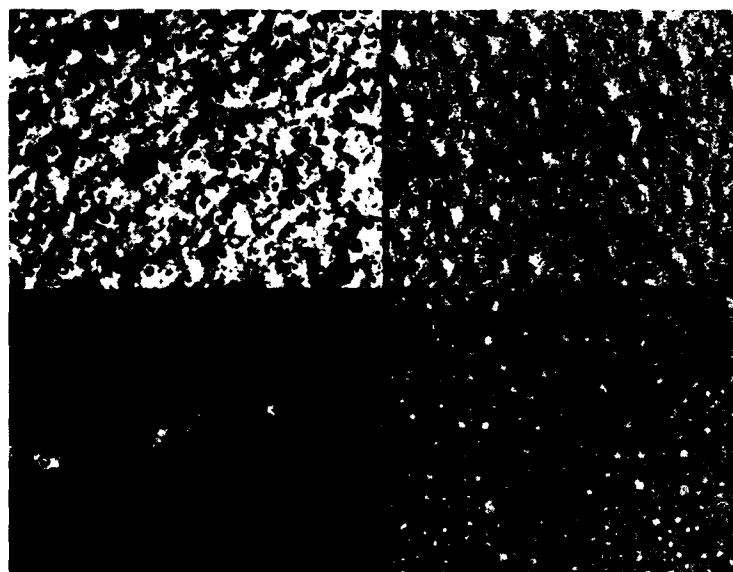


IMAGE	O
F	Ti

Fig. 1-2. Severe Pock-Marking of Surface in SEM Micrographs After 1 Day's Exposure of an Uncoated Ti-6Al-4V Coupon to HF Vapor

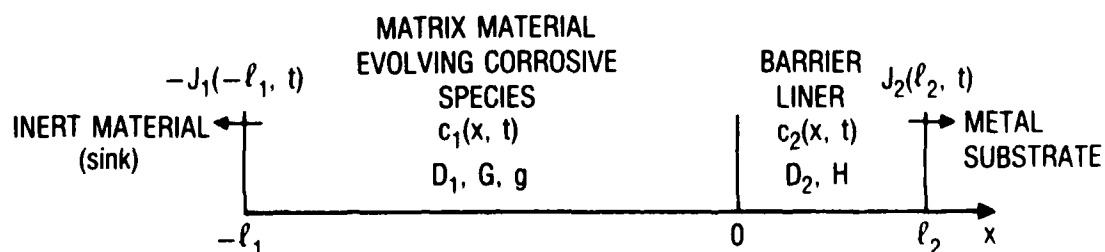


Fig. I-3. Definition of Geometry and Material Parameters. The concentrations, $c_1(x, t)$, of corrosive particles give rise to fluxes, J_1 , of corrosive particles impinging on the metal substrate and on the inert boundary material. The matrix material from $x = -l_1$ to $x = 0$ has a diffusion coefficient, D_1 , and evolves corrosive particles at a rate $r = Ge^{-gt}$. The barrier liner from $x = 0$ to $x = l_1$ has a diffusion coefficient, D_2 , and reacts with the corrosive species with a characteristic rate, H .

addition, the diffusion coefficient, D_1 , of the corrosive species in the original matrix must be known or determined, as well as the rate of corrosive-species evolution, r . We take $r = G \exp(-gt)$, where G and g are constants and t is time.

In Section III, several sets of diffusion coefficients and reactivities are assumed for the two-layer system shown in Fig. I-3. Time-dependent concentration profiles and cumulative fluxes are calculated. A barrier effectiveness is defined which is zero when half the number of evolved particles impinges on the metal substrate (the other half disappearing in the sink material on the side of the decomposing layer opposite to the metal substrate). The barrier effectiveness is 100% when none of the evolved particles impinges on the metal substrate. For the case of an 0.277-cm thick decomposing layer next to an 0.025-cm thick barrier liner, it is shown that about half of the potentially impinging corrosive species can be kept away from the metal substrate when the diffusion coefficient of the liner is one-tenth that of the decomposing matrix.

In Section IV, experimental results for the diffusion of gaseous HF in a filled or unfilled polyurethane liner are reported. It is shown that SrCrO_4 or carbon black can effect a tenfold or greater reduction in the polyurethane diffusion coefficient. Thus, it seems reasonable to expect filled polymeric liners to prevent about 50% of the potentially impinging, corrosive particles from reaching the metal substrate.

II. INITIAL RESULTS FOR GASEOUS HF DIFFUSION

A. BACKGROUND

This investigation considers the case in which adhesion must be maintained over an approximately 10-year lifetime, during which there is a slow evolution of corrosive HF gas⁴ from a material layer that has, on one side, a sensitive adhesive/metal interface and, on the other side, a layer of material (or a free surface) that is not sensitive. The polymer adhesive is chosen to be the polyurethane, Uralane 5753. It has been often informally proposed that filling the polymer with materials such as alumina, carbon, strontium chromate, magnesium silicate, zinc oxide, or titanium dioxide would create a barrier liner, which would reduce the amount of HF incident on the wall. It is not clear a priori if this effect should arise from chemically binding the HF within the liner or from kinetically favoring diffusion to the material layer (or free surface) that is not sensitive.

The Aerospace Materials Sciences Laboratory (MSL) has developed a method for quantifying the resistance of filled polymers to gaseous HF diffusion. The method provides quantitative transport coefficients for filled polymers on the basis of (1) concentration profile measurements from one-dimensional diffusion experiments and (2) the assumption of a particular phenomenological diffusion model. The determination of these transport coefficients is the subject of this report. The subsequent calculation of the HF flux incident on the metal surface will be discussed in the next section.

The effectiveness of filler particles needs to be quantified for the following reason. The matrix polymer must be selected for its intrinsic bondability to titanium alloy and its intrinsic resistance to HF diffusion. However, if filler particle effectiveness is well characterized, then the matrix polymer can be selected with an increased emphasis on intrinsic bondability and with the expectation that the filler will adequately impede HF diffusion. Of course this approach must be used

cautiously, because it is highly unlikely that the properties of highly filled systems will be simple averages of the intrinsic properties of the filler and of the matrix.

B. INITIAL OBSERVATIONS

The search for a suitable barrier liner begins with the selection of an appropriate matrix polymer. We initially experimented with polyvinyl butyral (PVB), which is a well-known, chemically resistant resin manufactured by Monsanto under the name of Butvar. By varying the polymerization conditions, Monsanto produces different kinds of Butvar with differing percentages of acetal, alcohol, and acetate side groups. We experimented with the Monsanto Metal Coating 2009, containing 5.1 wt% phenolic, 13 wt% epoxy, 2 wt% Butvar B-90, and 79.9% of various solvents.

In order to judge the HF resistance of the unfilled Coating 2009, we first prepared the surfaces of Ti-6Al-4V coupons with sodium dichromate ($\text{Na}_2\text{Cr}_2\text{O}_7$) and sulphuric acid etching, followed by rinsing and vacuum drying (see Fig. I-1). Metal Coating 2009 was then sprayed on these coupons to a thickness of 5 ± 2 mils (see Fig. II-1). The original intent was to use the metal surface beneath the coating as a "detector" of the time-dependent corrosion caused by HF penetration. This experiment was actually performed by holding a coated coupon for 1 day in a Teflon accelerated-aging chamber of "pure" HF vapor. (Some ambient atmosphere was present before the chamber was purged with HF.) In Fig. II-2a, it is seen, first, that debonding occurred. Therefore, the duration of the originally intended experiment could be no more than a few hours. Second, a nonuniform buildup of corrosion products is seen in Fig. II-2a. Even if the film had adhered to the coupons for a few hours, several cross sections of one coupon specimen at one aging time could give widely varying results for the corrosion buildup. These variations could be caused by thickness variations of the sprayed films.

EFFECT OF HF EXPOSURE

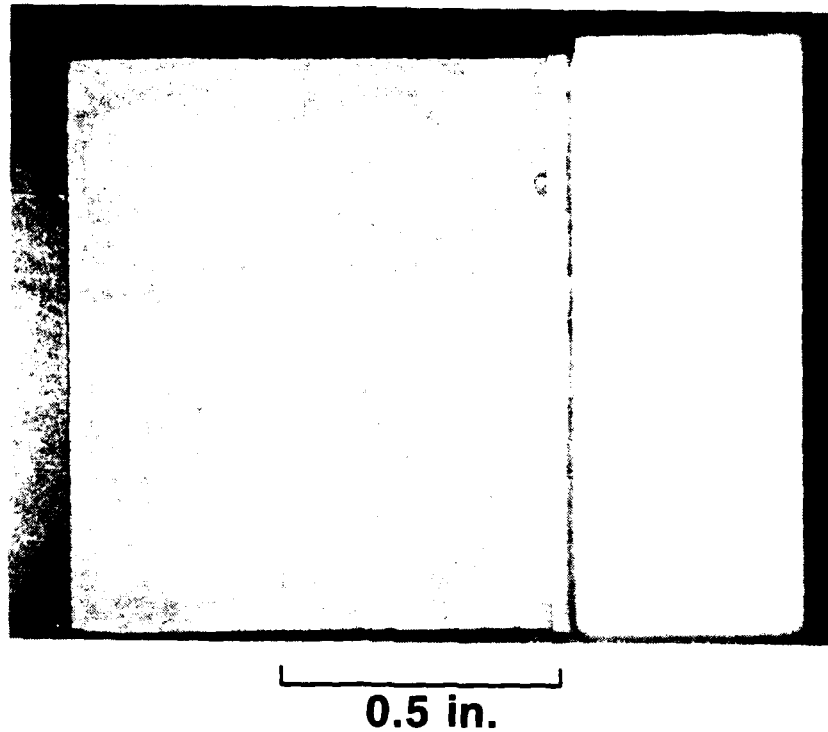
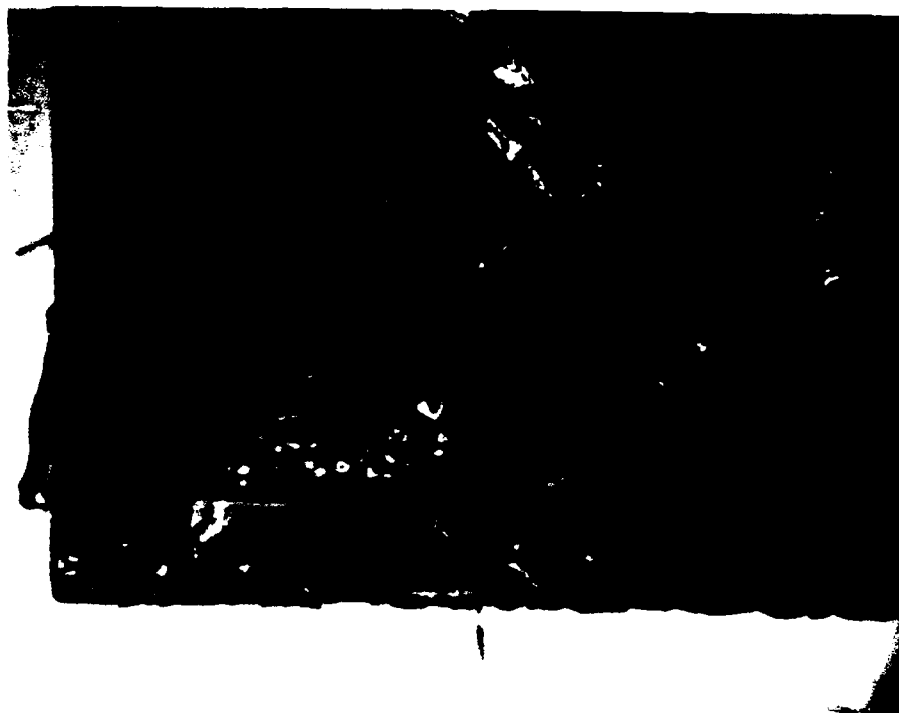


Fig. II-1. Titanium-Alloy Coupon as Originally Spray Coated with PVB. Teflon block on the right is a sample holder.

Fig. II-2. (Top photo, next page) Enlarged View of One Corner of the Coated Coupon in Fig. II-1 after 1 Day of Exposure to "Pure" (see text) HF Vapor.

(Bottom photo, next page) Alumina-Filled (top) and Unfilled (bottom) Uralane 5753 Samples Cut from Larger Slabs of Material and Subjected to One-Dimensional Diffusion of HF Vapor (from the left). The top sample is approximately 1/8 in. thick.



Third, and most important, was that as corrosion products accumulate at the metal interface within a coated coupon, the boundary conditions for diffusion change. Diffusion is governed by a partial differential equation whose solutions are codetermined by the boundary conditions at the metal interface. In this initial experimental arrangement, the initial boundary condition at the wall caused every impinging HF particle to interact with the metal and thus disappear from the diffusion process. After a sufficient buildup of corrosion products, as shown in Fig. I-2, the boundary condition resulted in no impinging HF reaction. In the initial experiment, it would have been difficult to separate this effect from the intrinsic property of a barrier liner material to impede diffusion.

Because of these problems, we improved the experimental arrangement. Our goal was to age the coupons in pure HF to accelerate diffusion and to obtain experimentally manageable measurement times. To realize this goal, we had to find a measurement configuration without time-dependent boundary conditions, so that the transport properties of the liner material could be clearly seen.

The improved arrangement selected for these diffusion experiments included a large slug of filled or unfilled material cured in a polyethylene cup of about 1 in. diam and 1 in. depth. The polyethylene, being relatively impervious (because of its crystalline content) and unreactive to HF, limited HF diffusion to one circular face of the sample when the cup was placed in a Teflon jar containing HF. After the slug was exposed to HF, it was sectioned so that ion mass microprobe analysis (IMMA) or X-ray photoelectron spectroscopy (XPS) could be used to determine fluorine content (normalized by carbon content) vs position. This experimental arrangement was preferable because in any of our possible experimental times, diffusion of HF to the back wall of the sample container was impossible. Thus, the assumed boundary condition at the back wall was much less important when evaluating the concentration profile.

It would have been advantageous to test filler/resin composites where the resin is the liner material. However, this is not possible, because the sprayable liner material contains a high percentage (80% in the case of Monsanto 2009) of solvent. Attempts to cure such material in bulk always yield large air bubbles. Attempts to cure such material layer by layer are time consuming and result in stratified samples with unknown interfacial resistance to diffusion between strata. Therefore, a model polymer was used as the matrix, with and without several filler types. The purpose of the experiment is to discover (1) how the matrix-polymer diffusion coefficient is affected (compared to the unfilled matrix) by the presence of the filler particles and (2) to what extent the filler particles additionally contribute to the composite's diffusion coefficient (e.g., by surface reactions on the filler particles that chemically trap some of the fluorine). When this knowledge is subsequently applied to real liner systems, the range⁵ of values for the unfilled matrix polymer can be assumed to be 10^{-6} to 10^{-8} cm²/sec, according to recorded experience (see Table II-1) with small gas molecules in polymer matrices. Using this range and experimental information, we can calculate the HF flux on the metal substrate and thereby estimate the potential for corrosion.

Figure II-2b exhibits specimens prepared from alumina-filled and unfilled slugs of Uralane 5753 (polyurethane) and exposed to HF vapor for 12 days. These specimens were made several years previously by MSL in conformance with a specification requiring a 10 ± 2 μ m particle size (50 μ m maximum). The alumina was fired at 700°C for 10 min and stored, covered, at 100-130°C for 24 h before use. Figure II-2b indicates that the filled system does retard HF diffusion (shown by the darkest area of HF reaction). An experimental technique was used to quantify the different HF concentration profiles in the two samples shown in Fig. II-2b. However, before describing this technique, we will construct a physical model for guidance in the experimental design and in the interpretation of the resulting profiles.

Table II-1. Diffusion Coefficients^a for Gas Molecules in Solid Polymers at 25°C^b

Polymer	Gas			
	H ₂ (MW=2) ^c	He (MW=4) ^c	H ₂ O (MW=18) ^c	CO ₂ (MW=44) ^c
poly(1,3-butadiene)	9.6	--	--	1.05
poly(butadiene-co-acrylonitrile)	6.43	15.5	--	0.425
poly(isoprene)	--	21.6	--	1.25
poly(ethylene) ρ=0.914	--	6.8	--	0.37
poly(ethylene) ρ=0.964	--	3.07	--	0.124
poly(ethyl methacrylate)	--	42.3	0.0989	0.033
poly(styrene)	--	10.4	0.14	0.058
poly(tetrafluoroethylene)	--	--	--	0.095
Teflon FEP	--	--	--	0.105
poly(vinyl chloride)		2.8	0.0238	0.0025

^aUnits are 10⁻⁶ cm²/sec.

^bSee Ref. 5 (p. III-232).

^cMolecular weight in grams per mole.

C. PHYSICAL MODEL FOR REACTIVE GAS DIFFUSION IN FILLED POLYMERS

Consider a one-dimensional slab of material between positions $x = 0$ and $x = l$. The slab initially contains zero HF. The concentration of HF (number of HF particles per length of material) within the slab is denoted by $c(x,t)$, where t is time. In this continuum model, any filler particles (micron sized) are considered to be much smaller than the slab thickness, l . (The slab thickness is mil sized, i.e., about 25 times larger than the particle size). A constant concentration, c_0 , of gas is present at the slab surface, $x = 0$, and no gas transport is assumed to occur at $x = l$. However, as shown in the preceding section, this second boundary condition is not critical for short experiment times. It is required to determine $c(x,t)$ in order to calculate the number of HF particles that impinge on the back wall of the sample.

The analysis of unreactive gas diffusion proceeds in terms of a diffusion coefficient, D , for the system. The analysis must be refined for the present case of reactive gas. We hypothesize that the following boundary-value equations are applicable to this problem, where H is the reactivity of the gas with the system and $-Hc$ is the rate of HF particle reduction resulting from this reaction:

$$D \frac{\partial^2 c}{\partial x^2} - Hc = \frac{\partial c}{\partial t} \quad (1)$$

for $0 \leq x \leq l$, $t \geq 0$ and D and H constant

Initial condition:

$$c(x,0) = 0 \quad (2)$$

Boundary conditions:

$$c(0,t) = c_0 \quad (3)$$

$$\frac{\partial c}{\partial x}(l,t) = 0 \quad (4)$$

In this boundary value problem, the units of D are evidently area per time, and the units of H are inverse time. The feature that allows for the reactive nature of the gas is the term $-Hc$.

There are at least three possible physical interpretations for the term $-Hc$. [Of course, the phenomenological suitability of the model can only be established by matching calculated and measured profiles. Acceptance or rejection of the microscopic mechanisms(s) underlying this problem must be determined by other methods.] First, $-Hc$ could be a sink term for the annihilation of diffusing molecules at a rate proportional to the concentration of HF. A sink term is common in heat conduction problems but would conflict with our ideas about the conservation of matter. Second, the $-Hc$ term could refer to a rate of trapping (chemically immobilizing) the diffusing particles by reactive sites in the system. This idea seems attractive but does not allow for the saturation of available trap sites at very long times. Third, the $-Hc$ term could refer to the rate of diffusion-channel clogging by the ongoing process of chemical reaction and physical adsorption of the diffusing particles. This interpretation can be considered mathematically to be caused by a reverse current of rejected particles. This current reduces the net flux of particles into regions of lower concentration. Alternately, and most generally, this third case can be interpreted as due to a time-dependent diffusion coefficient resulting from all physical and chemical processes of diffusant immobilization. Consider the case of no reaction:

$$-\nabla \cdot J = \partial_t c \quad (5a)$$

$$c(x,t) = - \int_0^t dt' \nabla \cdot J(x,t') \quad (5b)$$

where J is the particle flux. When reaction occurs

$$-\nabla \cdot J_{\text{eff}} = -\nabla \cdot J - Hc = \partial_t c \quad (6a)$$

$$c(x,t) = - \int_0^t dt' \nabla \cdot J_{\text{eff}} \quad (6b)$$

where J_{eff} is the net flux into regions of lower concentration. Formally combining Eqs. (6a) and (6b), we obtain

$$-\nabla \cdot J + H \int_0^t dt' \nabla \cdot J_{eff} = \partial_t c \quad (7a)$$

Assuming interchangeability of integration and differentiation for non-pathological functions

$$-\nabla \cdot (J - H \int_0^t dt' J_{eff}) = \partial_t c \quad (7b)$$

Comparing Eqs. (6a) and (7b)

$$J_{eff}(x,t) = J(x,t) - H \int_0^t dt' J_{eff}(x,t') \quad (7c)$$

We define an effective diffusion coefficient, $D_{eff}(x,t)$, by

$$J_{eff}(x,t) = -D_{eff}(x,t) \nabla c(x,t) \quad (8a)$$

Therefore, whenever ∇c is nonzero, Eqs. (7c) and (8a) yield

$$D_{eff}(x,t) = D - H \int_0^t dt' D_{eff}(x,t') \frac{\nabla c(x,t')}{\nabla c(x,t)} \quad (8b)$$

This equation is of the form

$$D_{\text{eff}}(t) = D - H \int_0^t dt' D_{\text{eff}}(t') K(t', t) \quad (8c)$$

which is a Volterra integral equation with the kernel $K(t', t)$.⁶ $D_{\text{eff}}(t)$ is a function whose value clearly decreases monotonically from the value D at $t = 0$. Before Eq. (8c) can be solved, $c(x, t)$ must be found.

The solution $c(x, t)$ to the single slab problem specified by Eqs. (1)-(4) could be obtained from a Sturm-Liouville eigenvalue approach. However, the calculation of HF flux at the metal substrate (to be presented in Section III) clearly must allow for two adjacent layers (matrix and liner). Churchill⁷ has shown that the solution to such a problem, in which there is more than one layer, cannot be constructed with the Sturm-Liouville approach. Therefore, the alternate method of Ref. 8 is used here as a deliberate choice and in subsequent multislabs calculations as a necessity.

Laplace-transforming⁹ Eqs. (1) and (2), we obtain

$$\partial_x^2 \bar{c} - \omega^2 \bar{c} = 0 \quad (9a)$$

$$\omega^2 = \frac{H + s}{D} \quad (9b)$$

where $\bar{c}(s)$ is the Laplace transform of $c(t)$, suppressing the x -variable notation. Consequently

$$\bar{c} = A \cosh \omega x + B \sinh \omega x \quad (9c)$$

where A and B are constants. Applying Eqs. (3) and (4), we obtain

$$\bar{c}(s) = \frac{c_0}{s} \left\{ \frac{\cosh[\omega l(1 - x/l)]}{\cosh \omega l} \right\} \quad (9d)$$

Letting the denominator of $\bar{c}(s)$ be denoted by $f(s)$, we obtain

$$f(s) = s \cosh\left(\sqrt{\frac{H+s}{D}} l\right) \quad (10a)$$

Note that $f(s) > 0$ for all $s > 0$. For $s = 0$, $f(s) = 0$. For $s < 0$ and $|s| \leq H$, $f(s) < 0$. For $s < 0$ and $|s| > H$, $f(s) = 0$ whenever

$$0 = s_n \cosh\left[i \sqrt{\frac{-(H+s_n)}{D}} l\right] \quad (10b)$$

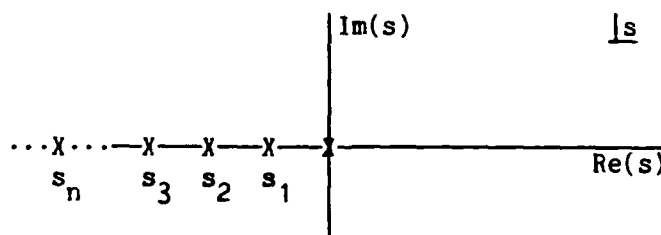
or

$$s_n = -H - \frac{(2n-1)^2}{\tau} \quad (10c)$$

$$n = 1, 2, 3, \dots$$

$$\tau = \frac{4l^2}{D\pi^2}$$

Therefore, the pole structure (which is all first order) of $\bar{c}(s)$ is



Expanding $\bar{c}(s)$ according to the Mittag-Leffler theorem,¹⁰ we have

$$\bar{c}(s) = \frac{\text{Res}[\bar{c}(s), 0]}{s} + \sum_{n=1}^{\infty} \frac{\text{Res}[\bar{c}(s), s_n]}{s - s_n} \quad (11a)$$

where $\text{Res}[\bar{c}(s), s']$ denotes the residue of $\bar{c}(s)$ at $s = s'$. Evaluating the residues, we have

$$\text{Res}[\bar{c}(s), 0] = \frac{c_0 \cosh[\omega_0 l(1 - x/l)]}{\cosh \omega_0 l} \quad (11b)$$

$$\omega_0 = \sqrt{H/D} \quad (11c)$$

$$\text{Res}[\bar{c}(s), s_n] = 2c_0 \frac{\sqrt{D}}{l} \cdot \frac{\sqrt{-(s_n + H)}}{s_n} \sin\left[\sqrt{\frac{-(s_n + H)}{D}} x\right] \quad (11d)$$

Laplace-inverting Eq. (11a), we obtain

$$\frac{c(x,t)}{c_0} = \frac{\cosh[\omega_0 l(1 - x/l)]}{\cosh \omega_0 l} + \frac{2\sqrt{D}}{l} \sum_{n=1}^{\infty} \frac{\sqrt{-(s_n + H)}}{s_n} \sin\left[\sqrt{\frac{-(s_n + H)}{D}} x\right] \exp(s_n t)$$

$$\omega_0 = \sqrt{H/D}$$

$$s_n = -H - \frac{(2n-1)^2}{\tau} \quad n = 1, 2, 3, \dots \quad (12)$$

$$\tau = \frac{4l^2}{D\pi^2}$$

D. COMPUTER CALCULATIONS AND THEIR PHYSICAL INTERPRETATION

The results shown in Eq. (12) have been programmed on the Aerospace Space Science Laboratory's (SSL's) "DIRAC" VAX. The normalized profiles, $[c(x,t)/c_0]$, are given in Figs. II-3 through II-7. Figure II-3 represents the case $H = 0$, which is diffusion without chemical reaction, diffusion-channel clogging, and so on. In this report, we use megaseconds as the

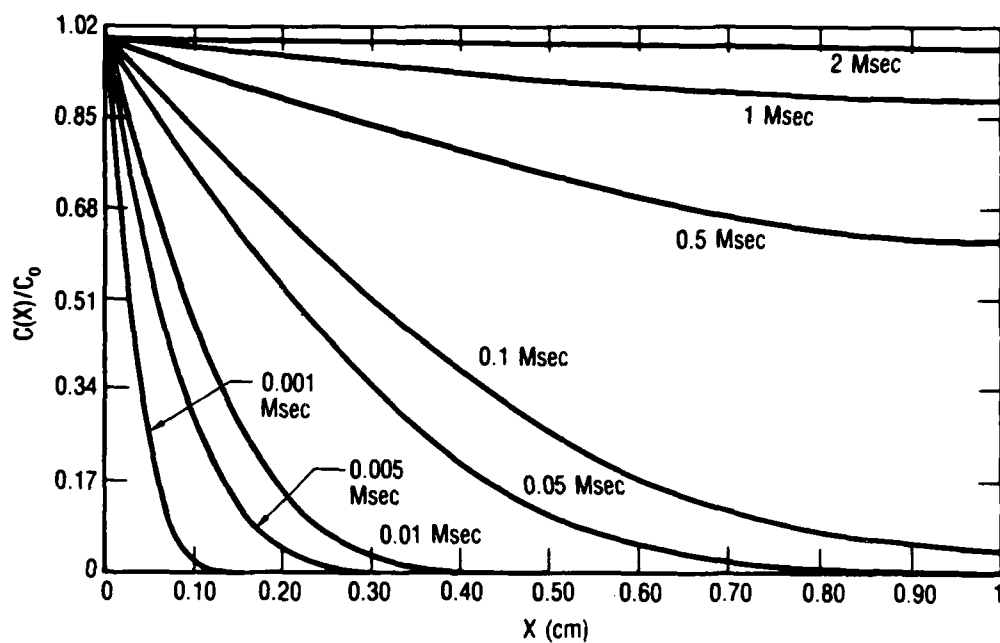


Fig. II-3. Calculated Diffusion Profiles for $H = 0 \text{ Msec}^{-1}$

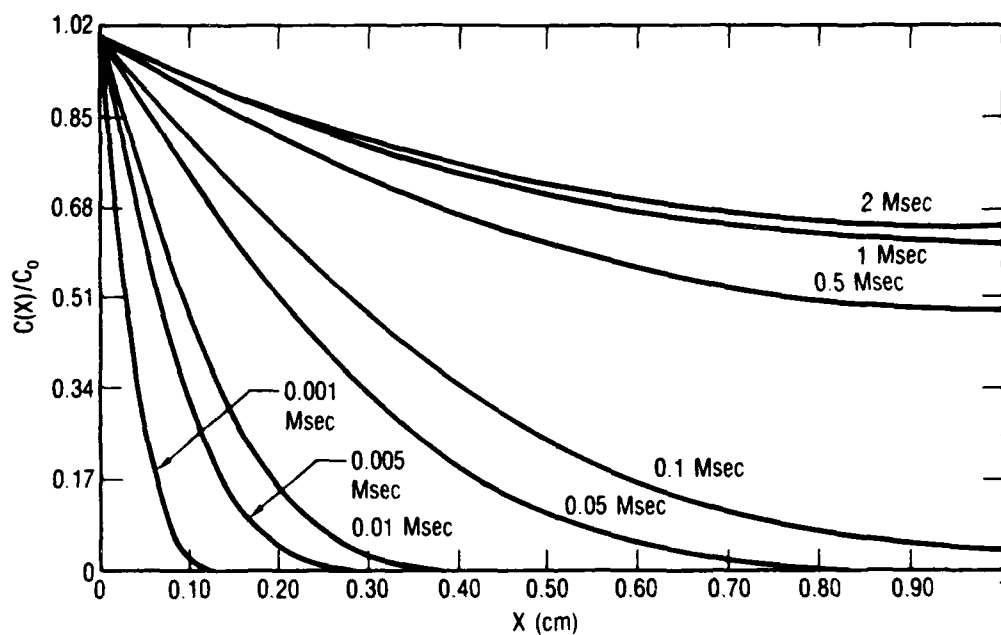


Fig. II-4. Calculated Diffusion Profiles for $H = 1 \text{ Msec}^{-1}$

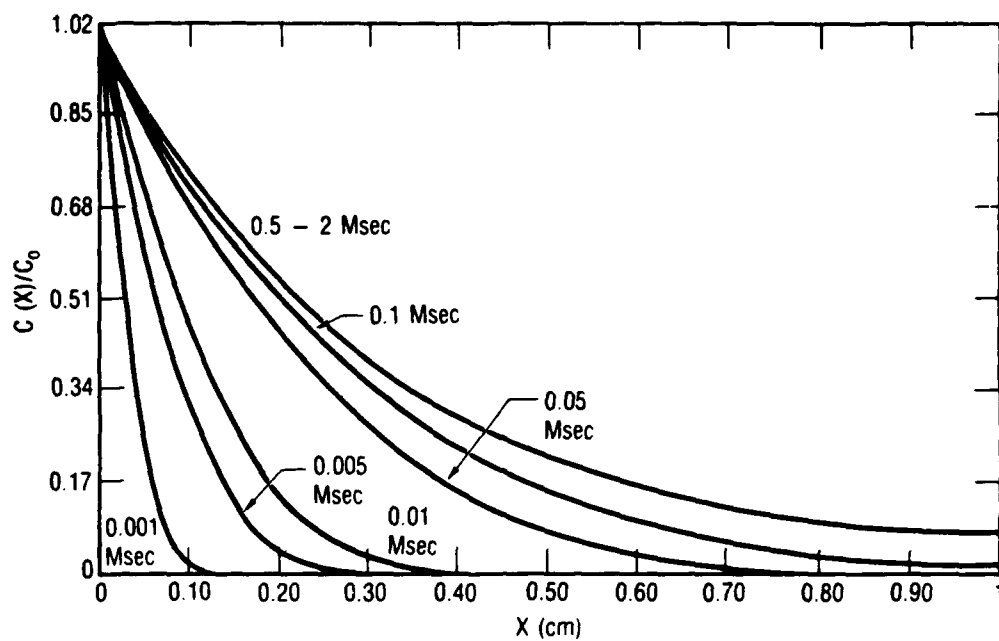


Fig. II-5. Calculated Diffusion Profiles for $H = 10 \text{ Msec}^{-1}$

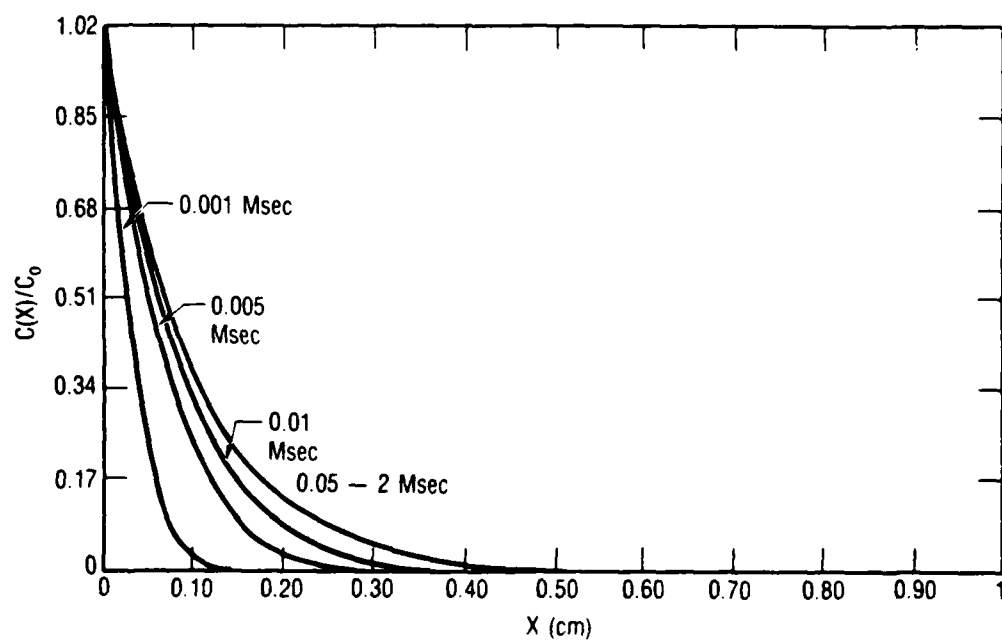


Fig. II-6. Calculated Diffusion Profiles for $H = 100 \text{ Msec}^{-1}$

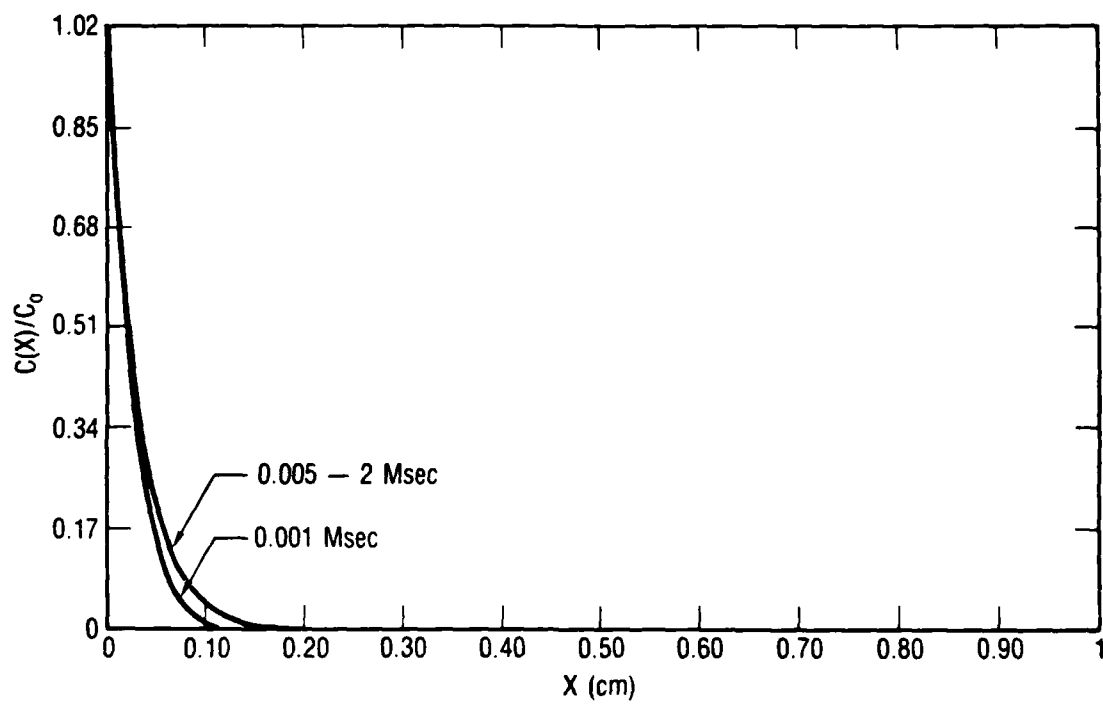


Fig. 11-7. Calculated Diffusion Profiles for $H = 1000 \text{ Msec}^{-1}$

unit of time for the calculations. One megasecond is 278 h. At long times, $t \geq 2 \text{ Msec} > \tau = 0.406 \text{ Msec}$, the profile is flat, and diffusion is complete.

Numerical values of the parameters used in the calculation of the normalized profiles are as follows:

$$D = 1 \text{ cm}^2/\text{Msec}$$

$$l = 1 \text{ cm}$$

$$\tau = 4l^2/D\pi^2 \doteq 0.406 \text{ Msec}$$

$$t \text{ in Msec (1 Msec = 278 h)}$$

$$x \text{ in cm}$$

Profiles were calculated at the following times: 10^{-3} , 5×10^{-3} , 10^{-2} , 5×10^{-2} , 10^{-1} , 0.5, 1, and 2 Msec.

Figure II-3 shows calculated profiles for $H = 0 \text{ Msec}^{-1}$; Fig. II-4, for $H = 1 \text{ Msec}^{-1}$; Fig. II-5, for $H = 10 \text{ Msec}^{-1}$; Fig. II-6, for $H = 100 \text{ Msec}^{-1}$, and Fig. II-7 for $H = 1000 \text{ Msec}^{-1}$. In Fig. II-4 (where $H = 1$), we see that the 0.5, 1, and 2 Msec results are significantly shifted. In fact, even as $t \rightarrow \infty$, the flat profile is not attained. This is shown by taking the derivative, σ_0 , of Eq. (12) at $x = 0$ and letting t tend to infinity:

$$\sigma_0 \equiv \lim_{t \rightarrow \infty} \frac{1}{c_0} \left. \frac{\partial c}{\partial x} \right|_{x=0} = -\sqrt{\frac{H}{D}} \tanh \left(\sqrt{\frac{H}{D}} l \right) \quad (13a)$$

Because $\sigma_0 < 0$ for $H > 0$, the flat profile is never attained. The final value, P_0 , for the plateau level is

$$P_0 \equiv \lim_{t \rightarrow \infty} \frac{1}{c_0} c(l, t) = \text{sech} \left(\sqrt{\frac{H}{D}} l \right) \quad (13b)$$

Some numerical results for σ_0 and P_0 are given in Table II-2.

Table II-2. Initial Slopes (σ_o) and Final Plateau Levels (P_o) for the Normalized Profiles for Several Values of the Interaction Parameter H

H (Msec ⁻¹)	σ_o (cm ⁻¹)	P_o (dimensionless)
0	0	1
1	-0.762	0.65
10	-3.15	0.085
100	-10.0	10 ⁻⁴
1000	-31.6	10 ⁻¹⁴

This suppression of the infinite-time plateau, shown in Figs. II-4 through II-7, is consistent with a "rejection current" resulting from annihilation, trapping, clogging, and so on:

$$L = - \int_0^L dx H c(x,t) \quad (14a)$$

$$G = J(o,t) = - D \nabla c(x,t) \Big|_{x=0} \quad (14b)$$

where L is the rate of reduction of mobile HF particles throughout the slab and G is the rate of increase of HF particles caused by diffusion from the environment into the slab at position $x = o$. As the time tends to infinity, the integral and the derivative of the infinite series terms [compare Eqs. (12), (14a), and (14b)] are zero, so that $L = - \sqrt{HD} c_o$ and $G = \sqrt{HD} c_o$ (particles/Msec).

In Fig. II-5 ($H = 10$), we see that the results for $t = 0.5, 1$, and 2 Msec actually superimpose. In Fig. II-6 ($H = 100$), the last five times have coincident profiles. In Fig. II-7 ($H = 1000$), this saturation is reached at $t = 5 \times 10^{-3}$ Msec, which is only about 1.4 h. Clearly, HF diffusion can be significantly restricted for a sufficiently large interaction parameter, H . If measurements are made at a time close to the system relaxation time, τ , and if a result is obtained like that for $t = 0.5$ Msec (1.25τ) in Fig. II-3, then H is undoubtedly very small. If the results are like those from $t = 0.005$ to 2 Msec in Fig. II-7, then H is very large. We need a method for extracting D and H from measured profiles.

We know⁶ that one-dimensional diffusion into an unbounded medium is governed by $\langle x \rangle = 2 \sqrt{Dt}$, where $\langle x \rangle$ is an "effective" penetration depth. In Fig. II-3, let $\langle x \rangle$ be the position at which $c(x,t)/c_0$ assumes the value 0.17. The values in Fig. II-3 of $\langle x \rangle$ for $t = 10^{-3}$ to 10^{-1} Msec are unaffected by the presence of the back wall of the sample container. These values are listed in Table II-3 and Fig. II-8. On the other hand, the role

Table II-3. Propagation Into an Unbounded Medium^a

$\langle x \rangle$ (cm)	t (Msec)	\sqrt{t} (Msec ^{1/2})	$\langle x \rangle / (2\sqrt{t})$ (cm/Msec ^{1/2})	\bar{D} (cm ² /Msec)
0.062	0.001	0.0316	0.98	0.96
0.14	0.005	0.0705	0.99	0.98
0.20	0.010	0.1000	1	1
0.44	0.050	0.2236	0.98	0.96
0.61	0.100	0.3162	0.96	0.92

^aData from Fig. II-3 ($H = 0$) for $t \leq 0.1$ Msec:

$\langle x \rangle$ defined at $c(x,t)/c_0 = 0.17$

$D = 1 \text{ cm}^2/\text{Msec}$

\bar{D} = apparent (secant) value of D (see Fig. II-8)

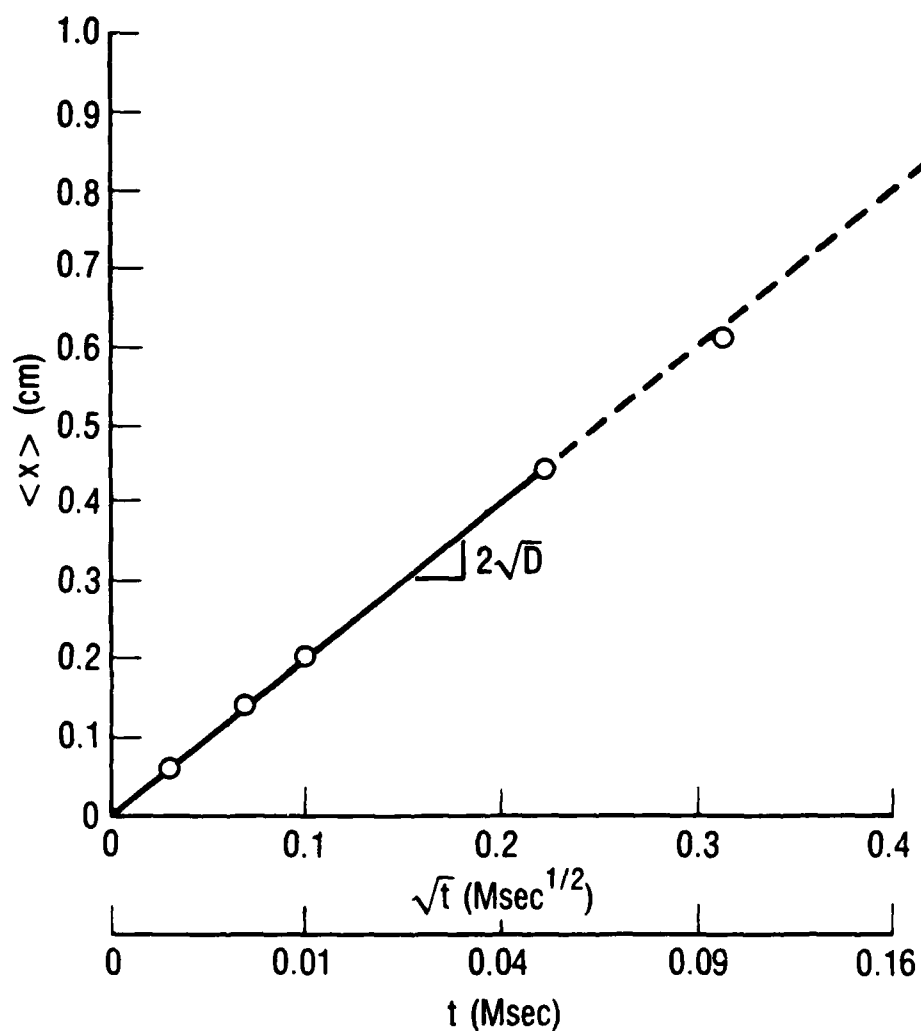


Fig. II-8. "Effective" Diffusion Front ($H = 0$) Advances According to $\langle x \rangle = 2\sqrt{Dt}$ into an Unbounded Medium (for $t < \tau$, i.e., when the back wall plays no role). The plotted points are obtained from Fig. II-3 (see text).

of $H = 10$ in Fig. II-5 is seen in Table II-4 and Fig. II-9 as a deviation from the "classical" $\langle x \rangle = 2 \sqrt{Dt}$ trajectory. The deviation of $\langle x \rangle$ from $2 \sqrt{Dt}$ is most pronounced in the case of $H = 1000 \text{ Msec}^{-1}$ (see Table II-5 and Fig. II-10).

Table II-4. Propagation into an Unbounded Medium^a

$\langle x \rangle$ (cm)	t (Msec)	\sqrt{t} (Msec ^{1/2})	$\langle x \rangle / (2\sqrt{t})$ (cm/Msec ^{1/2})	\tilde{D} (cm ² /Msec)
0.062	0.001	0.0316	0.98	0.96
0.14	0.005	0.0705	0.99	0.98
0.19	0.010	0.1000	0.95	0.90
0.39	0.050	0.2236	0.87	0.76
0.49	0.100	0.3162	0.77	0.59
0.585	0.5	0.705	0.41	0.17

^aData from Fig. II-5 ($H = 0$) for $t \leq 0.5 \text{ Msec}$:

$\langle x \rangle$ defined at $c(x,t)/c_0 = 0.17$

$D = 1.0 \text{ cm}^2/\text{Msec}$

\tilde{D} = apparent (secant) value of D (see Fig. II-9)

Compare Figs. II-8, II-9, and II-10, where $\langle x \rangle$ is plotted vs \sqrt{t} . In Fig. II-8, when several measurements lie on a straight line through the origin, we may identify the slope with $2 \sqrt{D}$. From Fig. II-8, by itself, we can only conclude that the measurement times are too short for any H value to be determined (although we know that $H = 0$ in this particular case). Figure II-10 is at the other extreme, where there are not at least two nonzero $\langle x \rangle$ measurements on a straight line through the origin. We can only conclude that the measurement times were too long to determine D . Figure II-9 is the intermediate case, where D can be determined from the slope of the line that passes through the first two nonzero $\langle x \rangle$ points as well as the origin. The value of H in Fig. II-9 can be determined as follows.

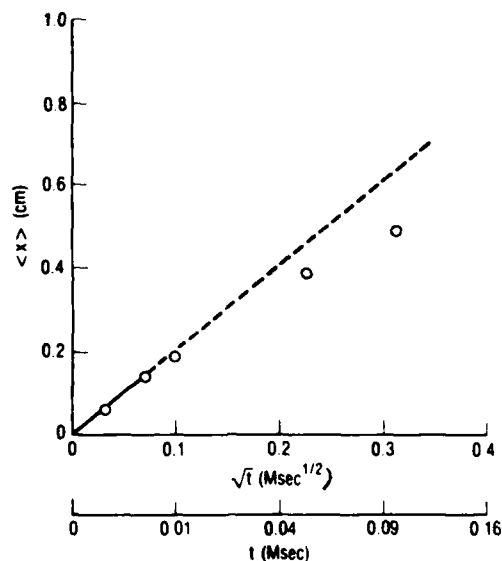


Fig. II-9. "Effective" Diffusion Front ($H = 10$) Advances According to $\langle x \rangle = 2\sqrt{Dt}$ Until Saturation (due to the nonzero H) Sets In. Here, deviation starts at $\sqrt{t} = 0.223 \text{ Msec}^{1/2}$. The plotted points are obtained from Fig. II-5 (see text).

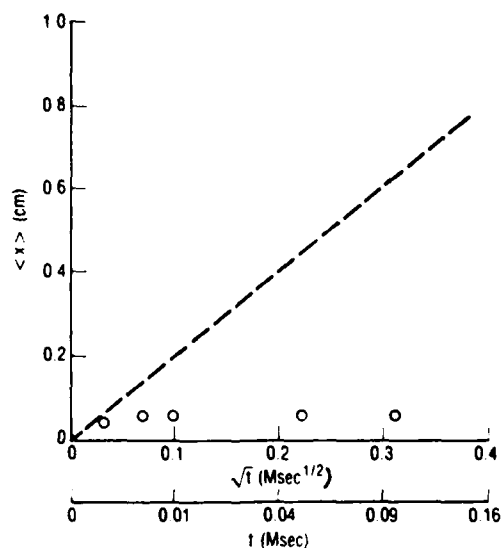


Fig. II-10. "Effective" Diffusion Front of a Strongly Interacting System ($H = 1000$) Does Not Exhibit Classical $\langle x \rangle = 2\sqrt{Dt}$ Behavior in This Region. For times sufficiently smaller than 10^{-3} Msec, classical behavior should be regained. The plotted points are obtained from Fig. II-7 (see text).

Table II-5. Propagation Into an Unbounded Medium^a

$\langle x \rangle$ (cm)	t (Msec)	\sqrt{t} (Msec ^{1/2})	$\langle x \rangle / (2\sqrt{t})$ (cm/Msec ^{1/2})	\bar{D} (cm ² /Msec)
0.047	0.001	0.0316	0.74	0.41
0.057	0.005	0.0705	0.40	0.16
0.057	0.010	0.1000	0.28	0.078
0.057	0.050	0.2230	0.13	0.017
0.057	0.100	0.3162	0.09	0.008

^aData from Fig. II-7 ($H = 0$) for $t \leq 0.1$ Msec:

$\langle x \rangle$ defined at $c(x,t)/c_0 = 0.17$

$D = 1.0$ cm²/Msec

\bar{D} = apparent (secant) value of D (see Fig. II-10)

Ordinary ($H = 0$) diffusion into a slab may be considered as a relaxation of concentration with a time constant $\tau = 4l^2/D\pi^2$. This relaxation is typical of a process occurring at a rate v , where

$$v = \frac{\sqrt{\bar{D}}}{\sqrt{t}} \quad (15a)$$

$$\langle x \rangle = \int_0^t v(t') dt' = 2 \sqrt{\bar{D}t} \quad (15b)$$

On the other hand, consider the data from Figs. II-3 through II-7, listed in Table II-6. Apparently, a second relaxation is occurring with a time constant H^{-1} . We hypothesize, therefore, that

$$v = \frac{\sqrt{\bar{D}}}{\sqrt{t}} \exp(-Ht) \quad (16a)$$

$$\langle x \rangle = \int_0^t v(t') dt' = \sqrt{\frac{D\pi}{H}} \operatorname{erf}(\sqrt{Ht}) \quad (16b)$$

Using the expansion¹¹ of the error function as well as its asymptotic value, we find

$$\langle x \rangle = 2 \sqrt{Dt} \left[1 - \frac{Ht}{3} + \frac{(Ht)^2}{10} - \dots \right] \quad (16c)$$

$$\langle x \rangle = 2 \sqrt{Dt} \quad Ht \ll 1 \quad (16d)$$

$$\langle x \rangle = \sqrt{\frac{D\pi}{H}} \quad t \rightarrow \infty \quad (16e)$$

Letting $f = \langle x \rangle / (2 \sqrt{Dt})$ and using Eq. (16c) (up to the quadratic term), we obtain the value of H from the short-time deviation of $\langle x \rangle$ from $2 \sqrt{Dt}$ as follows:

$$H = \frac{1}{t} \left[\frac{\frac{1}{3} - \frac{1}{9} - 0.4(1-f)}{0.2} \right] \quad (17)$$

Table II-6. Correlation of Profile Saturation with the Value of the Interaction Parameter, H^a

H (Msec ⁻¹)	Approximate saturation time (Msec)	$1/H$ (Msec)
0	∞	∞
1	2	1
10	0.5	0.1
100	0.05	0.01
1000	0.005	0.001

^aData from Figs. II-3 through II-7.

Applying Eqs. (16)-(17) in Fig. II-9, we find that classical $\langle x \rangle = 2\sqrt{Dt}$ diffusion occurs for $t \ll H^{-1} = 0.1$ Msec. We also find that $\sqrt{D\pi}/H = 0.56$ cm is a reasonable extrapolation for long-time behavior. To find H , we interpolate a synthetic data point between $t = 0.01$ and 0.05 , balancing the requirements of $t \ll 0.1$ Msec and of $\langle x \rangle$ being measurably different from $2\sqrt{Dt}$. We use $t = 0.0256$ Msec and $\langle x \rangle = 0.29$ cm. Applying Eq. (17) with $f = 0.29/0.32 = 0.906$, we find $H = 12 \text{ Msec}^{-1}$, which deviates significantly from the true value, $H = 10 \text{ Msec}^{-1}$. We conclude that the small deviations from the classical behavior will not accurately determine H . This is a strong conclusion, because it implies that diffusion-profile measurements must be made at times close to the system relaxation time ($\tau = 4l^2/D\pi^2$) in order to determine H . These times should be as follows: for $l = 2.54$ cm and $D = 1.0 \text{ cm}^2/\text{Msec}$, $\tau = 2.6 \text{ Msec} = 727 \text{ h} = 30.3 \text{ days}$; for $l = 2.54$ cm and $D = 0.01 \text{ cm}^2/\text{Msec}$, $\tau = 3030 \text{ days} = 8.3 \text{ years}$. However, such measurement times are impracticable. Therefore, H values, such as those in Fig. II-9, are best estimated only by order of magnitude.

To accurately determine H , we must have plateau values of $\langle x \rangle$ vs \sqrt{t} . For example, Fig. II-11 shows one more data point (at 0.5 Msec, taken from Fig. II-4) than Fig. II-9. The plateau value is 0.585 cm. Using Eq. (16e), $H = 9.2 \text{ Msec}^{-1}$. This determination of H is not in agreement with the true value of 10 ; however, it is at least an improvement over the estimate from short-time behavior. The presence of the back wall of the sample may be affecting this result. The agreement could possibly be improved if a refinement of the simple postulate, Eq. (16a), could be obtained. Considering Table II-5 and Fig. II-10, we note that the saturation $\langle x \rangle = 0.057$ cm is consistent with $H = D\pi/\langle x \rangle^2 = 967 \text{ Msec}^{-1}$, which is close to the true value, $H = 1000 \text{ Msec}^{-1}$. For such a strong interaction parameter, the measurements may be done in a time much less than τ . The problem, as noted in the discussion of Fig. II-10, is that D cannot be determined from this data. Shorter measurement times would have to be used to obtain the slope of $\langle x \rangle$ vs \sqrt{t} in the classical regime.

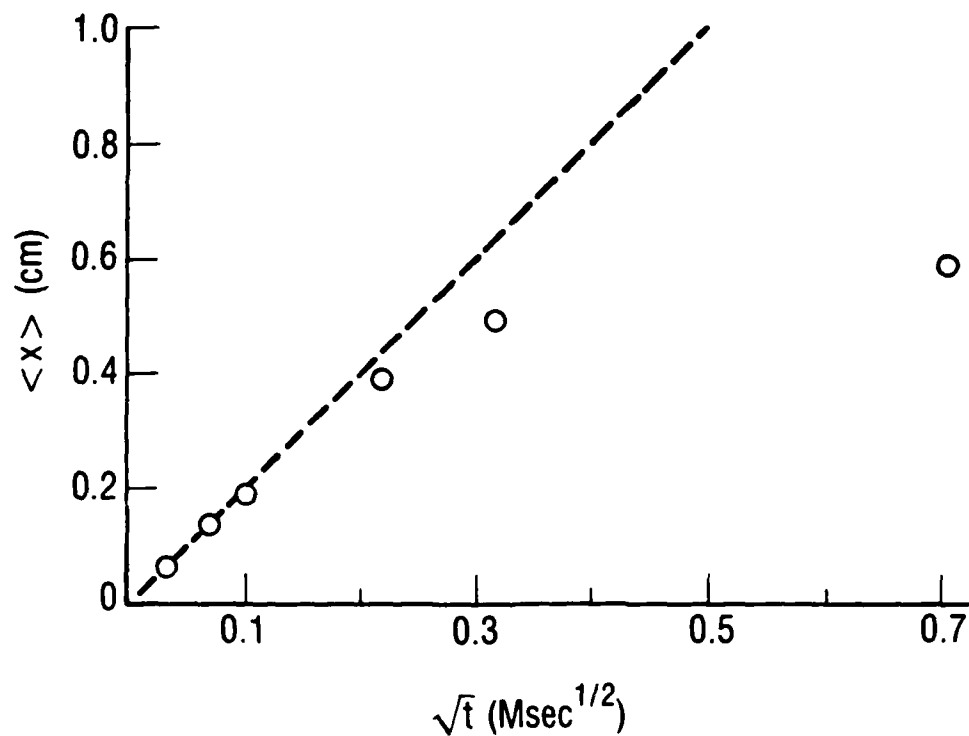


Fig. II-11. "Effective" Diffusion Front ($H = 10$) Showing Longer-Time Behavior than Fig. II-9. It is concluded (see text) that adequate data for the determination of D and H must be of this form.

In summary, to determine the D and H values for a system, data must be obtained in the form shown in Fig. II-11. In this figure, the initial slope provides D, and the final plateau provides $\sqrt{D\tau}/H$. If we cannot obtain long enough measurement times to reach the plateau, we must either assume $H = 0$ or at best estimate the order of magnitude of H. Of course, if the results remain on the $\langle x \rangle = 2 \sqrt{Dt}$ trajectory (until coupling to the back wall of the sample invalidates the unbounded-medium condition), then $H = 0$, or at least $H \ll \tau^{-1}$.

D and H must be determined for each polymer/gas system. H specifies the essential trapping/reactive nature of the filler particles (in conjunction with the matrix). If the H parameter is unmeasurably small, then there is no evidence to support the surface reactivity interpretation of the filler particle effect. But considering the visual impression of Fig. II-2b, it is anticipated that filler particles make a real difference. Even if there were no "H effect," there are important effects of the filler upon D. These effects have been documented in the diffusion of inert gases, as discussed in the next two paragraphs.

In the most widely accepted model for gas transport through polymers¹²⁻¹⁶ at temperatures below the glass transition temperature, T_g , each gas molecule must jump between fixed free-volume sites. Above T_g , the polymer segments are more mobile and the available, mobile free-volume vacancies for gas-molecule hopping allow propagation (diffusion) to occur at a faster rate. The rate of increase of the diffusion coefficient with temperature is relatively low for $T < T_g$, because the polymer lattice expands relatively little and because no additional free volume can enter the polymer system. The rate of increase of the diffusion coefficient with temperature is relatively high when $T > T_g$, because there is progressively more free volume in the system¹⁷ as the temperature rises.

The presence of filler reduces the mobility of the adsorbed (or chemically bonded) polymer segments. In effect, the glass transition temperature is higher in a thin layer of polymer adjacent to each filler particle, i.e., the polymer in this layer is below its T_g and allows less

gas-molecule diffusion. This layer of restricted mobility¹² can be as thick as 5000 to 8000 Å. Because the interparticle spacing¹² of a TiO₂-filled (19.25 wt%) polymer has been reported to be 1250 Å, the filler can place the entire matrix in a glassy state, which could not be achieved in an unfilled system at the same temperature. For example, the T_g of poly(vinyl acetate - vinyl chloride) can be raised from 30 to 51°C by appropriate loading.¹² The diffusion coefficient of such a glassy system will be correspondingly lower. Thus the filler could have a significant effect on the overall diffusion even if the filler particle surfaces were inert to the gas. We suggest that this effect also explains the restricted HF penetration into our filled polymers. Further testing is in progress to determine the T_g of filled and unfilled Uralane.

It is important to experimentally check the present mathematical model in order to ascertain whether factors in addition to concentration gradients are driving diffusion. It is known, in general, that chemical potential gradients drive diffusion and that concentration gradients are a special case of this effect. For example, low levels of some fillers were seen to increase the permeability of some liners to liquid migrants.¹⁸ It was postulated that this increase resulted from the chemical reactivity of the migrant with the filler.

E. EXPERIMENTAL RESULTS

One-dimensional diffusion experiments were conducted on alumina-filled (40 wt%) and on unfilled samples of the polyurethane Uralane 5753. Because the Uralane was cured in HF-impervious polyethylene cups, the HF could enter the Uralane only from its one exposed face. The cup was placed in an HF aging chamber, which was a larger Teflon jar that had a threaded lid sealed with an O-ring. Inlet and outlet bulkhead connectors made from Teflon were tightly installed in the jar wall. Teflon tubes connected the inlet to an HF lecture bottle and the outlet to a water bath that trapped excess HF. Teflon valves in the inlet and outlet lines maintained a tight seal after HF was introduced into the aging chamber. An ambient laboratory atmosphere (including humidity) was present in the aging chamber before the

chamber was purged for 5 min with HF to establish an HF atmosphere at room temperature. The HF atmosphere was "recharged" once per day during the aging period. The differences between HF diffusion in filled and unfilled samples are valid because each sample was in the identical environment.

One cup of unfilled Uralane and one cup of alumina-filled Uralane were simultaneously exposed in the same Teflon jar for 21 h. Slices were subsequently cut from the inside of the exposed samples, with the cuts perpendicular to the direction of diffusion. These samples were subjected to IMMA and were normalized by carbon concentration. The experimental diffusion profiles (Figs. II-12a and II-12b) deviated considerably from the calculated diffusion profiles (Figs. II-3 to II-7). This deviation was attributed to the surface roughness of the samples, which could not be polished because of the "smearability" of the profiles. However, the experimental results for the unfilled sample were consistent with a calculated profile of $\langle x \rangle = 2$ mm (a position where there is about 17% of the estimated 1.5 initial concentration in Fig. II-12a).

The IMMA results (Fig. II-12b) for the filled sample were consistent with the superposition of two effects. First, there was a sharper decrease in HF, of the type seen in Figs. II-3 to II-7, with $\langle x \rangle = 1$ mm. Second, there was an additional constant plateau level of about 20% of the initial ($= 1.5$) HF concentration, which extends relatively far into the sample. This is clearly an independent process that has been completed (level profile) but that is not present uniformly throughout the sample (only 20% of the surface concentration was obtained). One plausible explanation for such a process is the HF-induced debonding of polymer from filler particles. The resulting crevices could rapidly fill with HF gas but are limited in their volume fraction. This effect could be modeled by parallel diffusion pathways, where one diffusion coefficient is at least one order of magnitude faster than that of the gas molecule in the polymer matrix. Measurements at extremely short times would have to be conducted to ascertain exactly how many orders of magnitude are involved. This effect (of unestablished origin) is clearly harmful for a film proposed as a

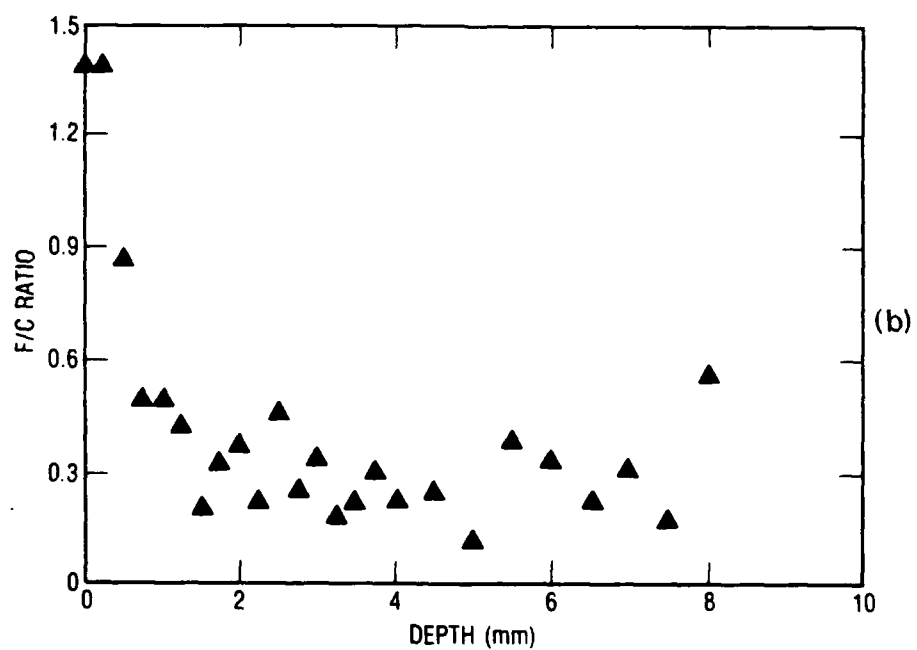
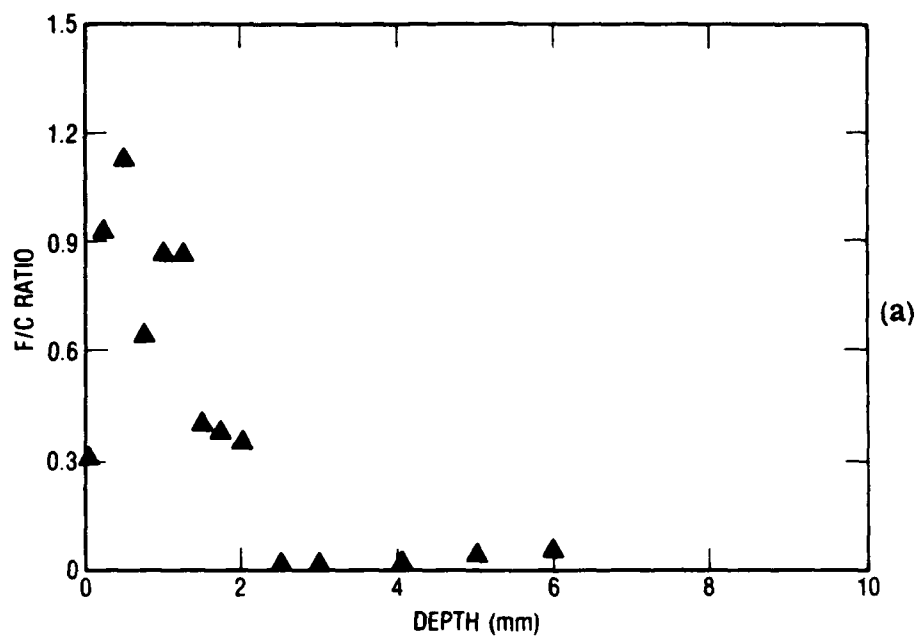


Fig. 11-12. (a) Experimental (ion microprobe) Diffusion Profile for Unfilled Uralane After 21 h of Exposure. (b) Experimental (ion microprobe) Diffusion Profile for Alumina-Filled Uralane After 21 h of Exposure.

propellant/motor case barrier. Further analysis is given in the next section in order to determine exactly how harmful this effect is.

Because of the surface roughness problem observed in the IMMA data, it was decided to obtain XPS data on two similar samples. After 12 days of aging, the slugs from the similar samples were withdrawn from the aging chamber and sectioned for XPS analysis. Initially, the oxygen 1s signal was analyzed, because the HF degradation reaction was responsible for smearing this peak (intensity vs binding energy), consistent with the formation of reaction by-products with varied oxygen bonding states. When no systematic variation could be found, carbon-normalized fluorine concentration vs position was analyzed. The XPS results for unfilled and filled Uralane are shown in Figs. II-13a and II-13b. The unfilled specimen has the calculated curve shape seen in Figs. II-3 to II-7, indicating that the surface roughness problem is not critical in XPS. The filled specimen (Fig. II-13b) shows the same superposition of two effects seen in the IMMA results (Fig. II-12b) but with less experimental scatter. Similarly, as before, the estimated HF penetration depths are 2 mm (unfilled) and 1 mm (filled). The penetration is (experimentally) the same even when sample exposure increases from 21 to 288 h. For unhindered diffusion, the diffusion front should have advanced by a factor of 3.7 between 21 and 288 h.

In this discussion, we assume that the profiles in Figs. II-12a and II-12b are the same as those in Figs. II-13a and II-13b, respectively. (Of course, the results shown in Fig. II-12 should be repeated using XPS.) If this assumption is true, then we have obtained the case shown in Fig. II-10 (as opposed to Figs. II-8 and II-9) for both the filled and unfilled samples. It follows that $t = 21 \text{ h} \geq H^{-1}$, or $H \geq 13 \text{ Msec}^{-1}$, in either filled or unfilled samples. It does not follow that H is the same for both filled and unfilled samples, only that the values of H for both samples are consistent with $H \geq 13 \text{ Msec}^{-1}$. Furthermore, $|\sigma_0| = \sqrt{H/D} = 4 \text{ cm}^{-1}$ (unfilled) and 11 cm^{-1} (filled) [see Eq. (13a) and Figs. II-13a and II-13b]. The corresponding diffusion coefficients are $D \geq 0.8 \text{ cm}^2/\text{Msec}$

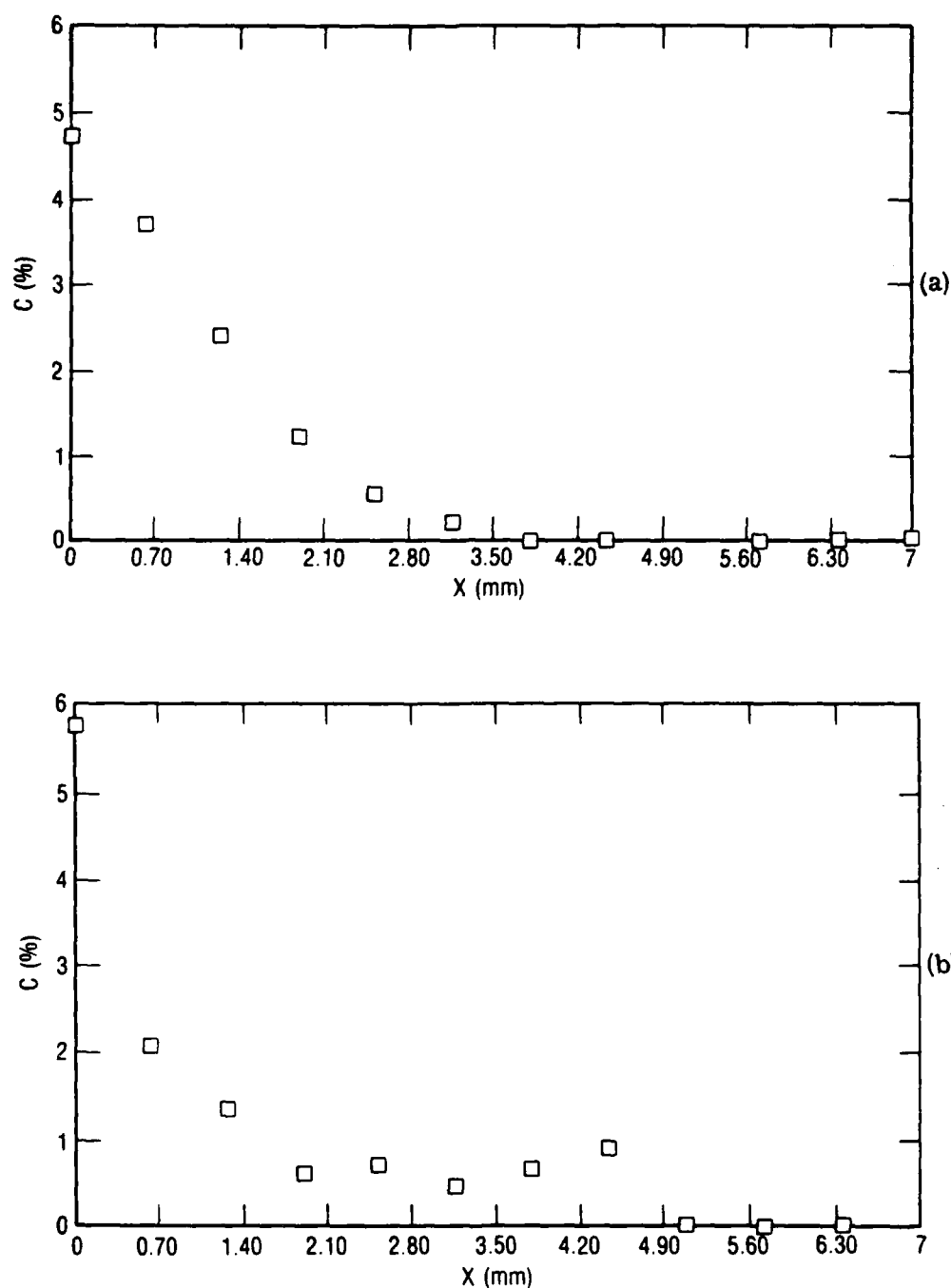


Fig. II-13. (a) Experimental (XPS) Diffusion Profile for Unfilled Uralane After 12 Days of HF Exposure. (b) Experimental (XPS) Diffusion Profile for Alumina-Filled Uralane After 12 Days of HF Exposure.

(unfilled) and $D \geq 0.1 \text{ cm}^2/\text{Msec}$ (filled). These D values are consistent with the T_g phenomena previously described and with the range of values seen in Table II-1. As noted, only measurements over shorter times would completely specify both D and H .

F. SUMMARY

The Aerospace Materials Sciences Laboratory has investigated the assumption that the barrier effectiveness of a polymeric liner will be improved by adding filler particles that can inhibit the flow of HF gas. The transport coefficients of the liner materials must be determined before multislabs calculations can reveal the extent to which the barrier reduces the HF flux at the metal substrate. These transport coefficients can be determined from one-dimensional diffusion experiments in which the HF concentration profiles are measured by XPS. Several such profiles must be measured in order to determine both the basic diffusion coefficient, D , and a second parameter, H , specifying the degree of chemical reactivity between the gas and the liner material. The current experiments (21 h and 12 days long) on a model polymer with and without alumina particles (40 wt% of $10 \pm 2\text{-}\mu\text{m}$ particles) are consistent with $H \geq 13 \text{ Msec}^{-1}$ for either filled or unfilled polymer: $D \geq 0.8 \text{ cm}^2/\text{Msec}$ (unfilled) and $D \geq 0.1 \text{ cm}^2/\text{Msec}$ (filled). In Section IV, we will determine D and H for several different filler types.

Mathematical modeling established that diffusion can be significantly impeded by high values of the interaction parameter, H . Debonding between filler and matrix may partially offset this gain. In addition, other researchers have shown that the presence of filler particles immobilizes polymer segments, raises the polymeric glass transition temperature, and reduces the diffusion coefficient, D . For example, the T_g of poly(vinyl acetate - vinyl chloride) can be raised from 30 to 51°C by appropriate loading.¹² Any such increase will lead to a reduced diffusion coefficient. The most dramatic decrease occurs for a polymer system in which the loading elevates T_g from below the operating temperature to above it. We suggest that this effect explains the restricted HF penetration into our

filled polymers. Further testing is in progress to determine the T_g of filled and unfilled Uralane.

Phenomenologically, the description of diffusion in terms of D and H is consistent with the existence of a time-dependent diffusion coefficient, which may be considered to arise microscopically from the clogging of diffusion channels by reaction products. The consequences of such hindered diffusion in a layered system will be described in the next section.

III. CALCULATION OF HF FLUX AT THE METAL SUBSTRATE

A. BACKGROUND

The liner considered here must serve as a barrier to corrosive HF gas. In this section, the fraction of the evolved HF particles that can diffuse through the liner and arrive at the metal substrate is calculated for some typical values of component thicknesses, diffusion coefficients (matrix D_1 and liner D_2), and liner reactivity with HF. Figure 1-3 may be consulted in order to visualize the geometry and parameters. A barrier effectiveness, τ , is defined such that $\tau = 100\%$ when no HF ever reaches the metal substrate.

In Section I, a method for quantifying the resistance of filled polymers to gaseous HF diffusion was developed on the basis of (1) concentration profile measurements from one-dimensional diffusion experiments and (2) the assumption of a particular phenomenological diffusion model. Experiments on a model polymer with and without filler indicated that the diffusion coefficient, D , is at least $0.8 \text{ cm}^2/\text{Msec}$ (unfilled) and at least $0.1 \text{ cm}^2/\text{Msec}$ (filled). In either case, the parameter, H , specifying the reactivity of the gas and the decrease of D with time, was found to be at least 13 Msec^{-1} . Using these results, as well as literature values for the diffusion coefficients of common polymers, we calculated the barrier effectiveness, τ , for several sets of parameters. The ratio of the total number of HF particles arriving at a lined metal substrate surface to the total number of HF particles arriving when unlined is $(1 - \tau/100\%)$.

B. PHYSICAL MODEL FOR THE DIFFUSION OF REACTIVE GASES OUT OF A MATRIX, THROUGH A LINER, AND ONTO A METAL SUBSTRATE

Consider a one-dimensional slab of a gas-evolving matrix material between positions $x = -l_1$ and $x = 0$ (see Fig. 1-3). An adjacent, one-dimensional slab of liner material lies between $x = 0$ and $x = l_2$. The matrix material is characterized by a diffusion coefficient, D_1 , and an evolution rate per length, $G e^{-gt}$, for HF gas. The concentration of HF gas

in the matrix is $c_1(x,t)$, where t is time. Similarly, the HF concentration in the liner is $c_2(x,t)$. The liner is characterized by a diffusion coefficient, D_2 , and a rate of gas/liner reaction, $-Hc_2(x,t)$, which reduces the value of D_2 , as discussed in Section II. The initial values for c_1 and c_2 are zero for $-l_1 < x < l_2$. The boundary value at $x = -l_1$ is that each incident molecule is lost to the inert region, never to return. (The opposite case, where no molecules are lost to the inert region, is also straightforward but is not considered here.) The boundary value at $x = l_2$ is that every molecule that arrives at the metal substrate reacts with the metal and is immobilized. The continuity condition at $x = 0$ is that the fluxes, $J_1 = -D_1 \partial_x c_1$, and the concentrations, c_i , are continuous.

The barrier effectiveness, τ , is defined by

$$\tau = \left[1 - \frac{\int_0^\infty J_2(l_2, t) dt}{\frac{1}{2} \int_{-l_1}^0 \int_0^\infty G e^{-gt} dt dx} \right] \times 100\% \quad (18a)$$

$$\tau = \left[1 + \frac{D_2 \int_0^\infty \partial_x c_2|_{l_2} dt}{\frac{Gl_1}{2g}} \right] \times 100\% \quad (18b)$$

The denominator in τ is the total number of HF particles arriving at the metal substrate in an unlined system, i.e., half the total number of evolved particles, since half of them "get lost" in the inert material (sink). The barrier effectiveness, τ , varies between 0% (when half of the evolved HF impinges upon the metal substrate just as if no liner were present) and 100% (when none of the HF ever arrives at the metal substrate). We have to solve the partial differential equations suggested by Fig. I-3 in order to calculate τ .

The mathematical problem consists of partial differential equations (PDE), boundary conditions (BC), and initial conditions (IC):

$$\text{PDE} \quad \begin{cases} D_1 \nabla^2 c_1 + G e^{-gt} = \partial_t c_1 & -l_1 < x < 0 \\ D_2 \nabla^2 c_2 - H c_2 = \partial_t c_2 & 0 < x < l_2 \end{cases} \quad \begin{matrix} (19a) \\ (19b) \end{matrix}$$

$$\text{BC} \quad \begin{cases} D_1 \partial_x c_1|_0 = D_2 \partial_x c_2|_0 & t > 0 \\ c_1(0, t) = c_2(0, t) \\ c_1(-l_1, t) = 0 \\ c_2(l_2, t) = 0 \end{cases} \quad \begin{matrix} (20a) \\ (20b) \\ (20c) \\ (20d) \end{matrix}$$

$$\text{IC} \quad \begin{cases} c_1(x, 0) = 0 & -l_1 < x < 0 \\ c_2(x, 0) = 0 & 0 < x < l_2 \end{cases} \quad \begin{matrix} (21a) \\ (21b) \end{matrix}$$

Taking the Laplace transforms of Eqs. (19a)-(19b) and using Eqs. (21a) and (21b), we obtain

$$\nabla^2 \bar{c}_1 - \omega_1^2 \bar{c}_1 = \frac{-G}{D_1(s + g)} \quad (22a)$$

$$\nabla^2 \bar{c}_2 - \omega_2^2 \bar{c}_2 = 0 \quad (22b)$$

$$\omega_1 = \sqrt{s/D_1} \quad (22c)$$

$$\omega_2 = \sqrt{(s + H)/D_2} \quad (22d)$$

Equations (22a)-(22b) have the solutions

$$\bar{c}_1(s) = A_1 \cosh \omega_1 x + B_1 \sinh \omega_1 x + \frac{G}{s(s+g)} \quad (23a)$$

$$\bar{c}_2(s) = A_2 \cosh \omega_2 x + B_2 \sinh \omega_2 x \quad (23b)$$

Applying Eqs. (20a)-(20d) to Eqs. (23a)-(23b), we obtain

$$C_d = D_2 \omega_2 \cosh \omega_2 l_2 \sinh \omega_1 l_1 + D_1 \omega_1 \cosh \omega_1 l_1 \sinh \omega_2 l_2 \quad (24a)$$

$$C_d \cdot A_1 = \frac{-G}{s(s+g)} (D_2 \omega_2 \cosh \omega_2 l_2 \sinh \omega_1 l_1 + D_1 \omega_1 \sinh \omega_2 l_2) \quad (24b)$$

$$C_d \cdot B_1 = \frac{-G}{s(s+g)} \cdot D_2 \omega_2 \cosh \omega_2 l_2 (\cosh \omega_1 l_1 - 1) \quad (24c)$$

$$C_d \cdot A_2 = \frac{G}{s(s+g)} \cdot D_1 \omega_1 \sinh \omega_2 l_2 (\cosh \omega_1 l_1 - 1) \quad (24d)$$

$$C_d \cdot B_2 = \frac{-G}{s(s+g)} \cdot D_1 \omega_1 \cosh \omega_2 l_2 (\cosh \omega_1 l_1 - 1) \quad (24e)$$

The functions, Eqs. (23a)-(23b), with the coefficients, Eqs. (24a)-(24e), are the system response functions on the complex s-plane. In order to facilitate the following calculation, Eqs. (23a)-(23b) may be written more succinctly as

$$\bar{c}_i(s) = \frac{-G}{s(s+g)} \left[\frac{\hat{A}_i(s) \cosh \omega_i x + \hat{B}_i(s) \sinh \omega_i x}{C_d(s)} + \delta_{i1} \right] \quad (25a)$$

where $i = 1, 2$, δ_{ij} is the Kronecker delta (1 for $i = j$ and 0 for $i \neq j$), ω_i is given by Eqs. (22c)-(22d), $C_d(s)$ is given by Eq. (24a), and

$$\hat{A}_1 = D_2 \omega_2 \cosh \omega_2 l_2 \sinh \omega_1 l_1 + D_1 \omega_1 \sinh \omega_2 l_2 \quad (25b)$$

$$\hat{B}_1 = D_2 \omega_2 \cosh \omega_2 l_2 (\cosh \omega_1 l_1 - 1) \quad (25c)$$

$$\hat{A}_2 = -D_1 \omega_1 \sinh \omega_2 l_2 (\cosh \omega_1 l_1 - 1) \quad (25d)$$

$$\hat{B}_2 = D_1 \omega_1 \cosh \omega_2 l_2 (\cosh \omega_1 l_1 - 1) \quad (25e)$$

We observe that $\lim_{s \rightarrow 0} \bar{c}_i(s)$ is finite for either $i = 1$ or 2 . (Note that there are cancelling divergent terms from \hat{A}_i and the Kronecker delta.) Hence there is no pole in $\bar{c}_i(s)$ at the origin. Similarly, $\lim_{s \rightarrow -g} \bar{c}_i(s)$ diverges as $(s + g)^{-1}$. Therefore, there is a simple pole at $s = -g$. There are also, potentially, poles for values of s that cause $C_d(s) = 0$. We note first that $s = 0$ and $s = -H$ cause $C_d(s) = 0$ but that $\lim_{s \rightarrow 0} \bar{c}_i(s)$ and $\lim_{s \rightarrow -H} \bar{c}_i(s)$ are nevertheless finite. Therefore, the roots $s = 0$ and $s = -H$ of $C_d(s) = 0$ must be rejected, i.e., there are no poles at the origin (seen previously) or at $s = -H$. All the remaining roots of $C_d(s) = 0$ are, in general, simple poles on the negative, real s axis (see Ref. 3) and are denoted by $s = s_n$, $n = 1, 2, 3, \dots$

There is, however, an exceptional condition on the poles of $\bar{c}_i(s)$ when $s = s_n = -g$ by coincidence. In this case, $\lim_{s \rightarrow s_n} \bar{c}_i(s)$ diverges as $(s - s_n)^{-2}$, i.e., there is a second-order pole at s_n . In this analysis, we restrict our choice of g so that this "coalescence" of poles never occurs. This simplifies the calculation without any significant loss of generality. If, by any chance, the required gas evolution rate were the same as one pole of the system response function, second-order residues could be calculated. The poles are summarized in Fig. III-1.

In order to determine the response functions $\bar{c}_i(s)$, it is necessary to numerically determine the roots (sketched in Fig. III-2) of $C_d(s) = 0$ (Eq. (24a), where

$$\omega_1 = i \sqrt{\frac{|s|}{D_1}} \quad (26a)$$

$$\omega_2 = i \sqrt{\frac{|s| - H}{D_2}} \quad \text{for } |s| > H \quad (26b)$$

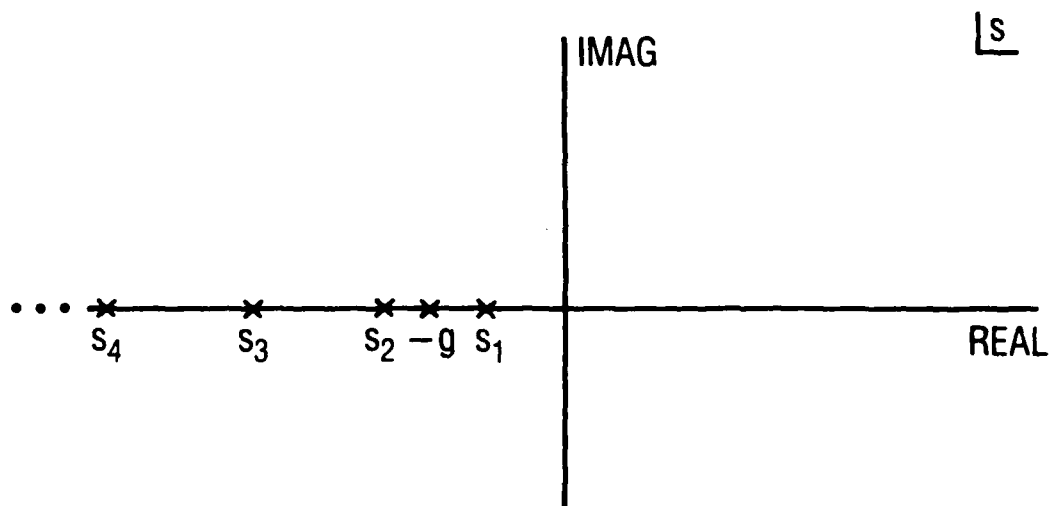


Fig. III-1. Pole Structure of the Response Function $\bar{c}_i(s)$. All the poles are simple if, as assumed, $s_n \neq -g$ for all n . There are no poles at $s = 0$ or $s = -H$.

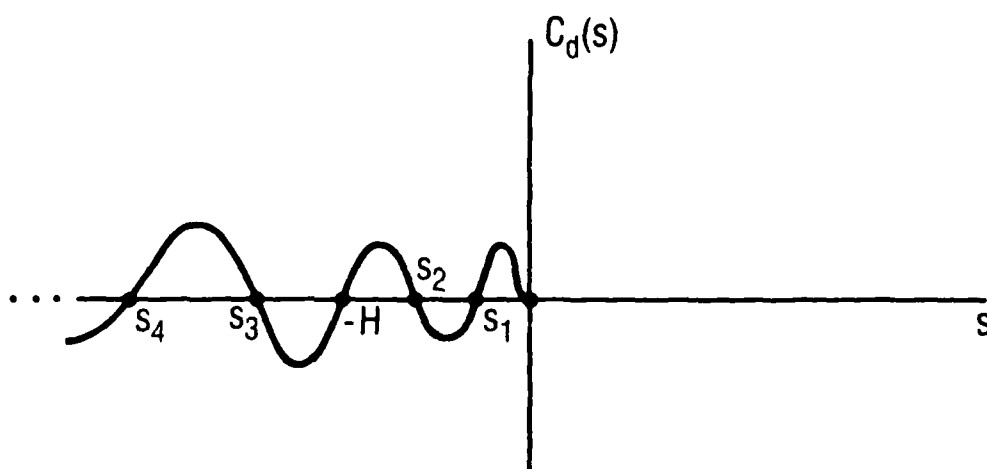


Fig. III-2. Roots of $C_d(s) = 0$ (excluding $s = 0$ and $s = -H$) Are Simple Poles of the Response Function $c_i(s)$. These roots must be found numerically.

$$\omega_2 = \sqrt{\frac{H - |s|}{D_2}} \quad \text{for } |s| < H \quad (26c)$$

When the roots are known, $\bar{c}_1(s)$ can be expanded according to the Mittag-Leffler theorem:

$$\bar{c}_1(s) = \frac{\text{Res}[\bar{c}_1(s), -g]}{s + g} + \sum_{n=1}^{\infty} \frac{\text{Res}[\bar{c}_1(s), s_n]}{s - s_n} \quad (27)$$

where $\text{Res}[\bar{c}_1(s), s_0]$ refers to the residue of $\bar{c}_1(s)$ at $s = s_0$.

Laplace-inverting Eq. (27), we obtain the response function in the time domain as

$$c_1(x, t) = \text{Res}[\bar{c}_1(s), -g] e^{-gt} + \sum_{n=1}^{\infty} \text{Res}[\bar{c}_1(s), s_n] e^{s_n t} \quad (28a)$$

where

$$\text{Res}[\bar{c}_1(s), -g] = \frac{-G}{g} \left[\frac{\hat{A}_1 \cosh \omega_1 x + \hat{B}_1 \sinh \omega_1 x}{C_d(s)} + \delta_{11} \right]_{s = -g} \quad (28b)$$

$$\text{Res}[\bar{c}_1(s), s_n] = \left[\frac{X_1(s)}{C'_d(s)} \right]_{s = s_n} \quad (28c)$$

$$X_1(s) = \frac{-G}{s(s + g)} [\hat{A}_1 \cosh \omega_1 x + \hat{B}_1 \sinh \omega_1 x + \delta_{11} \cdot C_d(s)] \quad (28d)$$

$$C'_d(s) = \frac{1}{2} \left(\frac{\cosh \omega_2 l_2 \sinh \omega_1 l_1}{\omega_2} + \frac{\cosh \omega_1 l_1 \sinh \omega_2 l_2}{\omega_1} \right) + \left(\frac{l_1 + l_2}{2} \right) \sinh \omega_2 l_2 \sinh \omega_1 l_1$$

$$+ \frac{1}{2} \left(\frac{l_1 D_2 \omega_2}{D_1 \omega_1} + \frac{l_2 D_1 \omega_1}{D_2 \omega_2} \right) \cosh \omega_1 l_1 \cosh \omega_2 l_2 \quad (28e)$$

When evaluating Eqs. (28a)-(28e), the replacements, Eqs. (26a)-(26c), should be performed separately for the different $|s_n| > H$ and $|s_n| < H$ regimes. Using $\cosh ix = \cos x$ and $\sinh ix = i \sin x$, we may keep track of the phases explicitly. Of course, $c_1(x,t)$ must be purely real and non-negative. In order to calculate ζ , the spatial derivative of $c_2(x,t)$ must be calculated [see Eq. (18b)]. This operation is performed on Eq. (28a), where the residues depend on x .

C. COMPUTER CALCULATION FOR THE BARRIER EFFECTIVENESS, ζ , OF FILLED POLYMERIC LINERS

The equations from the preceding section were programmed on the "DIRAC" VAX of the Aerospace Space Sciences Laboratory (SSL). Several matrix/liner systems were investigated, as shown in Table III-1. Eight cases, defined in Table III-1, were investigated, each case consisting of 12 possible combinations of parameters.

The time-dependent concentration profiles [$c_1(x,t)$ and $c_2(x,t)$] and cumulative fluxes (total evolved, incident at the inert sink, and incident at the metal substrate) are shown explicitly for three of the parameter combinations in Case I (Figs. III-3 to III-8) as well as for three of the parameter combinations in Case II (Figs. III-9 to III-14). The barrier effectiveness results for the eight cases are summarized in Tables III-2 to III-5. A detailed discussion of these results follows.

Figure III-3 shows the special case in which $-l_1 < x < l_2$ may be considered as one layer, because $D_1 = D_2$ and $H = 0$. In this case, the Sturm-Liouville theory is applicable, and the poles must be in the ratio of the squares of the positive integers. Appendix A shows that the present numerical calculation does give this result. Figure III-3 exhibits only a very slight (i.e., imperceptible) left-right asymmetry, because the HF is

Table III-1. Parameters Used in the Calculation of the Barrier Effectiveness, τ , of Several One-Dimensional Matrix/Liner Systems

1. Thicknesses		
matrix:	$-l_1 \leq x < 0$	liner: $0 \leq x \leq l_2$
2. HF generation rate in matrix = $G e^{-gt}$		
	$[G] = \text{particles}/(\text{cm} \cdot \text{Msec})$	
	$[g] = \text{Msec}^{-1}$	
3. HF reaction rate with liner = $-Hc_2(x,t)$		
	$[H] = \text{Msec}^{-1}$	
	$[c_2] = \text{particles}/\text{cm}$	
4. In all cases, $G = 10 \text{ particles}/(\text{cm} \cdot \text{Msec})$		
	$g^{-1} = 100 \text{ Msec} = 3.17 \text{ year}$	
	$\text{total HF} = \frac{Gl_1}{g} = 500.0 \text{ or } 277.0 \text{ particles}$	
	depending on the matrix thickness	
5. Diffusion coefficients matrix: D_1		liner: D_2
6. In all cases, $H = 0.0, 10, 100, \text{ and } 1000 \text{ Msec}^{-1}$, in sequence.		
7. Cases investigated		
Case I:	$D_1 = 1.0 \text{ cm}^2/\text{Msec}$	$l_1 = 0.277 \text{ cm}$
	$D_2 = 1.0, 0.1, 0.01$	$l_2 = 0.025$
	(see Figs. III-3 to III-8 and Table III-2)	
Case II:	$D_1 = 10.0$	$l_1 = 0.277$
	$D_2 = 10, 1.0, 0.1$	$l_2 = 0.025$
	(see Figs. III-9 to III-17 and Table III-2)	

Table III-1. Parameters Used in the Calculation of the Barrier Effectiveness, τ , of Several One-Dimensional Matrix/Liner Systems (Continued)

Case III:	$D_1 = 1.0$	$\tau_1 = 0.277$
	$D_2 = 1.0, 0.1, 0.01$ (see Table III-3)	$\tau_2 = 0.005$
Case IV:	$D_1 = 10$	$\tau_1 = 0.277$
	$D_2 = 10, 1.0, 0.1$ (see Table III-3)	$\tau_2 = 0.005$
Case V:	$D_1 = 1.0$	$\tau_1 = 0.500$
	$D_2 = 1.0, 0.1, 0.01$ (see Table III-4)	$\tau_2 = 0.025$
Case VI:	$D_1 = 10$	$\tau_1 = 0.500$
	$D_2 = 10, 1.0, 0.1$ (see Table III-4)	$\tau_2 = 0.025$
Case VII:	$D_1 = 1.0$	$\tau_1 = 0.500$
	$D_2 = 1.0, 0.1, 0.01$ (see Table III-5)	$\tau_2 = 0.005$
Case VIII:	$D_1 = 10$	$\tau_1 = 0.500$
	$D_2 = 10, 1.0, 0.1$ (see Table III-5)	$\tau_2 = 0.005$

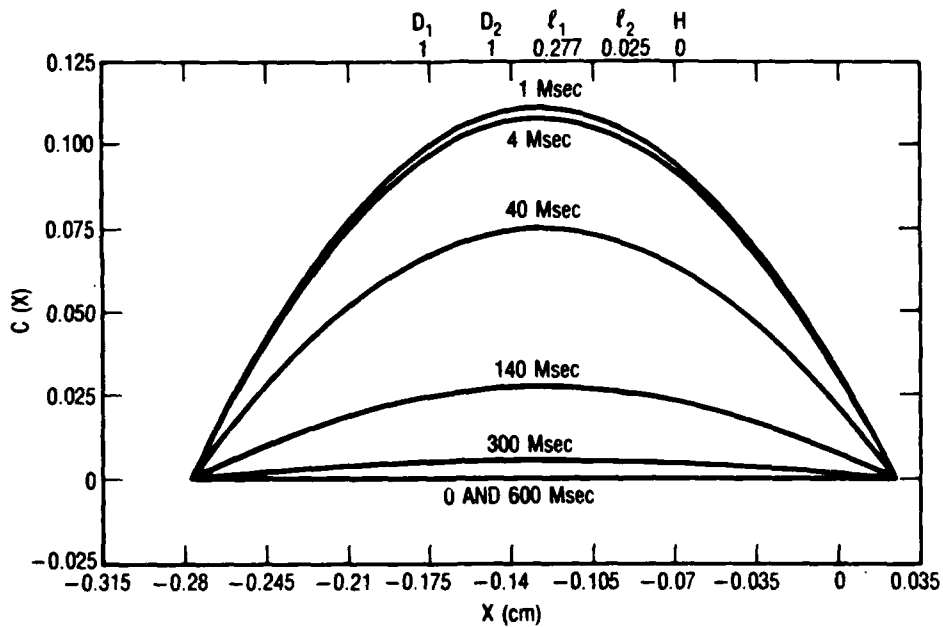


Fig. III-3. HF Concentration vs Position at Several Times. Since $D_1/D_2 = 1$, the fluxes at the metal (right) and at the sink (left) are virtually the same. Matrix: $x < 0$. Liner: $x > 0$. Parameters above figure.

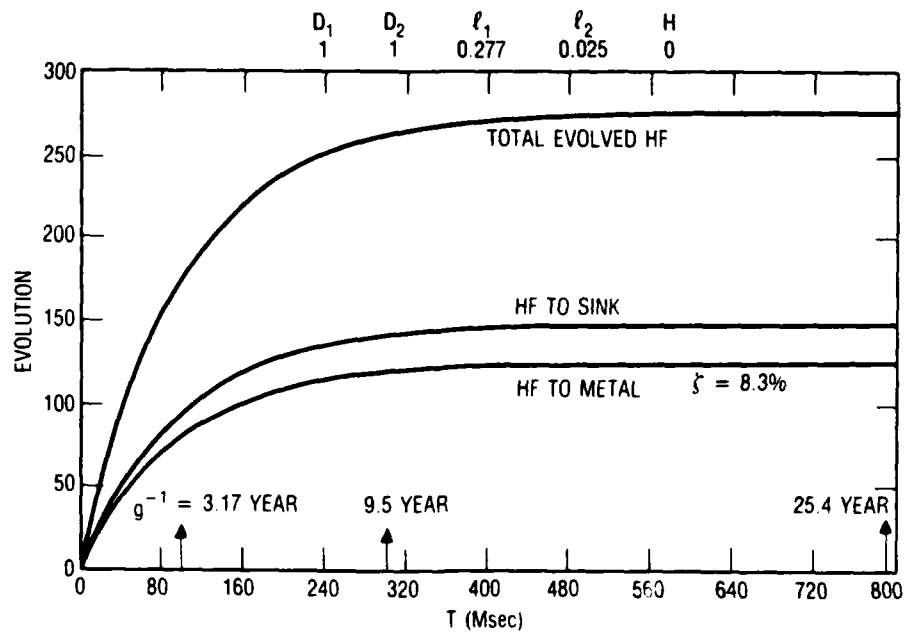


Fig. III-4. Time-Evolution of Total HF, HF at Sink (left), and HF at Metal (right), Corresponding to Fig. III-3. Parameters above figure.

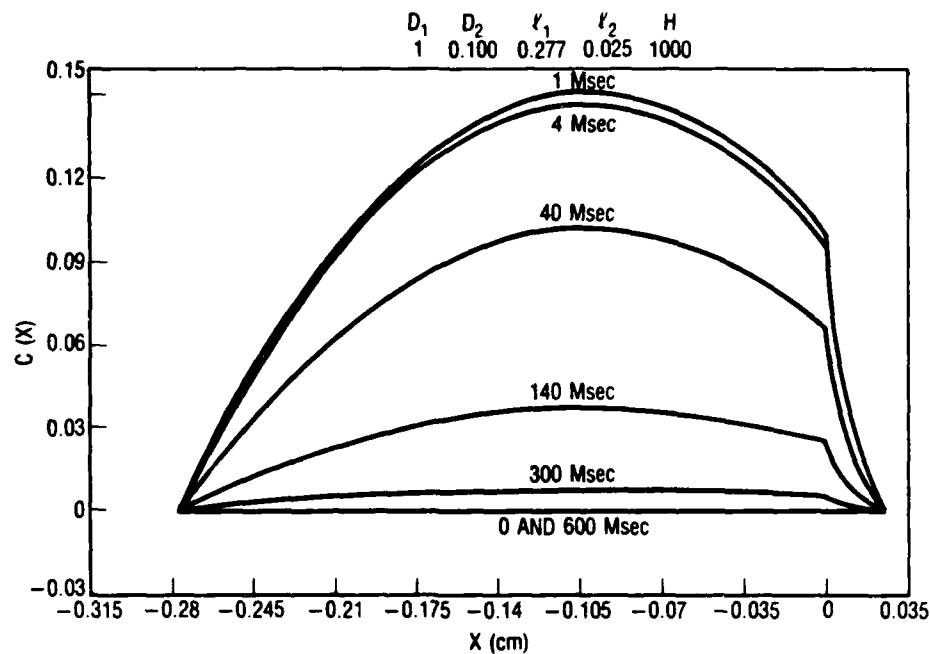


Fig. III-5. HF Concentration vs Position at Several Times. Since $D_1/D_2 = 10$, the flux at the metal (right) is less than that at the sink (left). Matrix: $x < 0$. Liner: $x > 0$. Parameters above figure.

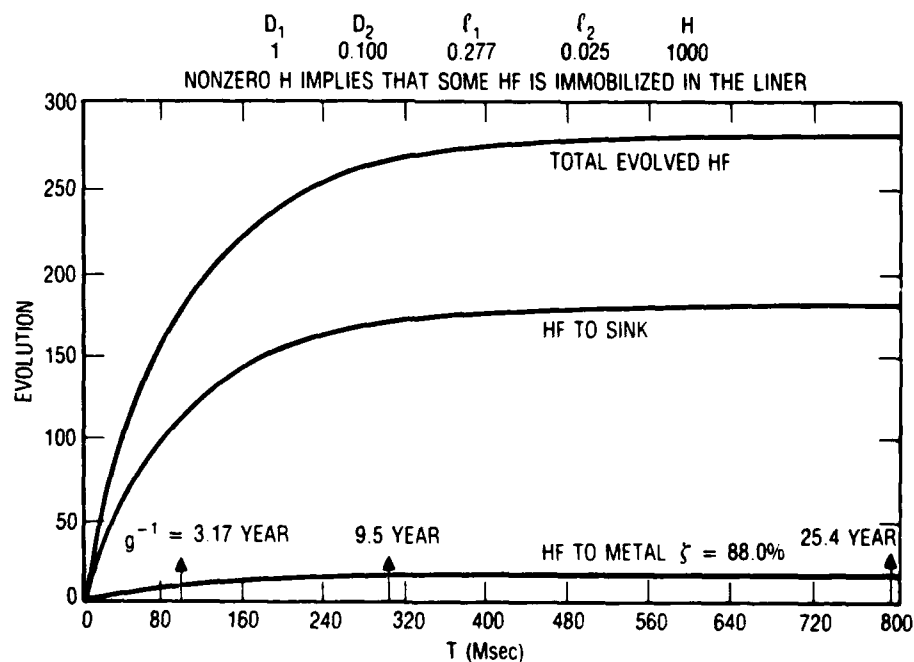


Fig. III-6. Time-Evolution of Total HF, HF at Sink (left), and HF at Metal (right), Corresponding to Fig. III-5. Parameters above figure.

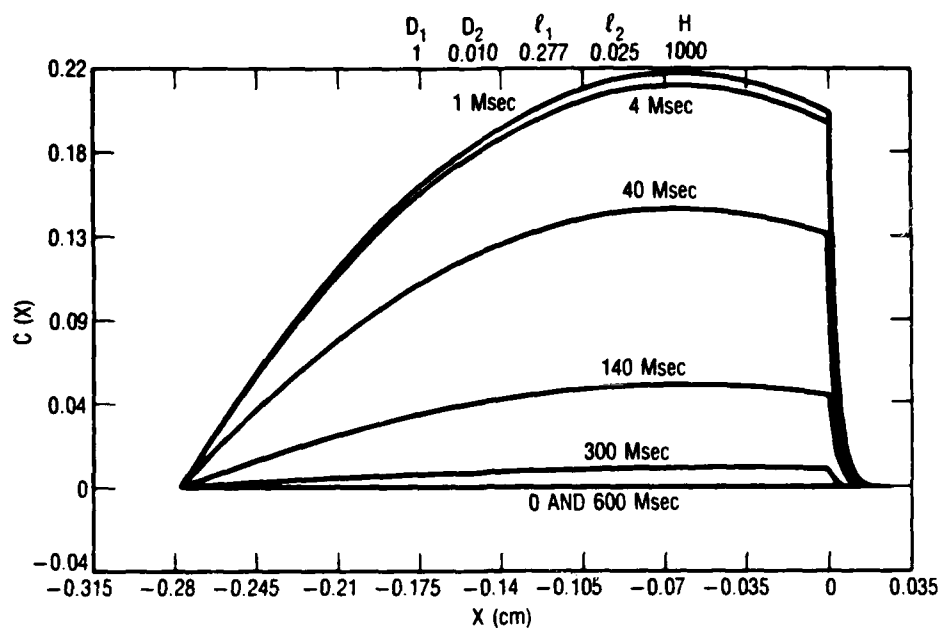


Fig. III-7. HF Concentration vs Position at Several Times. Since $D_1/D_2 = 100$, the flux at the metal (right) is less than that at the sink (left). Matrix: $x < 0$. Liner: $x > 0$. Parameters above figure.

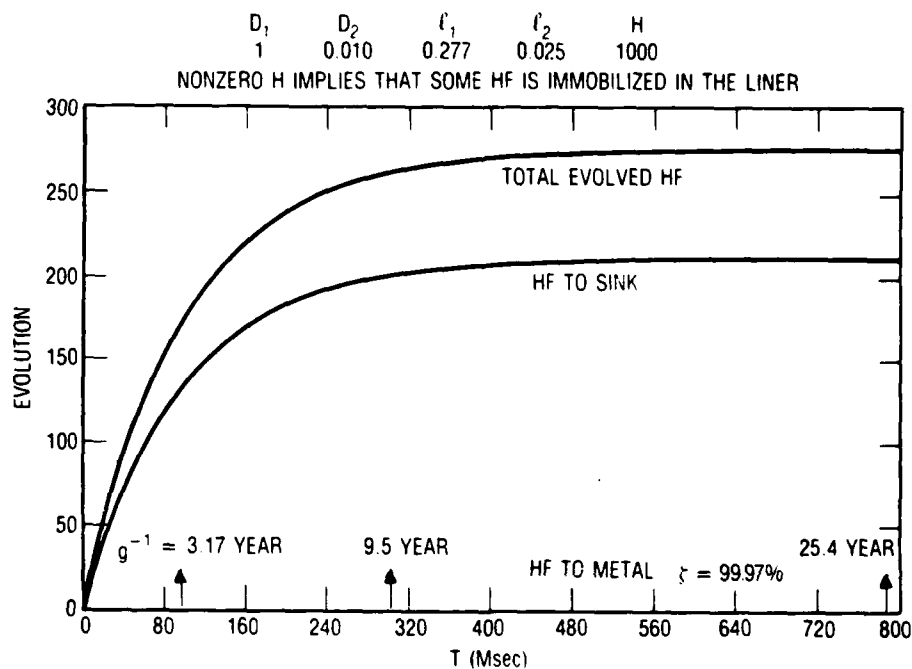


Fig. III-8. Time-Evolution of Total HF, HF to Sink (left), and HF to Metal (right), Corresponding to Fig. III-7. Parameters above figure.

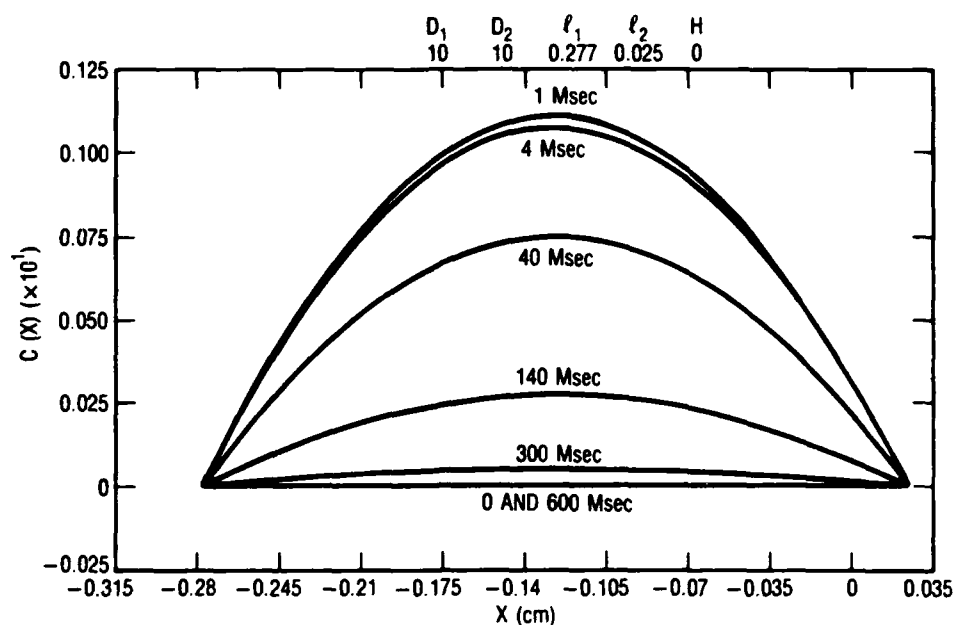


Fig. III-9. HF Concentration vs Position at Several Times. Since $D_1/D_2 = 1$, the fluxes at the metal (right) and at the sink (left) are virtually the same. Matrix: $x < 0$. Liner: $x > 0$. Parameters above figure.

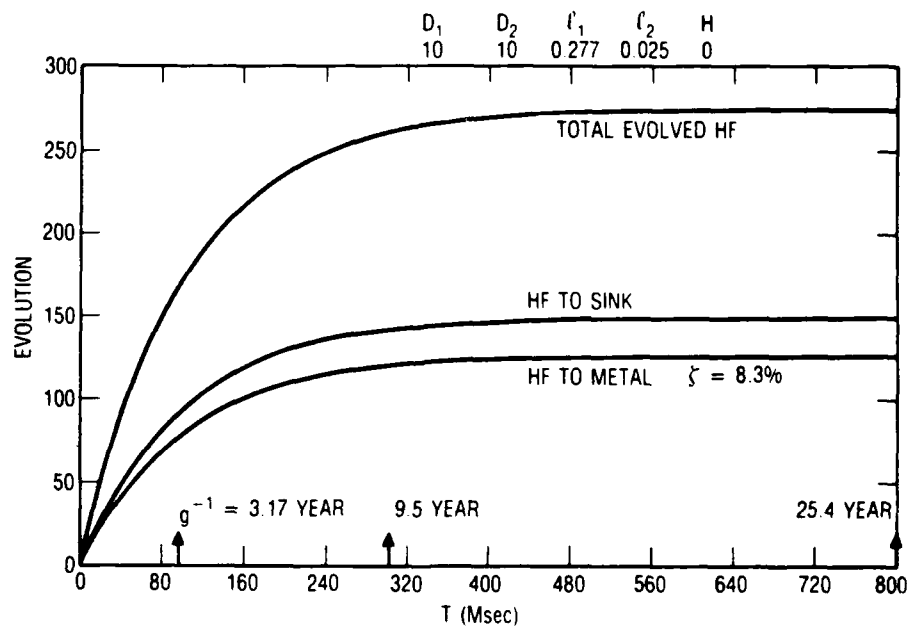


Fig. III-10. Time-Evolution of Total HF, HF at Sink (left) and HF at Metal (right), Corresponding to Fig. III-9. Parameters above figure.

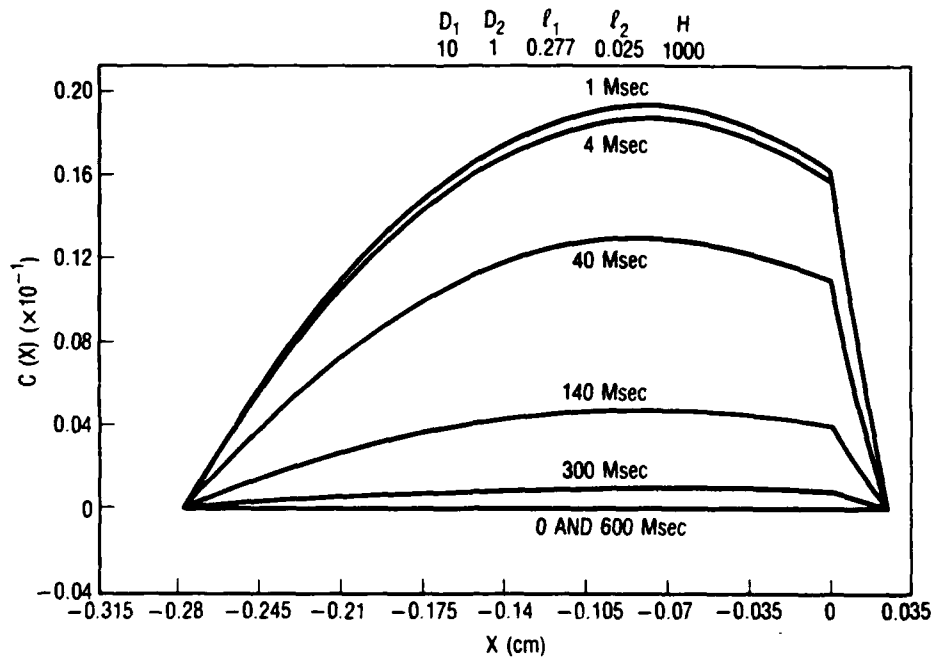


Fig. III-11. HF Concentration vs Position at Several Times. Since $D_1/D_2 = 10$, the flux at the metal (right) is less than that at the sink (left). Matrix: $x < 0$. Liner: $x > 0$. Parameters above figure.

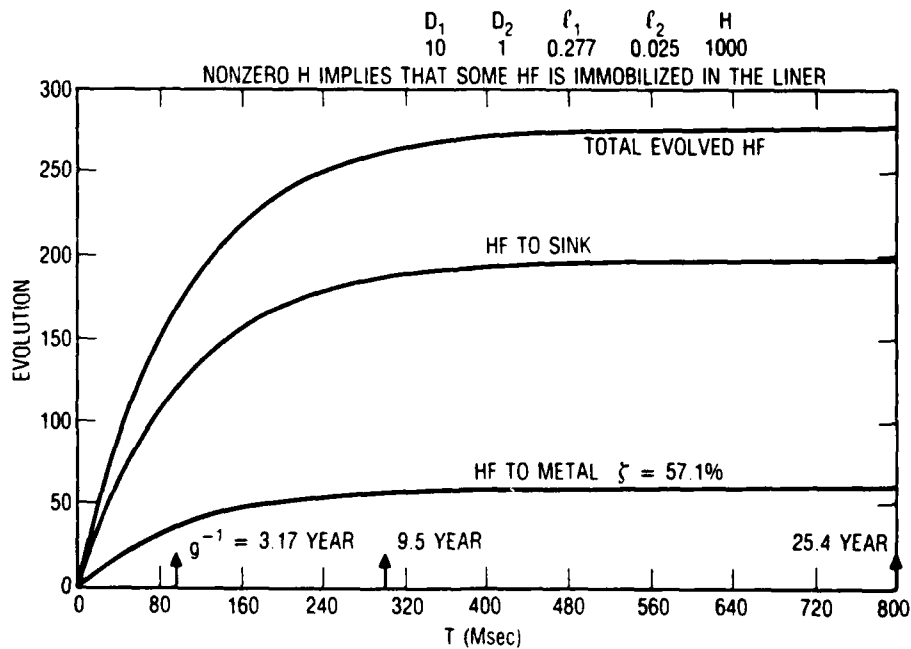


Fig. III-12. Time-Evolution of Total HF, HF to Sink (left), and HF to Metal (right), Corresponding to Fig. III-11. Parameters above figure.

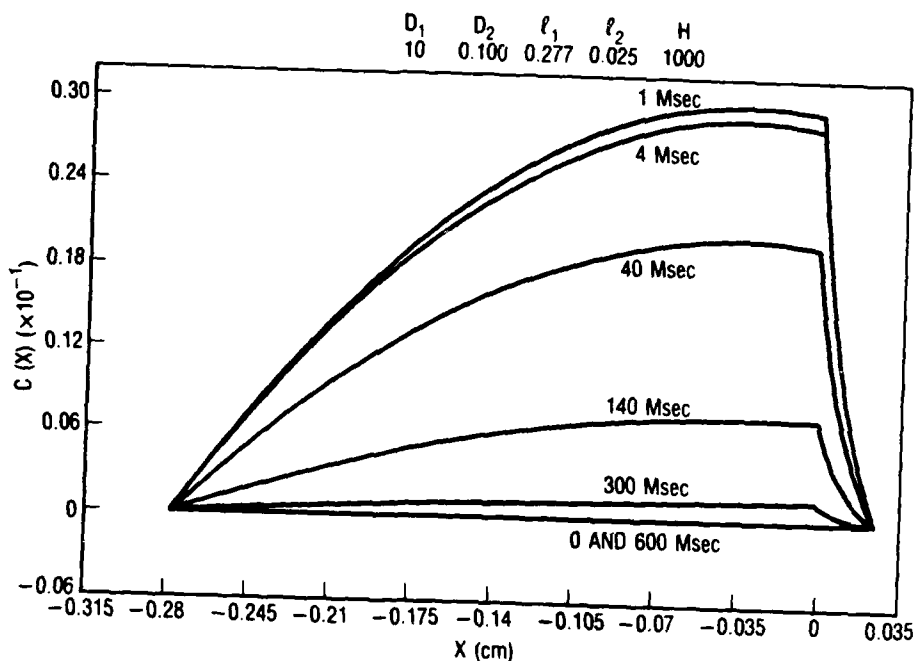


Fig. III-13. HF Concentration vs Position at Several Times. Since $D_1/D_2 = 100$, the flux at the metal (right) is less than that at the sink (left). Matrix: $x < 0$. Liner: $x > 0$. Parameters above figure.

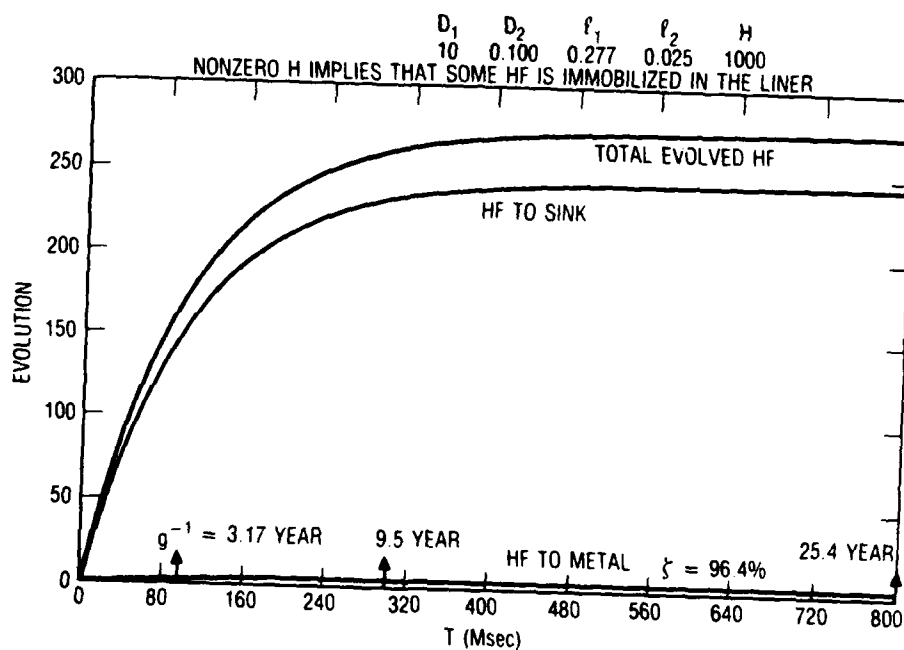


Fig. III-14. Time-Evolution of Total HF, HF to Sink (left), and HF to Metal (right), Corresponding to Fig. III-13. Parameters above figure.

Table III-2. Barrier Effectiveness, τ (%), for
Matrix/Liner = 0.277/0.025 cm

D_1/D_2 (cm^2/Msec)	H (Msec^{-1})			
	0.0	10.0	100.0	1000.0
1.0/1.0	8.3	8.6	10.9	30.0
1.0/0.1	47.4	48.5	57.1	88.0
1.0/0.01	90.0	91.2	96.4	99.97
10.0/10.0	8.3	8.3	8.5	10.9
10.0/1.0	47.4	47.5	48.5	57.1
10.0/0.1	90.0	90.1	91.2	96.4

Table III-3. Barrier Effectiveness, τ (%), for
Matrix/Liner = 0.277/0.005 cm

D_1/D_2 (cm^2/Msec)	H (Msec^{-1})			
	0.0	10.0	100.0	1000.0
1.0/1.0	1.8	1.8	1.9	3.0
1.0/0.1	15.3	15.4	16.2	24.0
1.0/0.01	64.3	64.6	66.8	80.7
10.0/10.0	1.8	1.8	1.8	1.9
10.0/1.0	15.3	15.3	15.4	16.2
10.0/0.1	64.3	64.4	64.6	66.8

Table III-4. Barrier Effectiveness, τ (%), for
Matrix/Liner = 0.500/0.025 cm

D_1/D_2 (cm^2/Msec)	H (Msec^{-1})			
	0.0	10.0	100.0	1000.0
1.0/1.0	4.8	5.1	7.6	27.8
1.0/0.1	33.3	34.9	46.9	86.4
1.0/0.01	83.3	85.4	94.5	99.95
10.0/10.0	4.8	4.8	5.0	7.6
10.0/1.0	33.3	33.5	34.9	46.9
10.0/0.1	83.3	83.6	85.4	94.5

Table III-5. Barrier Effectiveness, τ (%), for
Matrix/Liner = 0.500/0.005 cm

D_1/D_2 (cm^2/Msec)	H (Msec^{-1})			
	0.0	10.0	100.0	1000.0
1.0/1.0	1.0	1.0	1.1	2.2
1.0/0.1	9.1	9.2	10.2	18.8
1.0/0.01	50.0	50.4	53.9	75.0
10.0/10.0	1.0	1.0	1.0	1.1
10.0/1.0	9.1	9.1	9.2	10.1
10.0/0.1	50.0	50.0	50.4	53.9

generated only in the region $x < 0$. The HF concentration rises to a maximum before 1 Msec (278 h or 11.6 days). The maximum HF concentration occurs close to the center of the matrix/liner composite, where the HF accumulates before it can escape at the inert sink (at the left of the composite) or at the metal substrate (at the right of the composite). By 40 Msec (464 days), the maximum HF concentration has decreased to about two-thirds of its highest value. By 300 Msec (9.5 years), the maximum HF concentration is down to a few percent of its highest value. The diffusion relaxation time is 0.00924 Msec, which is equal to $(l_1 + l_2)^2/D_1^2$. In contrast, the characteristic time for HF evolution is $g^{-1} = 100$ Msec (3.17 years). The overall system relaxation time is determined by the longer of these two times, i.e., the characteristic time for HF evolution. This is clearly seen in Fig. III-3.

Figure III-4 shows the cumulative HF flux evolved and the fractions of that cumulative flux incident at the inert sink and at the metal substrate. The cumulative numbers of particles at the metal substrate and at the inert sink add up to the total evolved number of HF particles as time tends to infinity. This is true because $H = 0$ and no HF is bound up in the system for long times. The cumulative fluxes at the inert sink and at the metal substrate would be equal and ζ would be zero [see Eq. (18a)], except that the HF is generated only for $x < 0$. This geometric bias confers a small positive value on ζ , in this case, 8.3%.

Figure III-5 shows the case of $D_1 = 1 \text{ cm}^2/\text{Msec}$, $D_2 = 0.1 \text{ cm}^2/\text{Msec}$, $H = 1000 \text{ Msec}^{-1}$, $l_1 = 0.277 \text{ cm}$, and $l_2 = 0.025 \text{ cm}$. A sharp break in the slopes can be seen at $x = 0$, because the fluxes and not the slopes are continuous at that location. The slopes are reduced on the metal substrate (right) side compared to the inert sink (left) side. Because there is also less D_2 in the liner, the flux arriving at the metal substrate is less than that arriving at the inert sink for two reasons: a smaller concentration gradient and a smaller diffusion coefficient. Appendix B indicates that the poles are not in the ratio of the squares of the integers, because $D_1 \neq D_2$ and $H > 0$.

The reduction in flux arriving at the wall is readily apparent in Fig. III-6. According to Eq. (18a) or (18b), the barrier effectiveness, ζ , is 88%. Note that, in this case, the numbers of HF particles having arrived at the inert sink and at the metal substrate at cumulative times do not add up to the total number of evolved HF particles. This is true because $H \neq 0$, and some HF particles are immobilized in the liner.

The enhanced value of ζ (in Fig. III-6 compared to Fig. III-4) results from a liner diffusion coefficient (D_2) which is less than that of the matrix (D_1), as well as from the reactivity (H) of the gas with the liner. In Section II, it is shown that H specifies a rate of decrease of D_2 , which can be interpreted as a progressive diffusion-channel clogging.

A discussion follows of the molecular basis for the existence of a reduced D_2 in a filled polymer liner (see also Ref. 12). At temperatures below the polymer glass transition temperature, T_g , gas molecules must diffuse by jumping between fixed free-volume sites, which is a relatively slow process. For $T > T_g$, increased segmental motion and a higher free-volume content allow faster diffusion. Filler particles immobilize polymer segments and raise the effective T_g of the polymer/filler composite. For a given polymer at a given operating temperature, an unfilled system may be above its T_g (high D), while the corresponding filled system may be below its T_g' (low D). Not all filled systems exhibit the drastic effect of raising T_g above the operating temperature, but any increase in T_g results in some reduction in D .

Figure III-7 shows the case in which D_2 is down by two orders of magnitude from D_1 , with $H = 1000 \text{ Msec}^{-1}$. In this case, the slope discontinuity in the concentration profile at $x = 0$ is sharper, and the concavity for $x > 0$ is more pronounced. The slopes at the metal substrate (right side) remain virtually zero at all times. The success of this liner in keeping HF away from the metal substrate is shown in Fig. III-8. Note again that the plateau values for the cumulative number of particles at the inert sink and at the metal substrate as time tends to infinity do not add up to the total evolved number of HF particles, because $H \neq 0$, leaving some HF immobilized in the liner. Virtually no HF reaches the wall ($\zeta = 99.97\%$).

In comparison to Figs. III-3 to III-8, higher overall diffusion coefficients are shown in Figs. III-9 to III-14. Figures III-9 and III-10 are virtually identical to Figs. III-3 and III-4. The reason is as follows. The diffusion relaxation time in Figs. III-3 and III-4 is 0.00924 Msec. The diffusion relaxation time in Figs. III-9 and III-10 is 0.000924 Msec, being proportional to D^{-1} . However, the overall system relaxation time is dominated by the characteristic HF evolution time, $g^{-1} = 100$ Msec. Hence, the change of scale of D is virtually irrelevant.

In contrast, the case in Figs. III-11 and III-12 shows a significant difference compared to Figs. III-5 and III-6, even though the ratio of matrix to liner diffusion coefficients is the same. The concavity of the concentration profile within the liner is reduced, while the slopes at the metal substrate are increased. The barrier effectiveness, τ , is reduced to 57.1% in Fig. III-12 (it had been 88% in Fig. III-6). Figures III-13 and III-14 show the concentration profiles and cumulative fluxes for $D_1/D_2 = 100$ (compare to Figs. III-7 and III-8). There is still a fair amount of concavity in the liner concentration profiles. Only slightly more HF arrives at the metal substrate ($\tau = 96.4\%$ compared to 99.97% in Fig. III-8).

The barrier effectiveness results for all the cases listed in Table III-1 are presented in Tables III-2 to III-5. The liner thicknesses are either 0.025 cm (about 10 mils) or 0.005 cm (about 2 mils).

In the first row (the horizontal listing) of Tables III-2 and III-4, there is a substantial increase of τ with increasing H at $D_1/D_2 = 1$. However, the maximum τ is only about 30%. In all the other rows of Tables III-2 to III-5, there is only a modest increase of τ with increasing H . In contrast, there is always a large τ increase in each column (the vertical listing) in Tables III-2 to III-5, where D_1/D_2 increases at constant H . This shows that, of the two effects caused by filler particles (i.e., reduced D_2 and increased H), the D_2 reduction is far more important in increasing τ . This result indicates that it is useful to define a logarithmic diffusion-coefficient ratio as

$$R = \log(D_1/D_2) \quad (29)$$

For matrix and liner thicknesses of 0.277 and 0.025 cm, respectively, and $R = 2$, Tables III-2 to III-5 show that barrier effectiveness in excess of 90% can be achieved. In contrast, matrix/liner thicknesses of 0.277/0.005 cm result in $\tau \geq 65\%$ for $R = 2$. For matrix/liner thicknesses of 0.500/0.025 and 0.500/0.005, the τ values are at least 83%/50% for $R = 2$.

Figure III-15 shows τ plotted as a continuous function of D_2 (l_2 is a parameter). Most of the increase in τ occurs for $D_2 < 0.1 \text{ cm}^2/\text{Msec}$, corresponding in this case to $R > 1$. Finally, in Fig. III-16, τ is plotted as a continuous function of l_2 (D_2 is a parameter). Larger τ values are achieved for thinner liners when $R = 2$ (top curve) compared to $R = 1$ (lower curve).

D. COMPUTER CALCULATIONS OF THE BARRIER EFFECTIVENESS, τ , FOR A REALISTIC CASE OF A FILLED POLYMER CONTAINING DEFECTS

In Section II, single-slab, diffusion-profile measurements at two HF exposure times led to estimates of the diffusion coefficients of an unfilled and of a filled (Al_2O_3) model polymer (Uralane 5753). The diffusion coefficient, D_2 , of the unfilled system was estimated to be at least $0.8 \text{ cm}^2/\text{Msec}$ and of the filled system, at least $0.1 \text{ cm}^2/\text{Msec}$. In either case, H was at least 13 Msec^{-1} . Until measurements at additional times are available, we provisionally assign $D_2 = 0.8 \text{ cm}^2/\text{Msec}$ to the unfilled system, $D_2 = 0.1 \text{ cm}^2/\text{Msec}$ to the filled system, and $H = 13 \text{ Msec}^{-1}$ in either case. Further assuming that $D_1 = 1 \text{ cm}^2/\text{Msec}$, which is common for gas diffusion in typical polymers (see Section II), we can calculate the barrier effectiveness, τ , of the model polymer in both its unfilled and filled states. Of course there are other mechanical, thermal, and adhesion properties that have to be evaluated in the selection of an actual liner. This calculation merely illustrates what could be achieved in an actual system.

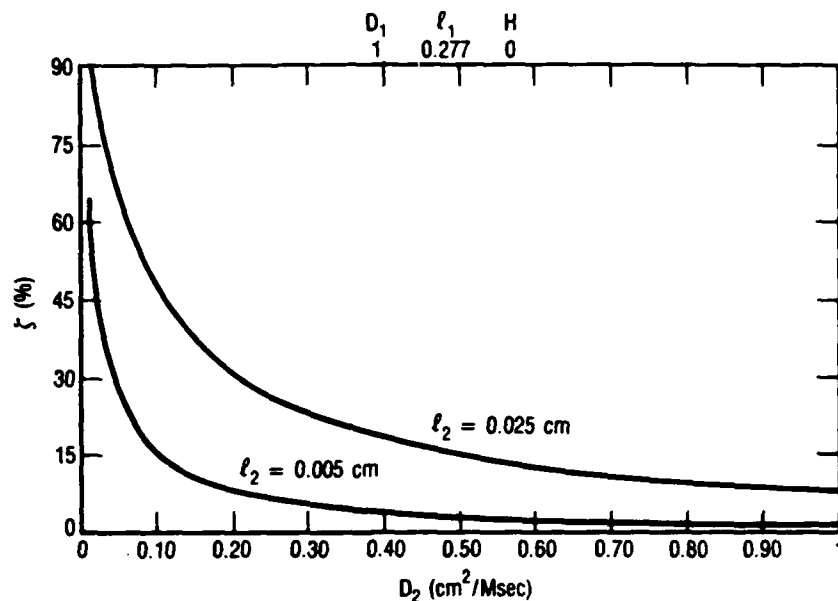


Fig. III-15. Barrier Effectiveness, ζ , vs the Liner Diffusion Coefficient, D_2 , for Two Values of Liner Thickness. Parameters above figure.

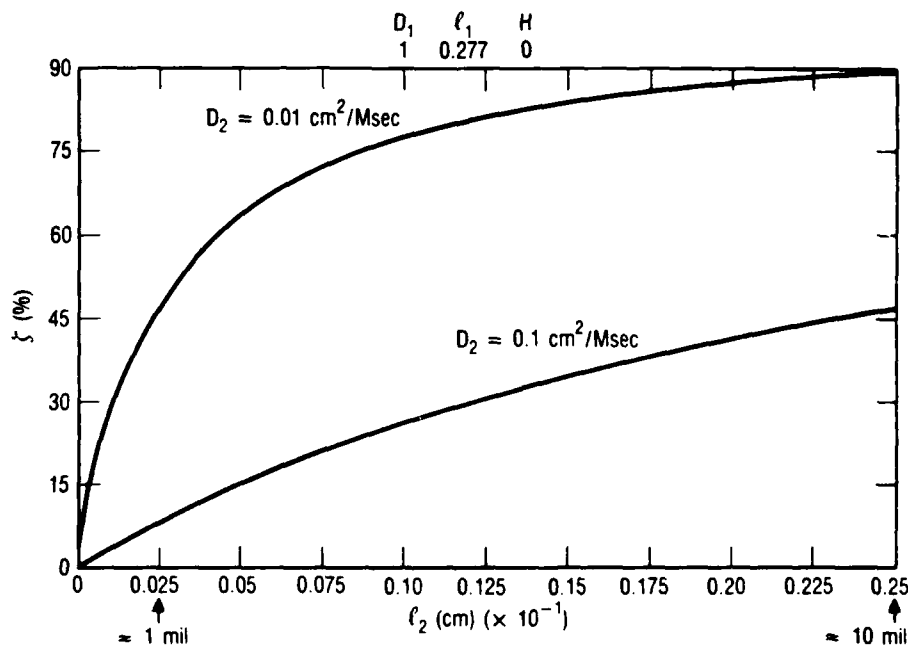


Fig. III-16. Barrier Effectiveness, ζ , vs the Liner Thickness, ℓ_2 , for Two Values of the Liner Diffusion Coefficient, D_2 . Parameters above figure.

In Figs. III-17 and III-18, we see that the barrier effectiveness of the unfilled system is very small ($\tau = 10.6\%$), as expected for $R = \log(D_1/D_2) = \log(1/0.8) = 0.097$. Because of the weak H dependence noted above, the system may be considered to exist at $D_2 = 0.8$ on the top curve in Fig. III-15. In Figs. III-19 and III-20, we see that τ for the filled system is much larger ($\tau = 48.9\%$), because $R = 1$. The system may be considered to exist at $D_2 = 0.1$ on the top curve in Fig. III-15 and at $x_2 = 0.025$ (extreme right) on the lower curve in Fig. III-16. These initial results possibly indicate that actual liner systems can be designed with $R \rightarrow 2$ and $\tau \rightarrow 90\%$.

Objections have been made that the experimental, single-slab HF concentration profiles of the Al_2O_3 -filled polymer in Section II do not look exactly like the computed curves in Fig. III-21. Specifically, the experimental data show a low-level plateau (for $x > 0.3$ cm), which is not evident in the computed model response. In contrast, the experimental response of the unfilled system does match the computed curves. The low level of additional diffusion is attributed to some unspecified defect in the filled system. One possible, but unverified, explanation is that cracks have developed between filler and polymer, allowing additional diffusion. It has been speculated that this could be a "fatal" drawback to the use of filled polymers as liners. We show in the following discussion, however, that the observed effect is consistent with only a small reduction in the barrier effectiveness, τ .

The effect of the defects can be modeled by assuming that some fraction of the diffusing species finds faster diffusion pathways, which may be traversed in parallel with diffusion through the polymer. The single-slab response of such a faster pathway is shown in Fig. III-22, where $D = 1$ and $H = 0$ in contrast to Fig. III-21 ($D = 0.1$ and $H = 13$). It is essential that $H = 0$ in such a pathway, so that the slope is zero at long times, as observed experimentally.

Considering parallel pathways in which 90% of the particles diffuse through the polymer and 10% through the defect channels, we compute the

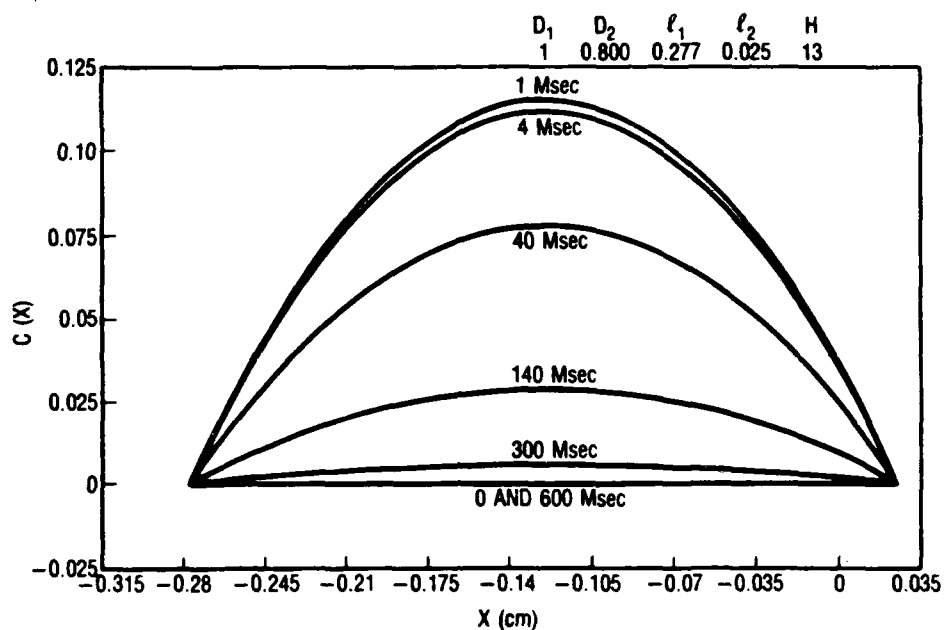


Fig. III-17. HF Concentration vs Position at Several Times, Corresponding to an Unfilled Model-Polymer Liner as Measured in Section II. Parameters above figure.

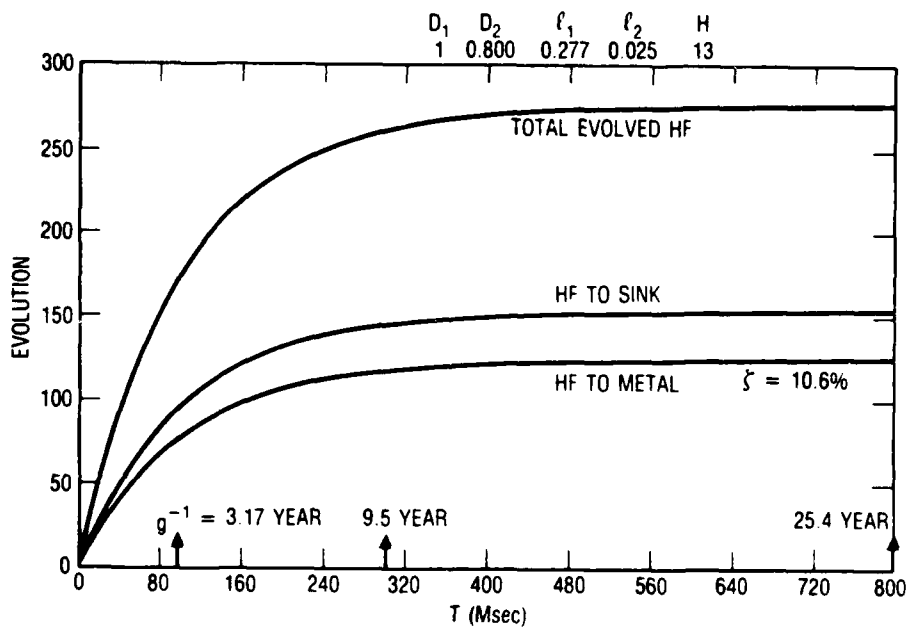


Fig. III-18. Time-Evolution of Total HF, HF to Sink (left), and HF to Metal (right), Corresponding to Fig. III-17. $\zeta = 10.6\%$.

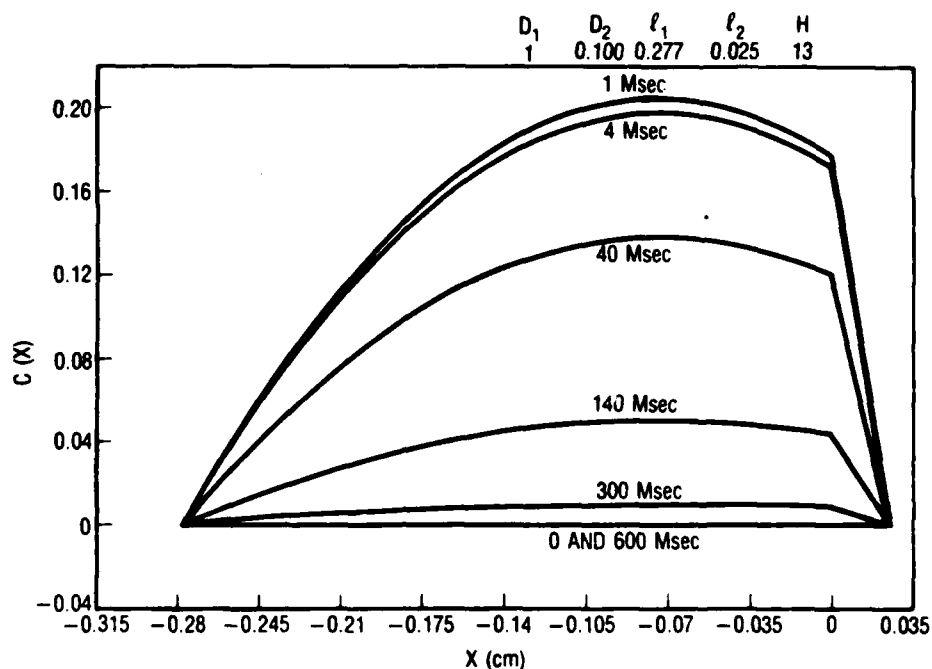


Fig. III-19. HF Concentration vs Position at Several Times, Corresponding to an Al_2O_3 -Filled Model-Polymer Liner as Measured in Section II. Parameters above figure.

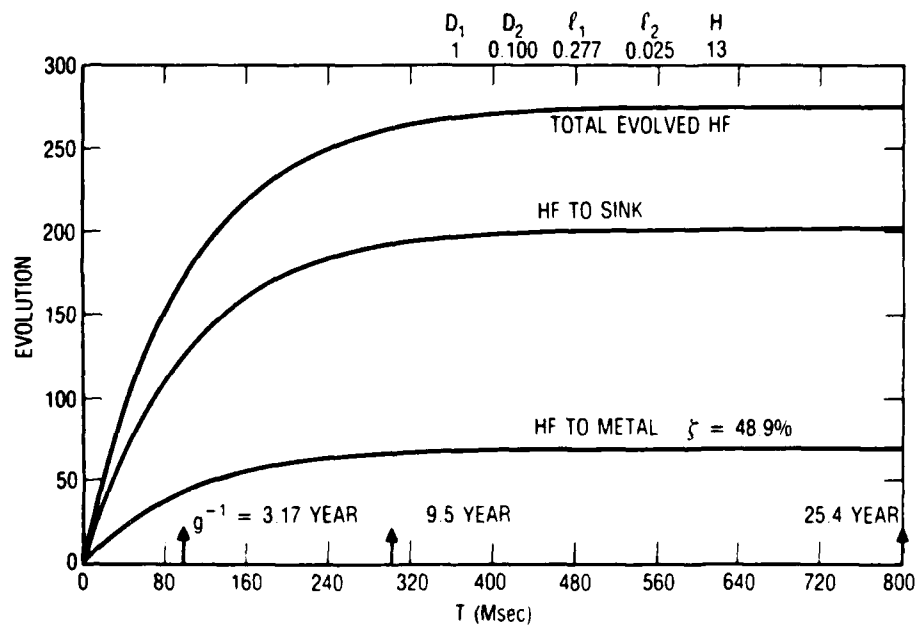


Fig. III-20. Time-Evolution of Total HF, HF to Sink (left), and HF to Metal (right), Corresponding to Fig. III-19. $\zeta = 48.9\%$.

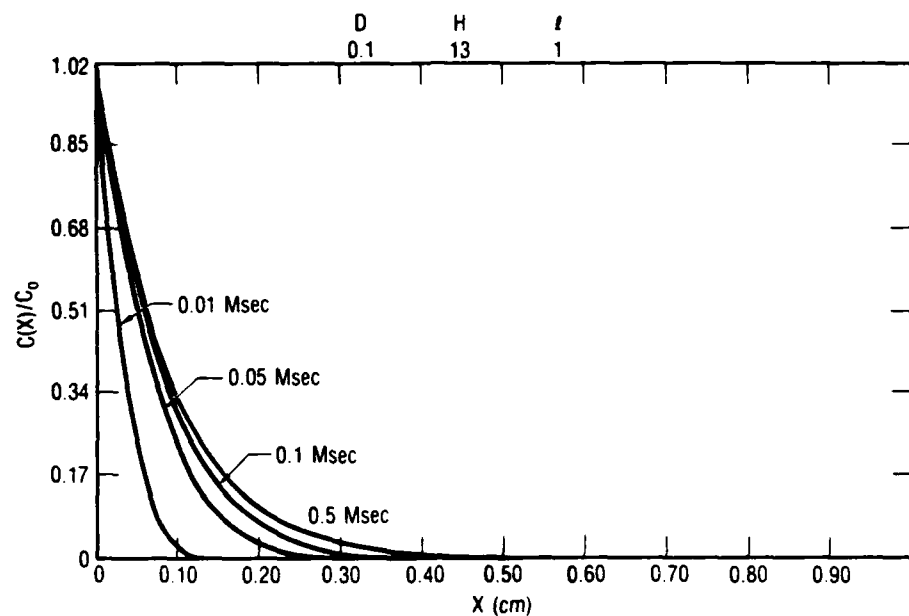


Fig. III-21. Single-Slab Profiles of HF Concentration Which Represent the Al_2O_3 -Filled Uralane Data in Fig. II-13b. For $x > 0.3$ cm, the experimental data show a low-level plateau not evident in this calculation.

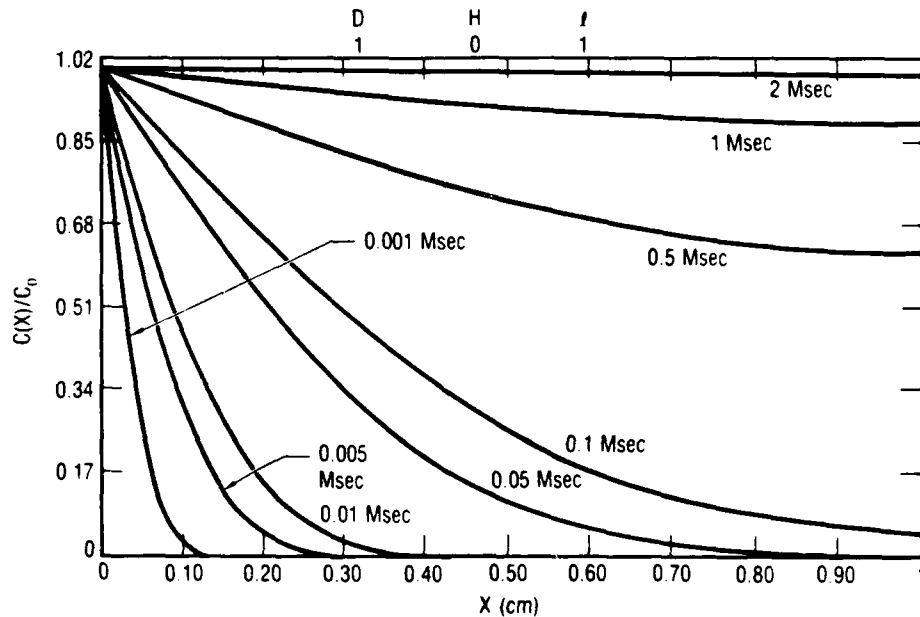


Fig. III-22. Single-Slab Results for the Parameters Given Above Figure. Since $H = 0$, the concentration approaches unity everywhere for long time.

single-slab response (see the equations in Section II) in Fig. III-23. This result adequately represents the experimental data in Fig. II-13b. Actually, the representation is believed to be conservative, because the low-level plateau extends farther in the computed response.

This same 90%/10% ratio of diffusing particles in the ($D_2 = 0.1$, $H = 13$)/($D_2 = 1$, $H = 0$) channels can be used in the double-layer calculations just described. The results are shown in Figs. III-24 and III-25. There is only a small difference from the results shown in Figs. III-19 and III-20. In fact, $\tau = 44.8\%$ in the defective system, compared to 48.9% in the perfect, filled system. This result is also intuitively clear, because the low-level plateau has essentially zero slope and the flux is proportional to the slope. Of course, it is possible to imagine the formation of giant cracks in a filled polymer exposed to HF and the drastic reduction of its barrier effectiveness. However, this view is contradicted by the available experimental evidence. The observed defects (Section II) are not a catastrophic drawback to the use of filled polymers as barrier liners.

E. SUMMARY

The diffusion-barrier properties of several matrix/liner systems were investigated as a function of thickness (matrix $l_1 = 0.277$ or 0.500 cm, and liner $l_2 = 0.025$ or 0.005 cm); diffusion coefficient (matrix $D_1 = 10$ or 1.0 cm²/Msec, and liner $D_2 = 10$, 1 , 0.1 , or 0.01 cm²/Msec); and reactivity ($H = 0$, 10 , 100 , or 1000 Msec⁻¹). The properties were investigated in a system in which HF gas is generated with a characteristic time of 100 Msec (3.17 years). All parametric combinations are defined in Table III-1.

Some examples of the time-dependent concentration profiles and cumulative fluxes are shown in Figs. III-3 to III-14. The results for the barrier effectiveness, τ , of all the parametric combinations are given in Tables III-2 to III-5, where τ is defined in Eqs. (18a)-(18b) (see also Fig. I-3). The barrier effectiveness, τ , is zero when half of the evolved HF particles impinge on the metal substrate and the other half escapes to the inert sink. The barrier effectiveness, τ , is 100% when none of the

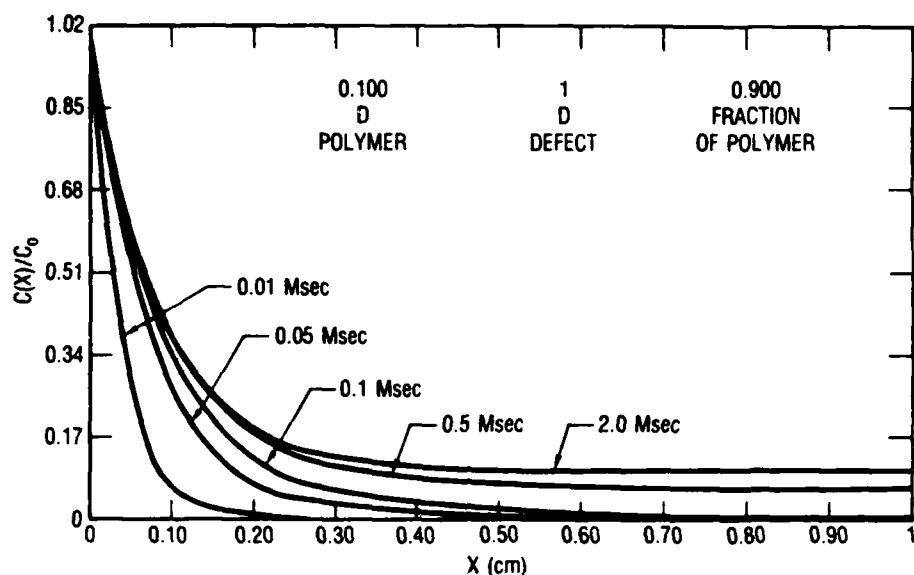


Fig. III-23. Parallel-Pathways Model Result (single slab) for a Filled Polymer ($D = 0.1$, $H = 13$) with Defects ($D = 1$, $H = 0$). The polymer/defect conductance ratio is 90%/10%. This result adequately represents the experimental data in Fig. II-13b. The defects may be provisionally thought of as cracks.

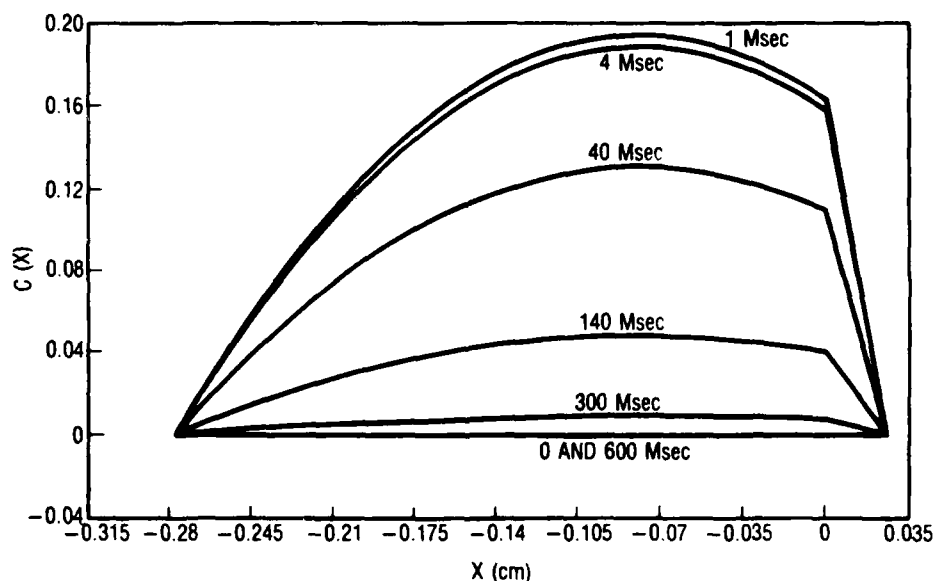


Fig. III-24. Parallel-Pathways Result (double slab) for a Filled Polymer Liner ($D = 0.1$, $H = 13$) with Defects ($D = 1$, $H = 0$) in the Region $x > 0$. The polymer/defect conductance ratio is 90%/10%. The matrix $D_1 = 1$ in the region $x < 0$. This result should be compared to Fig. III-19.

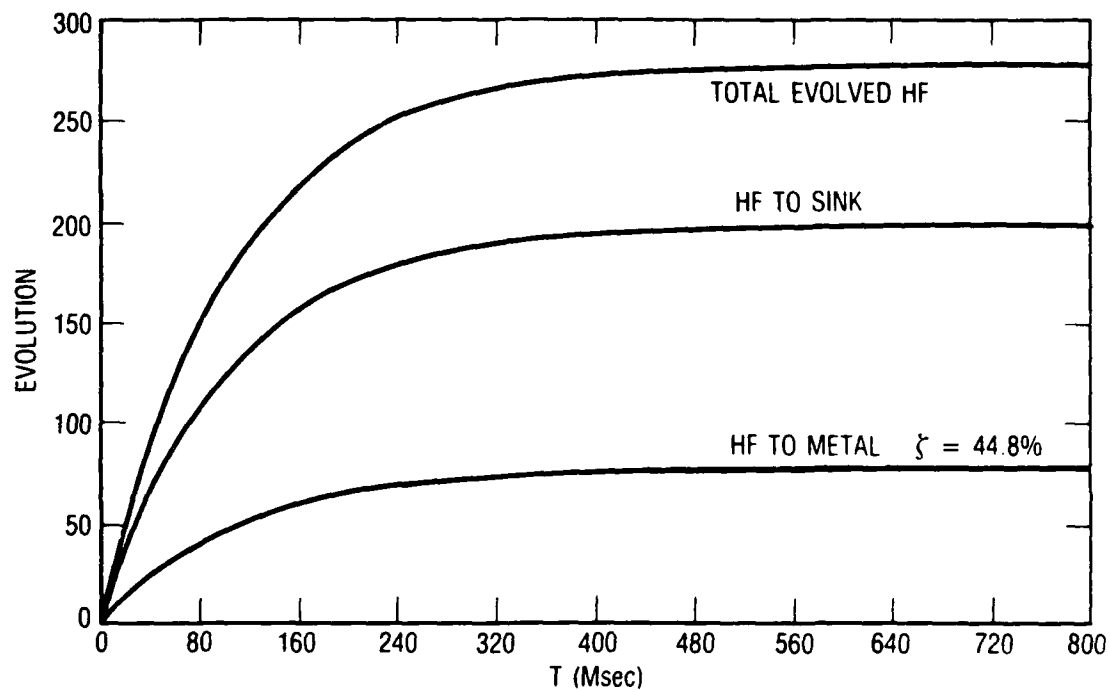


Fig. III-25. Time-Evolution of Total HF, HF at Sink (left), and HF at Metal (right), Corresponding to Fig. III-24 (defective liner). Compared to Fig. III-20 (no defects), we see that the barrier effectiveness is only reduced from 48.9% to 44.8%. These defects may be provisionally thought of as cracks.

evolved HF impinges on the metal substrate, instead either escaping to the inert sink or being immobilized in the liner.

Only a relatively weak dependence of ζ on the reactivity, H , was noted. However, filler particles in real polymer systems also serve to reduce the liner diffusion coefficient, and this reduction can have a dramatic effect on ζ . For the case of the matrix $l_1 = 0.277$ cm and the liner $l_2 = 0.025$ cm, ζ assumes values in excess of 90% for $R = \log(D_1/D_2) = 2$ and values in excess of 47% for $R = 1$. For a given parametric combination, ζ increases monotonically with R (the logarithmic diffusion-coefficient ratio). The most beneficial computed effects were obtained for $R = 2$, which should be the goal of future experimental liner development.

The detection of defects (slightly nonclassical, experimental concentration profiles) in filled polymers exposed to HF raised the possibility that the beneficial effects of the filler could be "short-circuited" by the introduction of faster, parallel diffusion pathways. The precise nature of these defects has not been determined, but they may be provisionally thought of as cracks between the filler particles and the polymer. It was shown, however, that (1) the measured effect of the defects may be successfully modeled by assuming that 10% of the HF travels in the defect pathways and (2) the barrier effectiveness of such a defective liner (based on measurement in Section II) is only reduced from 48.9% to 44.8% by these defects. At this time, there is no observable fatal disadvantage to the use of a filled polymer as a barrier to HF.

IV. EFFECT OF FILLER TYPE ON HF DIFFUSION

A. BACKGROUND

In the previous section, we investigated the effectiveness of unfilled and alumina-filled polymer systems as barrier liners in reducing the amount of HF gas impinging on a metal substrate. In this section, freshly prepared Uralane 5753 was used alone and in combination with magnesium silicate, strontium chromate, and carbon black. The transport coefficients of these liner materials were determined so that multislabs calculations could reveal the extent to which the barrier reduces HF flux at the metal substrate (see Fig. 1-3). One-dimensional diffusion experiments were used, as in Section II, to determine both the basic diffusion coefficient, D , and a second parameter, H , specifying the degree of chemical reactivity between the gas and the liner material.

In Section II, some experiments (of 21 h and 12 day durations) on a model polymer with or without alumina particles (40 wt% of $10 \pm 2 \mu\text{m}$ particles) were found to be consistent with $H \gtrsim 13 \text{ Msec}^{-1}$ for either filled or unfilled polymer: $D \gtrsim 0.8 \text{ cm}^2/\text{Msec}$ for unfilled polymer and $D \gtrsim 0.1 \text{ cm}^2/\text{Msec}$ for filled polymer. (One megasecond is 10^6 sec or 278 h.) In Section III, it was shown that barrier effectiveness of the unfilled system was only 10.6%, while that of the filled system was 44.8%. The barrier effectiveness is the percent reduction in the number of HF particles impinging on the wall due to the presence of the liner.

The enhanced value of the barrier effectiveness results from a liner diffusion coefficient (D_2) which is less than that of the matrix (D_1), as well as from the reactivity (H) of the gas with the liner. In Section II, it is shown that H specifies a rate of decrease of D_2 , which can be interpreted as a progressive diffusion-channel clogging. We suggest that the molecular basis for the existence of a reduced D_2 in our filled polymers is the following (Refs. 12-16): At temperatures below the polymer glass transition temperature, T_g , gas molecules must diffuse by jumping

between fixed free-volume sites, which is a relatively slow process. For $T > T_g$, increased segmental motion and a higher free-volume content allow faster diffusion. Filler particles immobilize polymer segments and raise the effective T_g of the polymer/filler composite. For a given polymer at a given operating temperature, an unfilled system may be above its T_g (high D), while the corresponding filled system may be below its T_g (low D). Not all filled systems may exhibit the drastic effect of raising T_g above the operating temperature, but any increase in T_g will result in some reduction in D. Work is in progress to determine the T_g for the filled and unfilled Uralane under consideration here.

In this section, the relative effects of filling the polymer with magnesium silicate, strontium chromate, and carbon black will be assessed by calculating the barrier effectiveness, ζ , which is defined in Section III as the percent reduction in the number of HF particles impinging on the metal substrate due to the presence of the liner.

B. DIFFUSION-FRONT TRAJECTORIES

Consider a one-dimensional slab of material between positions $x = 0$ and $x = l$. The slab is exposed to a constant gas concentration, c_0 , at $x = 0$. Diffusion of gas into the slab proceeds according to $D \frac{\partial^2 c}{\partial x^2} - Hc = \frac{\partial c}{\partial t}$, where D is the diffusion coefficient and H is the rate of reaction between the gas and the solid (see Section II). The concentration, $c(x,t)$, of gas in the slab is given by

$$\frac{c(x,t)}{c_0} = \frac{\cosh[\omega_0 l (1 - x/l)]}{\cosh \omega_0 l} + \frac{2\sqrt{D}}{l} \sum_{n=1}^{\infty} \frac{\sqrt{-(s_n + H)}}{s_n} \sin\left[\sqrt{\frac{-(s_n + H)}{D}} x\right] \exp(s_n t)$$

$$\omega_0 = \sqrt{H/D}$$

$$s_n = -H - \frac{(2n-1)^2}{\tau} \quad n = 1, 2, 3, \dots \quad (30)$$

$$\tau = \frac{4l^2}{D\pi^2}$$

Figure IV-1 is an example of this solution for the case in which $D = 0.5 \text{ cm}^2/\text{Msec}$, $H = 13 \text{ Msec}^{-1}$, and $l = 1 \text{ cm}$ at the successive times 0.001, 0.004, 0.007, 0.010, 0.025, 0.040, 0.070, 0.100, and 0.500 Msec.

For the case in which $H = 0$ and $l \rightarrow \infty$, this solution may also be written as (see Ref. 19):

$$\frac{c(x,t)}{c_0} = 1 - \operatorname{erf}\left(\frac{x}{2\sqrt{Dt}}\right) \quad (31)$$

where

$$\operatorname{erf}(z) = \frac{2}{\sqrt{\pi}} \int_0^z e^{-\eta^2} d\eta \quad (32)$$

Consider $c(x',t')$, where $c(x',t')/c_0 = 0.1573$. In that case, the argument of $\operatorname{erf}(z)$ is unity, and

$$\begin{aligned} x' &= 2\sqrt{Dt'} & (33) \\ \text{at } c(x,t)/c_0 &= 0.1573 \\ \text{for } H &= 0 \text{ and } l \rightarrow \infty \end{aligned}$$

In Section II, it was hypothesized that this relation could be generalized to

$$x' = \sqrt{\frac{D\pi}{H}} \operatorname{erf}(Ht') \quad (34a)$$

$$x' \approx 2\sqrt{Dt'} \quad Ht' \ll 1 \quad (34b)$$

$$x' \approx \sqrt{\frac{D\pi}{H}} \quad t' \rightarrow \infty \quad (34c)$$

for $l \rightarrow \infty$. In Section II, x' was determined from $c(x',t')/c_0 = 0.17$ for convenience.

The concentration profiles in Fig. IV-1 are all very small, at $x = l$, so, effectively, $l \rightarrow \infty$. These profiles are replotted in Fig. IV-2, and the

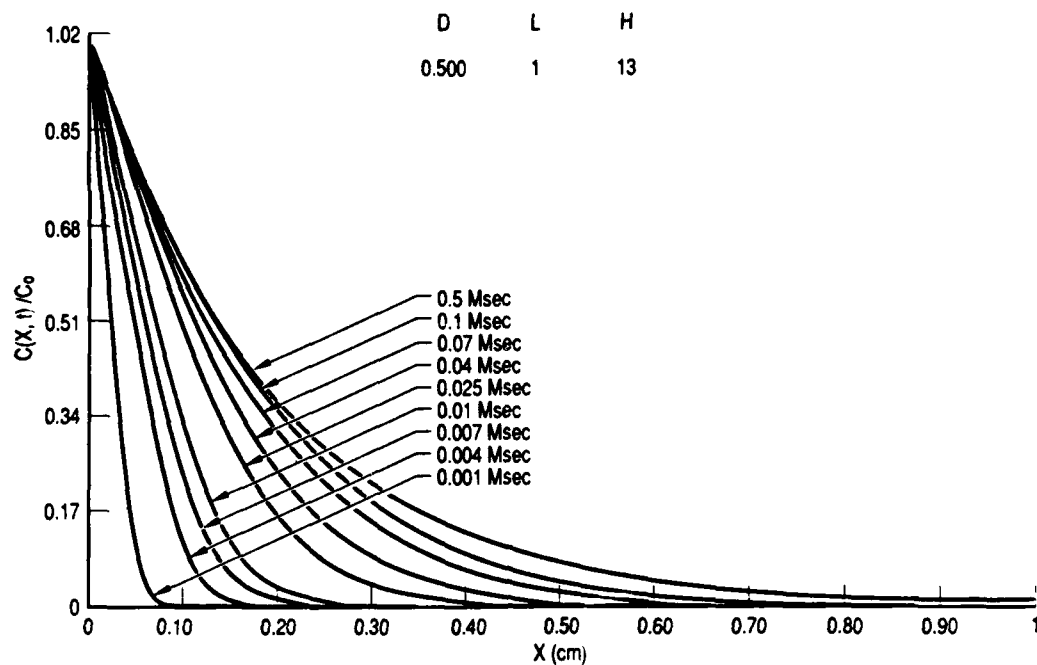


Fig. IV-1. Calculated Concentration Profiles for the Diffusion of Gas into a Solid, Including the Reactivity Between the Gas and Solid. Parameters given above figure.

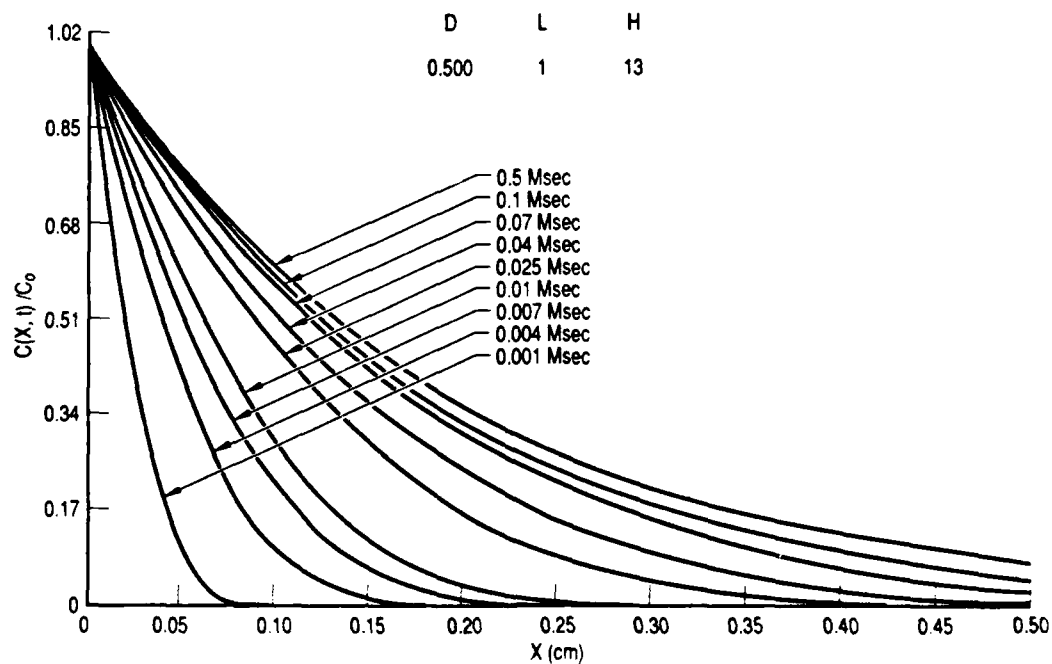


Fig. IV-2. Same Concentration Profiles as in Fig. IV-1 Replotted on a Smaller Scale

successive (x', t') data points at which $c(x', t')/c_0 = 0.1573$ are plotted in Fig. IV-3. There is excellent agreement with Eqs. (34a)-(34c), because the curve shape is like the $\text{erf}(z)$ function, the slope (1.425) at the origin gives $D = 0.51 \text{ cm}^2/\text{Msec}$ [Eq. (34b)], and the plateau (0.36 cm) gives $H = 12 \text{ Msec}^{-1}$ [Eq. (34c)]. This "slope/plateau" approach is the method for determining the fundamental gas-transport quantities D and H from the experimental concentration profiles.

It is beyond the scope of this investigation to measure an entire trajectory like that of Fig. IV-3. To provide an approximate evaluation, the following approach was adopted in Section II. In the cases of unfilled and Al_2O_3 -filled Uralane, it was noted that there was no further advance of the diffusion front at 288 h compared to 21 h of HF exposure. If, on the other hand, H had been zero, the diffusion front would have advanced by a factor of 3.7, according to Eq. (33). If the generalization, Eq. (34a), is valid, then this immobilization of the diffusion front should occur after a characteristic time, H^{-1} . If this time is 21 h or less, then H is 13 Msec^{-1} or more. It is considered conservative to set H at the lower end of this range without jeopardizing the subsequent calculations of barrier effectiveness, which are much less sensitive to H than to D (see Section II). Therefore, in all cases analyzed, we set H to 13 Msec^{-1} as a reasonable estimate until an entire trajectory can be measured.

Using this value of H , the value of D for a gas/polymer system may be obtained from the long-time (stationary) concentration profiles as time tends to infinity, as follows. From Eq. (30), we obtain the slope, σ_0 , where

$$|\sigma_0| = \lim_{t \rightarrow \infty} -\frac{1}{c_0} \frac{\partial c}{\partial x} \bigg|_{x=0} = \sqrt{\frac{H}{D}} \tanh \left(\sqrt{\frac{H}{D}} l \right) \quad (35)$$

Measurement of σ_0 and knowledge of H and l allow D to be calculated.

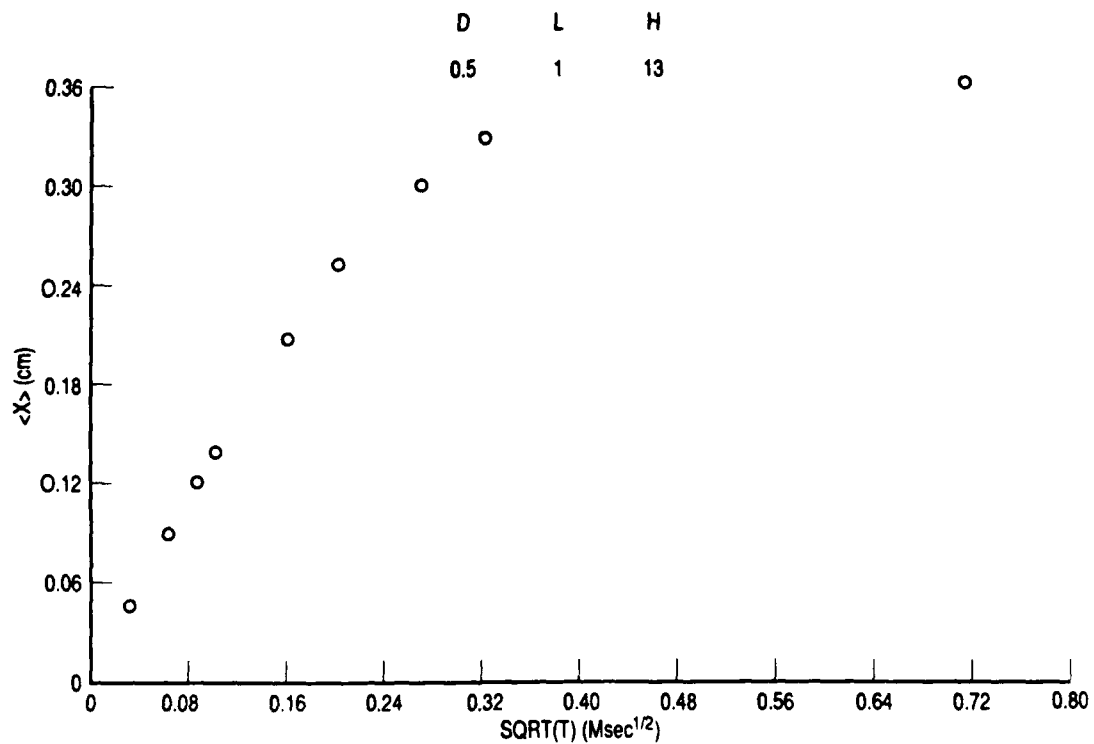


Fig. IV-3. Diffusion Trajectory, $\langle x \rangle$, Plotted vs Square Root of the Diffusion Time for Calculated Profiles in Fig. IV-2. $\langle x \rangle$ is the position of $[c(x)/c_0] = \text{a fixed value}$. This value is 0.1573 for $H = 0$ and is approximately the same for $H > 0$.

C. EXPERIMENTAL METHOD

Polyethylene cups of unfilled and filled Uralane 5753 were freshly prepared for one-dimensional HF diffusion experiments, as described in Section II. The fillers were magnesium silicate ($2\text{MgO} \cdot 3\text{SiO}_2 \cdot x\text{H}_2\text{O}$, Lot No. CE 311, from Spectrum Chemical, with initially 20 wt% MgO and 45 wt% SiO_2); strontium chromate [SrCrO_4 , Lot No. D13C, from Alfa Products/Morton Thiokol (98%)] and carbon black (National Spectroscopic Powder, Lot No. G66, Grade SP2). The fillers were baked at 120°C for 24 h before their incorporation (40 wt%) into the room-temperature cured Uralane. The Uralane and filler mixture was stirred by hand until uniform to the eye. Since the typical XPS beam dimension is about 0.5 mm, while the average interparticle spacing is 30 μm (or less),* the XPS averages over an area containing $17^2 = 289$ or more particles. This being the case, variations in interparticle spacing due to mixing are not expected to be observable in the XPS experiment. The generally monotonic results for fluorine concentration vs depth confirm this expectation. Curing continued for 2 weeks before the HF exposure began. The Uralane, part A, was from batch GLL-017, while part B was from batch HM-056. Both batches were dated January 1988.

The Le Mont particle analyzer was used to determine the filler particle-size distributions for the $\text{MgO} \cdot \text{SiO}_2$ and the SrCrO_4 . There was insufficient contrast to the carbonaceous substrate to allow this scanning electron microscopy (SEM)-based technique to be used for the carbon black. A different technique might allow results for the same grade of carbon black to be determined in the future. The complete analysis for $\text{MgO} \cdot \text{SiO}_2$ and SrCrO_4 is given in Appendix C. Typical particle lengths are $4.6 \mu\text{m} \pm 54\%$ for $\text{MgO} \cdot \text{SiO}_2$ and $5.2 \mu\text{m} \pm 61\%$ for SrCrO_4 .

*If a 40 wt% sample is considered (conservatively) to have 4 vol% of 5 μm particles, then it has $4^{2/3} = 2.5$ area percent of particles. Each 25 μm^2 particle therefore exists on an average area of 1000 μm^2 . The average interparticle distance is therefore $\sqrt{1000}$, or approximately 30 μm (conservatively). If the volume percent is larger, then the interparticle spacing is smaller.

The samples were exposed to HF for 9 days in a large polyethylene chamber. The presence of the polyethylene cups around the samples forced all the HF diffusion to proceed from one face of each sample. After exposure, the samples were sectioned for x-ray photoelectron spectroscopy (XPS) analysis. The fluorine concentration normalized by the carbon concentration was recorded.

D. EXPERIMENTAL RESULTS

Figure IV-4 shows the carbon-normalized fluorine concentration vs penetration depth for the unfilled Uralane after its 9-day exposure to HF. The solid line is a least-squares curve fit [$c(x) = a - \sigma_0 x$] to the data, excluding the points at $x = 1.9$ and 3.8 , which originate from regions considered to be smeared during sample preparation. The theoretical response function over the curve-fit region is not linear; the curve fit is merely a way to objectively estimate the slope at $x = 0$. It is found that $(a, \sigma_0) = (1.720, 0.2456)$ for $c(x)$ in percent and that $(a, \sigma_0) = (1.0, 0.1428 \text{ mm}^{-1})$ for normalized $c(x)/c_0$. Since the sample is about 25 mm deep, we may assume $1 \rightarrow \infty$. Hence, $\sigma_0 = 1.428 \text{ cm}^{-1} = \sqrt{H/D}$, from Eq. (35). Assuming $H = 13 \text{ Msec}^{-1}$, as just noted, $D = 6.4 \text{ cm}^2/\text{Msec}$. This result for freshly prepared Uralane is considerably larger than that obtained for several-year-old Uralane ($D = 0.8 \text{ cm}^2/\text{Msec}$) in Section II. Work is in progress for the determination of T_g for aged samples. As noted in Section IV.A, there is expected to be a correlation between T_g and the diffusion coefficient.

Figure IV-5 shows the concentration profile for the magnesium-silicate-filled Uralane after its 9-day HF exposure. Since the concentration rapidly decreases as x increases, the concentration drops below the XPS detection limit. Thus, the last two data points in Fig. IV-5 show zero concentration.

The solid line in Fig. IV-5 is a least-squares curve fit to the data, excluding the first, seventh, and eighth data points. The first data point is obviously smeared, while the last two data points are not on the approx-

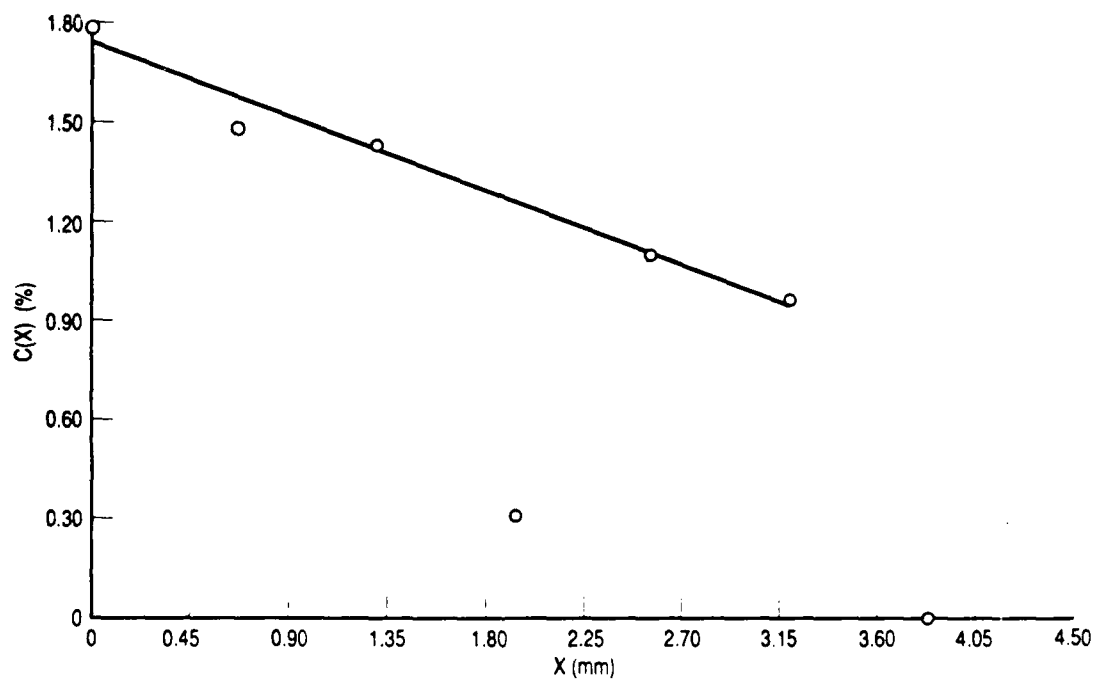


Fig. IV-4. Experimental Fluorine Concentration Profile for Unfilled Uralane After 9 Days of HF Exposure

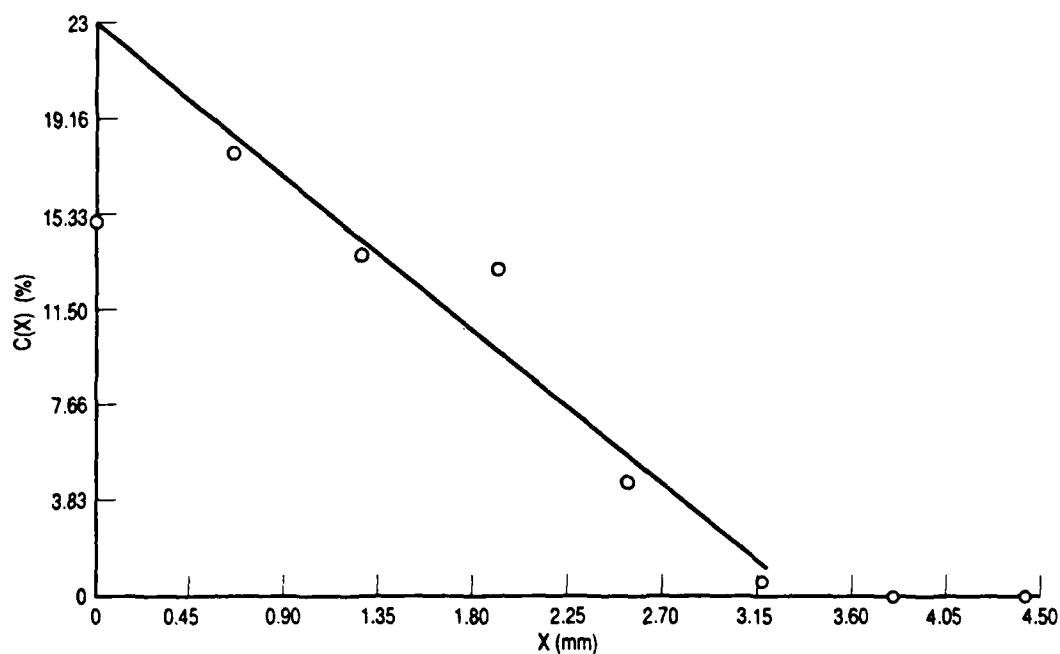


Fig. IV-5. Experimental Fluorine Concentration Profile for MgO·SiO₂-Filled Uralane After 9 Days of HF Exposure

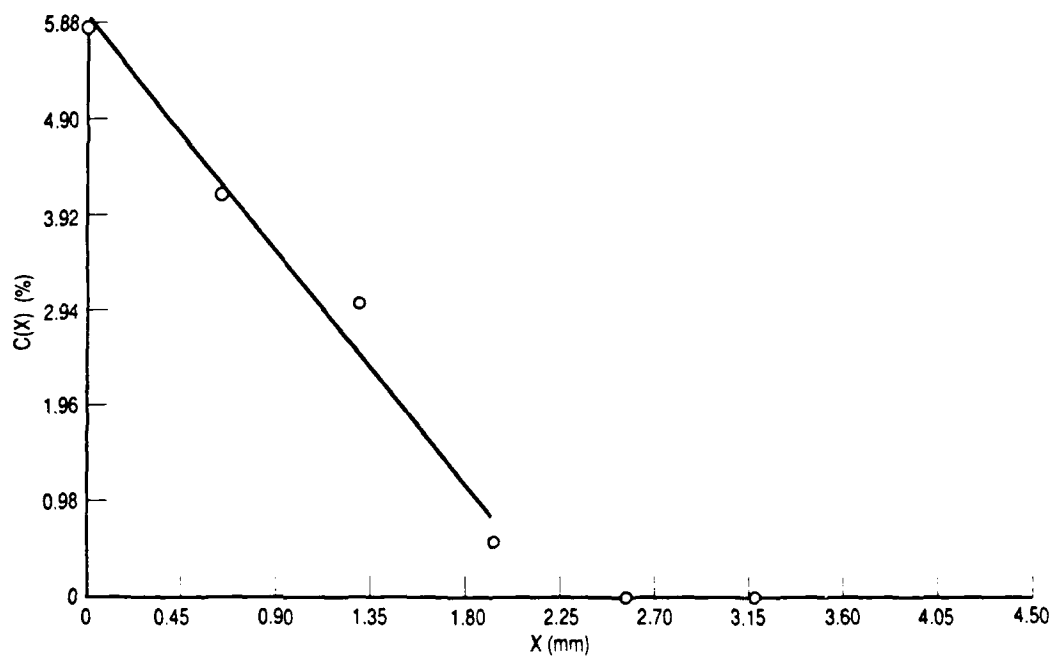


Fig. IV-6. Experimental Fluorine Concentration Profile for SrCrO₄-Filled Uralane After 9 Days of HF Exposure

imately linear portion of the profile. It is found that $(a, \sigma_0) = (23.05, 6.910)$ for c in percent and that $(a, \sigma_0) = (1.0, 0.2998 \text{ mm}^{-1})$ for normalized c . Using $\sigma_0 = \sqrt{H/D}$ and $H = 13 \text{ Msec}^{-1}$, we find $D = 1.4 \text{ cm}^2/\text{Msec}$. Thus, these $4.6 \text{ } \mu\text{m}$ ($\pm 54\%$) magnesium silicate particles reduce D by a factor of 4.5.

Figure IV-6 shows the concentration profile for the strontium-chromate-filled Uralane after its 9 days of HF exposure: The solid line is a least-squares curve fit to the data, excluding the two data points not on the linear portion of the profile. It is found that $(a, \sigma_0) = (5.948, 2.680)$ for c in percent and that $(a, \sigma_0) = (1, 0.4506 \text{ mm}^{-1})$ for normalized c . As before, it is found that $D = 0.64 \text{ cm}^2/\text{Msec}$. Thus, these $5.2 \text{ } \mu\text{m}$ ($\pm 60\%$) strontium chromate particles reduce D by a factor of 10.

Figure IV-7 shows the concentration profile for the carbon-black-filled Uralane after its 9-day HF exposure. Curve fitting reveals that $(a, \sigma_0) = (1.522, 0.7213)$ for c in percent and that $(a, \sigma_0) = (1.0, 0.4739 \text{ mm}^{-1})$ for normalized c . Thus $D = 0.58 \text{ cm}^2/\text{Msec}$, which is an 11-fold decrease from the unfilled condition.

In Table IV-1, the preceding results are summarized. In addition, the barrier effectiveness, ζ , of a polymer liner with these D and H values is calculated. The barrier effectiveness, ζ , is the percent reduction in the number of HF particles impinging on the metal substrate due to the presence of the liner and is rigorously defined in Section II. In these calculations, the matrix thickness is 0.277 cm , and the liner thickness is 0.025 cm .

E. SUMMARY

We investigated the effectiveness of unfilled and filled polymers as barrier liners to reduce the amount of HF gas that evolves from a matrix and impinges upon a metal substrate (see Fig. I-3). The polyurethane, Uralane 5753, was used alone and in combination with magnesium silicate, strontium chromate, and carbon black. Typical particle lengths were $4.6 \text{ } \mu\text{m}$ (for magnesium silicate) and $5.2 \text{ } \mu\text{m}$ (for strontium chromate). The carbon black size distribution was not determined because of lack of contrast (relative to the substrate) in the SEM. After a 9-day exposure to HF gas, the fluorine concentration vs depth was determined by XPS. Assuming that

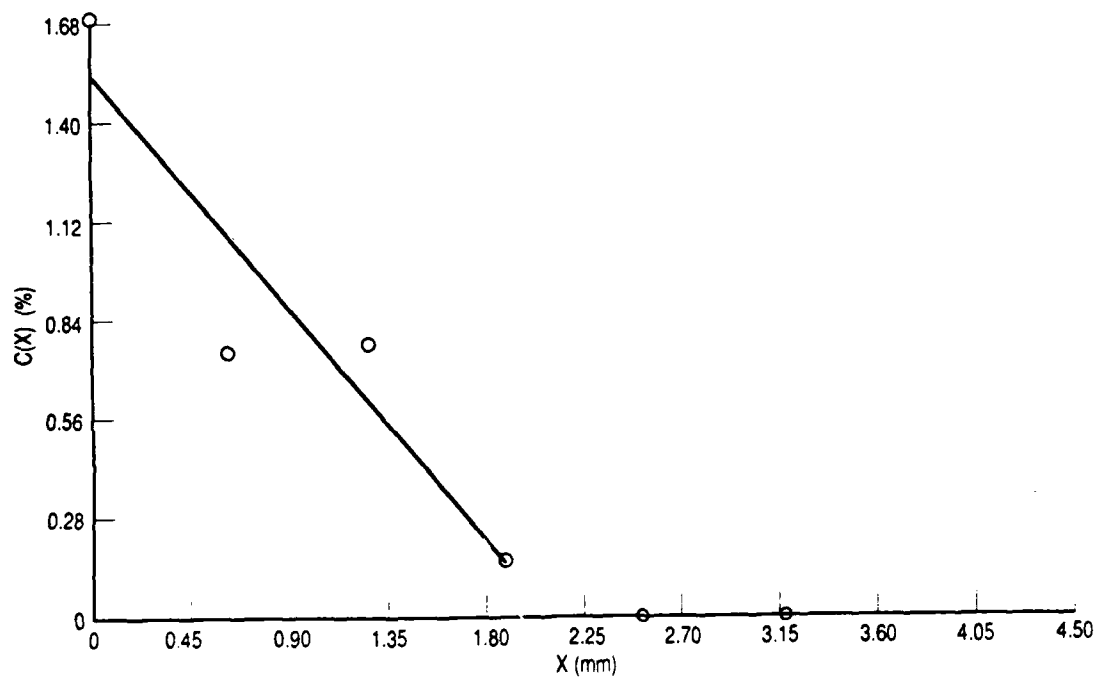


Fig. IV-7. Experimental Fluorine Concentration Profile for Carbon-Black-Filled Uralane After 9 Days of HF Exposure

Table IV-1. Effect of 9-Day HF Exposure on Freshly Cast Uralane 5753(a)
With or Without Filler Particles

Filler	Figure	F concentration		Relative F concentration $c(x)/c_0 = 1 - \sigma_0 x$	D (cm ² /Msec)(b)	τ (s)(c)
		a	b			
None	IV-4	1.720	0.2456	σ_0 (nm ⁻¹) 0.1428	6.4	8.3
	IV-5	23.05	6.910	0.2998	1.4	29.4
MgO.SiO ₂	IV-6	5.948	2.680	0.4506	0.64	47.7
SrCrO ₄	IV-7	1.522	0.7213	0.4739	0.58	50.1
Carbon black						

(a) The values in this table assume $\sigma_0 = \sqrt{H/D}$ and $H = 13 \text{ Msec}^{-1}$ (see text).

The filler amount was 40 wt%, and the typical particle size was 5 μm .

(b) In Section II, several-year-old Uralane 5753 (unfilled) had $D = 0.8 \text{ cm}^2/\text{Msec}$, while several-year-old Uralane 5753 filled with 40 wt% of 10 μm

Al₂O₃ had $D = 0.1 \text{ cm}^2/\text{Msec}$.

(c) τ is the percent reduction in the number of HF particles incident upon the metal substrate due to the presence of the barrier liner. In this calculation, the diffusion coefficient of the adjacent matrix is assumed to be $6.4 \text{ cm}^2/\text{Msec}$, because it is assumed that no liner would be used whose diffusion coefficient were higher than that of the matrix from which the metal substrate is to be protected.

A matrix thickness of 0.277 cm was assumed, along with a liner thickness of 0.025 cm.

the reactivity, H , was always 13 Msec^{-1} , as in Section II, we determined that the diffusion coefficients for unfilled, magnesium-silicate-filled, strontium-chromate-filled, and carbon-black-filled Uralane were 6.4, 1.4, 0.64, and 0.58, respectively.

The barrier effectiveness, τ , of a barrier liner has been previously defined (Section III) and is the percent reduction in the number of HF particles impinging on the motor wall due to the presence of the barrier liner. We assumed that the matrix has $D = 6.4 \text{ cm}^2/\text{Msec}$ and evolves HF at a rate Ge^{-gt} , where $g = 0.01 \text{ Msec}^{-1}$ and $G = 10 \text{ particles}/(\text{cm-Msec})$. We determined that barrier effectivenesses are $\tau = 8.3, 29.4, 47.7$, and 50.1% , for the unfilled, magnesium-silicate-filled, strontium-chromate-filled, and carbon-black-filled Uralane, respectively. In this calculation, a matrix thickness of 0.277 cm was used, and the liner thickness was 0.025 cm.

REFERENCES

1. R. S. Bretzlaff, T. A. Freitag, and A. Lee, Polym. Engr. and Sci. **26**, 931 (1986).
2. R. S. Bretzlaff, A. Y. Lee, and T. A. Freitag, "Adhesion and the Surface Behavior of the Silicone Elastomer RTV-142," TR-0084A(5935-03)-4, The Aerospace Corporation, El Segundo, CA (1985).
3. D. E. Packham, "The Adhesion of Polymers to Metals: The Role of Surface Topography," in Adhesion Aspects of Polymeric Coatings, ed. K. L. Mittal, Plenum, NY (1983).
4. S. K. Brauman and M. E. Hill, J. Organic Chem. **34**, 3381 (1969).
5. Polymer Handbook, Second ed., eds. J. Brandrup and E. H. Immergut, John Wiley and Sons, NY (1975).
6. H. W. Wyld, Mathematical Methods for Physics, W. A. Benjamin, Reading, MA (1976).
7. R. V. Churchill, Duke Math. J. **2**, 405 (1936).
8. R. S. Bretzlaff, J. Appl. Phys. **58**, 2816 (1985).
9. J. G. Holbrook, Laplace-Transformationen, Vieweg, Braunschweig, Germany (1970).
10. F. Dennerly and A. Krzywicki, Mathematics for Physicists, Harper and Row, NY (1967).
11. Handbook of Mathematical Functions, eds. M. Abramowitz and I. A. Stegun, Dover, NY (1972).
12. C. A. Kumins, "Sorption and Electrical Properties of Polymers-Adhesion and Corrosion Effects," eds. G. D. Parfitt and A. V. Patsis, in Sixth International Conference in Organic Coatings Science and Technology, Technomic Publishing Company, Westport, CT (1982).
13. C. A. Kumins and J. Roteman, J. Polym. Sci. **A1**, 527 (1963).
14. C. A. Kumins, J. Roteman, and C. J. Rolle, J. Polym. Sci. **A1**, 541 (1963).
15. T. K. Kwei and C. A. Kumins, J. App. Polym. Sci. **8**, 1483 (1964).
16. K. Isoka and K. Shibayama, J. Appl. Polym. Sci. **22**, 1845 (1978).

17. E. A. DiMarzio and F. Dowell, J. Appl. Phys. 50, 6061 (1979).
18. H. C. Brashears et al., Liner Barrier Technology Program, AFRPL TR-84-022, Air Force Astronautics Laboratory, Edwards Air Force Base, CA (May 1984).
19. P. G. Shewmon, Transformations in Metals, McGraw-Hill, NY (1969), pp. 43-46.

APPENDIX A.

RELATION OF COMPLEX ANALYSIS TO STURM-LIOUVILLE THEORY

This appendix presents the poles of the response function for a double-layer system with the given parameters. Note that in this case, $D_1 = D_2$ and $H = 0$ (see Figs. III-3 and III-4), so that the Sturm-Liouville theory is applicable and the poles must be in the ratio of the squares of the integers. These poles were found numerically and are in the proper ratio to at least seven significant digits in this double-precision calculation.

Case I (Table III-1): $D_1 = 1.0 \text{ cm}^2/\text{Msec}$
 $D_2 = 1.0$
 $H = 0.0 \text{ Msec}^{-1}$

<u>J</u>	<u>SN(J)</u>	<u>Multiplier</u>
1	-0.108214600E + 3	1.0000
2	-0.432858401E + 3	4.0000
3	-0.973931402E + 3	9.0000
4	-0.173143360E + 4	16.0000
5	-0.270536501E + 4	25.0000
.		
.		
.		
31	-0.103994231E + 6	961.0000

series truncated after 31 poles

APPENDIX B

USE OF COMPLEX ANALYSIS FOR CASE OF UNEQUAL D_1 AND D_2

This appendix presents the poles of the response function for a double-layer system with the given parameters (see Figs. III-5 and III-6). Compare to Appendix A.

Case I (Table III-1): $D_1 = 1.0 \text{ cm}^2/\text{Msec}$
 $D_2 = 0.1$
 $H = 1000 \text{ Msec}^{-1}$

<u>J</u>	<u>SN(J)</u>	<u>Multiplier</u>
1	-0.759111699E + 2	1.0000
2	-0.343936153E + 3	4.5308
3	-0.840981695E + 3	11.0785
4	-0.155907427E + 4	20.5381
5	-0.233610574E + 4	30.7742
.		
.		
.		
31	-0.758340216E + 5	998.9837

series truncated after 35 poles

APPENDIX C
PARTICLE-SIZE ANALYSIS

The Le Mont image analyzer was used to obtain the following particle-size information.

SAMPLE ID: SrCrO₄

Number Count: 148

Measurements for Each Physical Parameter

	Area (μm^2)	Ratio of Width to length	Width (μm)	Length (μm)	Angle (deg)	Perimeter (μm)
Avg	4.39	0.163	0.7162	5.2099	82	11.7
RMS Dev	4.66	0.075	0.3448	3.1623	54	6.79
% RMS Dev	106	46	48	61	66	58
Median	2.97	0.149	0.6907	4.2300	79	-
Most Probable	3.40	0.125	0.8150	3.2500	23	-

SAMPLE ID: MgO·SiO₂

Number Count: 105

Measurements for Each Physical Parameter

	Area (μm^2)	Ratio of Width to length	Width (μm)	Length (μm)	Angle (deg)	Perimeter (μm)
Avg	7.25	0.262	1.2728	4.6207	86	11.4
RMS Dev	9.17	0.109	0.9880	2.5176	54	6.32
% RMS Dev	126	42	78	54	62	56
Median	3.98	0.236	0.9794	4.1078	84	-
Most Probable	7.30	0.225	0.8150	5.1500	164	-

LABORATORY OPERATIONS

The Aerospace Corporation functions as an "architect-engineer" for national security projects, specializing in advanced military space systems. Providing research support, the corporation's Laboratory Operations conducts experimental and theoretical investigations that focus on the application of scientific and technical advances to such systems. Vital to the success of these investigations is the technical staff's wide-ranging expertise and its ability to stay current with new developments. This expertise is enhanced by a research program aimed at dealing with the many problems associated with rapidly evolving space systems. Contributing their capabilities to the research effort are these individual laboratories:

Aerophysics Laboratory: Launch vehicle and reentry fluid mechanics, heat transfer and flight dynamics; chemical and electric propulsion, propellant chemistry, chemical dynamics, environmental chemistry, trace detection; spacecraft structural mechanics, contamination, thermal and structural control; high temperature thermomechanics, gas kinetics and radiation; cw and pulsed chemical and excimer laser development including chemical kinetics, spectroscopy, optical resonators, beam control, atmospheric propagation, laser effects and countermeasures.

Chemistry and Physics Laboratory: Atmospheric chemical reactions, atmospheric optics, light scattering, state-specific chemical reactions and radiative signatures of missile plumes, sensor out-of-field-of-view rejection, applied laser spectroscopy, laser chemistry, laser optoelectronics, solar cell physics, battery electrochemistry, space vacuum and radiation effects on materials, lubrication and surface phenomena, thermionic emission, photo-sensitive materials and detectors, atomic frequency standards, and environmental chemistry.

Computer Science Laboratory: Program verification, program translation, performance-sensitive system design, distributed architectures for spaceborne computers, fault-tolerant computer systems, artificial intelligence, micro-electronics applications, communication protocols, and computer security.

Electronics Research Laboratory: Microelectronics, solid-state device physics, compound semiconductors, radiation hardening; electro-optics, quantum electronics, solid-state lasers, optical propagation and communications; microwave semiconductor devices, microwave/millimeter wave measurements, diagnostics and radiometry, microwave/millimeter wave thermionic devices; atomic time and frequency standards; antennas, rf systems, electromagnetic propagation phenomena, space communication systems.

Materials Sciences Laboratory: Development of new materials: metals, alloys, ceramics, polymers and their composites, and new forms of carbon; non-destructive evaluation, component failure analysis and reliability; fracture mechanics and stress corrosion; analysis and evaluation of materials at cryogenic and elevated temperatures as well as in space and enemy-induced environments.

Space Sciences Laboratory: Magnetospheric, auroral and cosmic ray physics, wave-particle interactions, magnetospheric plasma waves; atmospheric and ionospheric physics, density and composition of the upper atmosphere, remote sensing using atmospheric radiation; solar physics, infrared astronomy, infrared signature analysis; effects of solar activity, magnetic storms and nuclear explosions on the earth's atmosphere, ionosphere and magnetosphere; effects of electromagnetic and particulate radiations on space systems; space instrumentation.